

NUMERICAL STUDIES OF VORTEX DYNAMICS IN SUPERCONDUCTIVITY

A Dissertation

Submitted to the Graduate School
of the University of Notre Dame
in Partial Fulfillment of the Requirements
for the Degree of

Doctor of Philosophy

by
Wenzhao Li

Boldizsár Jankó, Director

Graduate Program in Physics

Notre Dame, Indiana

April 2021

© Copyright by

Wenzhao Li

2021

CC-BY-4.0

NUMERICAL STUDIES OF VORTEX DYNAMICS IN SUPERCONDUCTIVITY

Abstract

by

Wenzhao Li

The behavior of vortex matter is critical to the applications of superconductivity and the effective control of Abrikosov vortices can lead to higher dissipation-free current carrying capacity (critical current). In this thesis, we study the superconducting vortex dynamics under different pinning potential systems via numerical simulations. We first show that on a moiré pinning pattern, the critical current shows pronounced dips at commensurate angles due to vortices flowing in ordered quasi-one-dimensional channels. These flow channels break apart at incommensurate angles and for certain angles, the pinning pattern forms five-fold symmetry which can further suppress the easy flow channeling. We also study the vortex dynamics on the so-called "Santa Fe ice" pinning array and show that due to the frustrated geometry, the critical current profile of such a superconductor does not present any commensurability-induced peaks like the ones observed in other periodic patterns. When above the critical current, the vortices in Santa Fe pinning pattern develop both transverse and longitudinal flow channels while easy straight channels form in the square lattice. We also collaborate with an experiment group at Argonne National Lab and provide simulation evidence on the vortex flow in liquid state under different artificial spin ice configurations and show that the resistivity response in liquid state can be controlled by the underlying magnetic potential landscapes. We also present a thorough numerical study on the vortex ratchet motion induced by asymmetric potentials in

such systems. At a more fundamental level, we propose a network science approach to systematically study the potential energy landscapes of confined vortex matter. We find that after mapping the full configuration space onto a complex network, the energetic property of the system is correlated with the topology of its network representation. In the vast majority of cases, the ground state of the system belongs to the sub-network with the highest number connections. Furthermore, with the large scale computing methods, we show that the system stability depends on the container symmetry, container size and vortex number.

CONTENTS

Figures	iv
Chapter 1: Introduction	
1.1 Superconductivity	1
1.2 Type-II Superconductors and Abrikosov Vortex	3
1.3 Vortex Dynamics	5
1.4 Molecular Dynamics Simulation	6
1.5 Motivations	7
1.6 About This Thesis	8
Chapter 2: Vortex Dynamics on Moiré Patterns	
2.1 Overview	9
2.2 Method	11
2.3 Results and Discussion	12
2.3.1 Pinning Pattern	12
2.3.2 Annealing Process	13
2.3.3 Critical Current	13
2.3.4 Vortex Trajectories	18
2.3.5 Transverse Motion	22
2.3.6 Matching Effect	22
2.4 Summary	24
Chapter 3: Vortex Ordering and Dynamics on Santa Fe Artificial Ice Pinning Arrays	
3.1 Overview	26
3.2 Method	29
3.3 Results and Discussion	32
3.3.1 Ground States	32
3.3.2 Critical Current	32
3.3.3 Vortex Flow	34
3.3.4 Different Pinning Densities	36
3.4 Summary	36

Chapter 4: Hybrid Material of Artificial Spin Ice and High Temperature Superconductor	39
4.1 Overview	39
4.2 Method	43
4.3 Results and Discussion	45
4.3.1 Vortex Liquid State	45
4.3.2 Resistivity Response	46
4.3.3 Vortex Ratchet Effect	49
4.4 Summary	55
Chapter 5: Potential Energy Landscape Networks of Confined Vortex Matter	56
5.1 Overview	56
5.2 Method	59
5.2.1 Newton-Raphson Method	60
5.2.2 Eigenvector Following	62
5.3 Results and Discussion	64
5.3.1 Local Minima	64
5.3.2 Network Representation	66
5.3.3 K-Core Decomposition	66
5.3.4 Network Complexity	69
5.3.5 Melting Temperature	70
5.4 Summary	73
Chapter 6: Conclusion and Future Work	75
Appendix A: Large Scale Computing at Notre Dame	77
A.1 Overview	77
A.2 Condor	79
A.3 Work Queue	79
A.4 Example	81
A.4.1 Sample Code	82
Appendix B: Supplement Information	87
Bibliography	89

FIGURES

1.1	The resistance of superconductors drops to zero when cooled below the critical temperature, T_c	2
1.2	(a) Phase diagram for type-I superconductors. (b) Demonstration of the Meissner effect. Magnetic field is expelled by the superconductor. [1]	2
1.3	Phase diagram for type-II superconductors.	4
1.4	Demonstration of vortices driven by external driving current[2]. . . .	5
2.1	An illustration of twisted bilayer graphene (TBG).	10
2.2	The pinning array structures for two triangular lattices where the blue lattice is kept fixed and the orange lattice is rotated by an angle θ of (a) 5.0° , (b) 9.4° , (c) 13.2° and (d) 21.8°	14
2.3	Vortex configurations after annealing for a system with 100 vortices (density $n_v = 0.25$) for $\theta = 5^\circ$ (a), 15° (b), and 25° (c). Blue dots: pinning site centers for a hexagonal lattice. Orange dots: a second hexagonal lattice rotated by θ . Large dots: vortices.	15
2.4	Vortex configurations after annealing for a system with 300 vortices (density $n_v = 0.75$) for $\theta = 5^\circ$ (a), 15° (b), and 25° (c). Blue dots: pinning site centers for a hexagonal lattice. Orange dots: a second hexagonal lattice rotated by θ . Large dots: vortices.	15
2.5	Vortex configurations after annealing for a system with 1000 vortices (density $n_v = 2.5$) for $\theta = 5^\circ$ (a), 15° (b), and 25° (c). Blue dots: pinning site centers for a hexagonal lattice. Orange dots: a second hexagonal lattice rotated by θ . Large dots: vortices.	16
2.6	(a) The critical current F_c vs θ for the system in Fig. 2.2 at varied vortex densities of $n_v = 0.25$ to 2.5 in increments of 0.25 . (b) F_c vs θ at $n_v = 1.25$, showing dips at $\theta = 9.4^\circ$, 13.2° and 21.8° as well as a peak near 28° . The letters a, b, c, and d correspond to the locations of the images in Fig. 2.8.	17
2.7	Critical current F_c vs θ in samples of size (a) $L = 16\lambda$ and (b) $L = 24\lambda$. .	19

2.8	The vortex positions (dots) and trajectories (lines) just above depinning for the system in Fig. 2.6(b) with $n_v = 1.25$. Different colors indicate the motion of different individual vortices. (a) $\theta = 9.4^\circ$ and $F_d = 1.5$, where quasi-one-dimensional flow patterns form. (b) $\theta = 13.2^\circ$ and $F_d = 1.5$, with easy flow channeling. (c) $\theta = 17^\circ$ and $F_d = 2.0$, an incommensurate angle showing more disordered channeling. (d) $\theta = 21.8^\circ$ and $F_d = 1.5$, where there is strong channeling.	20
2.9	(a) The pinning site arrangement for the system in Fig. 2.6(b) at $\theta = 27.9^\circ$ where a peak appears in the critical current near $n_v = 1.25$. Here the substrate has considerable five-fold ordering or quasiperiodic type ordering. (b) The vortex flow pattern over the pinning sites at $F_D = 2.0$, showing a lack of ordered motion. Different colors indicate the motion of different individual vortices.	21
2.10	The transverse velocity $\langle V_y \rangle$ vs θ for the system in Fig. 2.6(b) at $F_d = 1.5, 2.0, 2.5$, and 3.0 , from bottom to top. There are strong transverse velocities at the commensurate angles, which correspond to the dips in the critical current.	23
2.11	Vortex trajectories at $\theta = 6.6^\circ$, $n_v = 1.25$ and $F_d = 3.0$	23
2.12	Critical current F_c vs magnetic field n_v for $\theta = 9.4^\circ, 13.2^\circ$, and 21.8° . There is a drop in F_c when $N_v/N_p > 2.0$	24
3.1	Illustration of the mapping between spin ice and water ice. A spin that points outward/inward indicates an hydrogen atom that is displaced away from/toward the oxygen atom at the center of the tetrahedron.[3]	27
3.2	Experimental measurement of resistance vs magnetic field on MoGe film with square ice lattice of pinning holes. ($a = 102\text{nm}$ and $d = 300\text{nm}$) Inset shows a scanning electron microscopy image of the square lattice. [4]	28
3.3	(a) Schematic of the Santa Fe ice (SFI) geometry. Experimental images of Santa Fe ice by (b) scanning electron microscopy, (c) magnetic force microscopy and (d) photoemission electron microscopy. [5]	30
3.4	(a) Blue dots indicate the pinning sites arranged in a Santa Fe AFI geometry with $d = 0.825$. (b) The vortex positions (black dots) and pinning locations (blue dots) for the system in panel (a) at $B/B_\phi = 1/2$, where the ice rule is mostly obeyed but there are scattered excitations present (red dots). (c) $B/B_\phi = 1.0$. (d) $B/B_\phi = 1.5$	31

3.5	(a) The critical depinning force F_c vs B/B_ϕ for the SF system in Fig. 3.4(a) with $d = 0.825$ and for a square pinning array. The matching field B_ϕ is for the SF array; in these units, the matching field for the square array is at $1.286B_\phi$. The labels a and b indicate the values of B/B_ϕ at which the images in Fig. 3.4 were obtained. (b) The critical depinning force F_c vs B/B_ϕ for SF systems with different densities of $d = 0.4$ and $d = 1.8$.	33
3.6	The vortex trajectories for the system in Fig. 3.5(a) with $d = 0.825$ at $B/B_\phi = 1.286$ ((a),(b)) and $B/B_\phi = 1.67$ ((c),(d)). (a) and (c) show that above depinning force, the SF lattice exhibits winding labyrinthine flow channels. (b) Under the depinning force, vortices are stuck by the square lattice. (d) The square lattice has easy flow one-dimensional channels. The different colors correspond to different times.	35
3.7	(a,b,c) The pinning site locations (blue dots) and vortex positions (black dots) for the system in Fig. 3.5(b) at $d = 1.8$ with weak vortex interactions where the ice rule is lost. (d,e,f) The same for the system in Fig. 3.5(b) with $d = 0.4$, where the pinning sites begin to overlap, creating labyrinth-like vortex states. (a,d) $B/B_\phi = 0.5$. (b,e) $B/B_\phi = 1.0$. (c,f) $B/B_\phi = 2.0$.	37
4.1	Experimental demonstration of the artificial spin ice superconductor heterosystem.	40
4.2	(a)-(c) Demonstrations for type I, II and III ASI magnetic charge orders. (d)-(f) The magnetic field dependence of current-voltage characterization under type I, II and III charge configurations	41
4.3	Demonstration of pinning potential energy landscape with nanoscale bar magnets.[6]	44
4.4	(a) Average standard deviation of vortices as a function of effective temperature. The dashed line $T = 2.4$ indicates when the standard deviation is comparable to the vortex lattice distance. (b)-(g) Vortex movement trajectories at $T = 0.1, 0.5, 1.0, 2.0, 3.0, 4.0$. The melting happens between 2.0 (e) and 3.0 (f). Different colors represent the trajectories of different vortices.	47
4.5	(a) Experiment and (b) simulation results on resistivity responses from three types of ASI configurations on BSCCO.	48
4.6	(a) Schematic of the experimental set-up with a.c. current drive and d.c. voltage detection. (b)-(f) Colour maps of the d.c. voltage response as a function of the a.c. current amplitude and magnetic field under the type I (b), II ((c) and (d)) and III ((e) and (f)) magnetic-charge orders shown in the insets. The magnetic charges in (d) and (f) are reversed (positive to negative and vice versa) compared with those in (c) and (e), respectively.[7]	51

4.7	Simulated color maps of the d.c. voltage response as a function of the a.c. current amplitude and magnetic field under the type II (a) and III (b) configurations.	52
4.8	(a) Simulated color map of the d.c. voltage response as a function of the a.c. current amplitude and period under effective temperature of 1.0. (b)-(d), vortex trajectories corresponding to "b"- "d" labelled in a. For every a.c. period, (b) shows vortices being trapped in each plaquette, (c) shows vortices only jumping out of one side of the plaquette causing ratchet motion and (d) shows vortices jumping out of both sides of the plaquette. Different colors represent the trajectories of different vortices.	53
4.9	Simulated color maps of the d.c. voltage response as a function of the a.c. current amplitude and period under effective temperatures of 1.0 (a), 3.0 (b), 6.0(c) and 10.0(d).The pattern gets more blurry as the effective temperature increases.	54
5.1	Vortices in NbSe ₂ defined by scanning tunneling microscopy (STM). [8]	57
5.2	Experimental measure of melting temperature of vortices confined in mesoscopic square container. [9]	58
5.3	Potential energy landscape of a square superconducting sample with eight vortices.	61
5.4	Experimental results of 7 vortices confined circular(a) and square(c)[10] containers. The corresponding simulation results are shown in (b) and (d).	64
5.5	Top: Images taken with scanning SQUID on mesoscopic triangular containers with increasing vortices[11]. Bottom: Simulation results generated from our simulation.	65
5.6	Network representation and its relation to real space configurations. (a) Network representation of the potential energy landscape (PEL) of 47 vortices in a square container. Each vertex corresponds to a metastable state, and those with larger sizes are of lower energy. An edge between 2 vertices means that there is at least 1 transition state connecting the 2 metastable states represented by the 2 vertices. (b) Energy change along a transition path from state A to state B through transition state TS, overcoming an energy barrier. (c) Real space configurations correspond to the metastable states and transition state along the transition path in (b).	67

5.7	Energy of states in different k-core decomposition shells with 50 superconducting vortices for (a) square container (b) triangular container. The corresponding potential energy landscape network representation is shown in (c) and (d). The size of each container is $25\lambda^2$. The ground state is always in the shell with the largest k-core decomposition shell index as highlighted with red circles.	68
5.8	(a) Normalized network complexity for the potential energy landscape in square and triangular containers with varying vortex numbers. (b)-(f) Vortex configurations in square and triangular containers corresponding to the network complexity dips in (a).	71
5.9	(a) Melting temperatures in triangular containers corresponding to varying vortex numbers and sample sizes. (c) – (g) Vortex configurations corresponding to the data points (c) – (g) in (b). These states have higher stability due to the perfect symmetry between vortex numbers and container geometry. In triangular containers, when the numbers of vortex are the triangular numbers: 6, 10, 15, 21, 28, etc., the containers can be perfectly filled, which leads to higher stability. Panels (h) and (i) show the transition from (d) and (e) as labelled by arrows in (b). As the containers get smaller, the vortices are squeezed by the container walls such that the perfect symmetry is destroyed. This is the size effect that we mention in our main text and can result in the decrease of stability. (j) – (l) Vortex configurations corresponding to the data points (j) - (l) in (b). These states preserve the three-fold symmetry of the system. They also show higher stability than the states with two-fold symmetry ((h), (i), (m)) and the states with no mirror symmetry ((n)). (m) – (n) Random unstable states. . .	72
A.1	Top Condor users in the year of 2020 at University of Notre Dame. .	78
A.2	The general framework of a Work Queue application.	80
B.1	Simulated distributions of flux quanta under type I, II and III magnetic-charge orders and various flux-quantum densities. Solid black lines constitute Voronoi diagrams elucidating the flux-quantum ordering. One repeating unit structure in each of the crystallized flux-quantum lattices is highlighted in yellow.[7]	88

CHAPTER 1

INTRODUCTION

1.1 Superconductivity

For an ordinary metallic conductor at room temperature, the electrical resistance decreases gradually with decreasing temperature and eventually saturates at a finite value. However, as first discovered in 1911 by Dutch physicist Heike Kamerlingh Onnes, the electrical resistance of certain metals vanishes completely when cooled below the boiling temperature of liquid helium, as shown in Fig. 1.1[12]. The phenomenon where a charge can move through a material without resistance is called superconductivity. Because of the discovery of superconductivity, Heike Kamerlingh Onnes was awarded the Nobel Prize in 1913.

Besides the absolute zero resistance, another characteristic of superconductivity is the Meissner-Ochsenfeld effect[13]. In 1933, German researchers Walther Meissner and Robert Ochsenfeld discovered that if a superconductor is placed into a weak magnetic field when transitioning into the superconducting state, the magnetic field is ejected by the bulk of the superconductor. The expulsion is not complete around the edge of the superconductors but instead the magnetic field can penetrate into the superconductor by a very small distance. This penetration is characterized by a parameter λ , which is called the penetration depth[1]. The field decays exponentially to zero in the bulk of the superconductor. A simple sketch illustrating the Meissner effect is shown in Fig. 1.2(b).

The Meissner effect also demonstrates the existence of the critical field. When the applied magnetic field is too strong, the superconducting state can be destroyed and

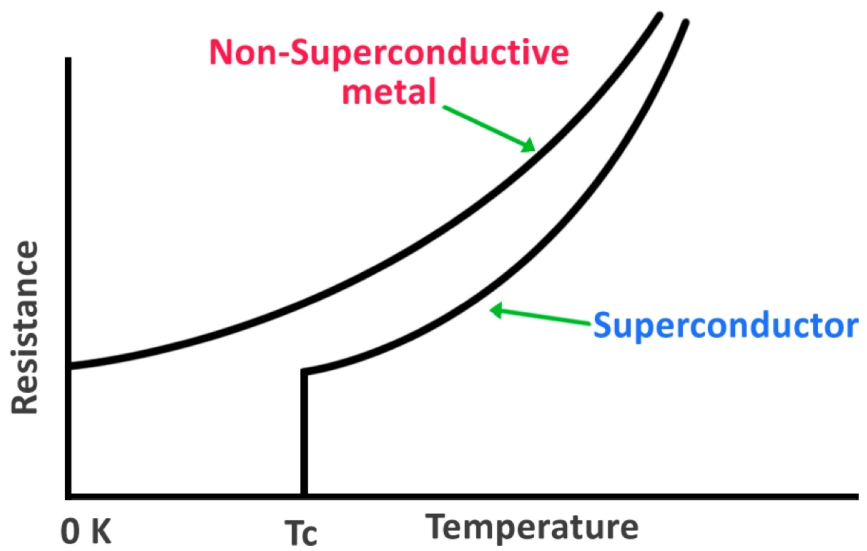


Figure 1.1. The resistance of superconductors drops to zero when cooled below the critical temperature, T_c .

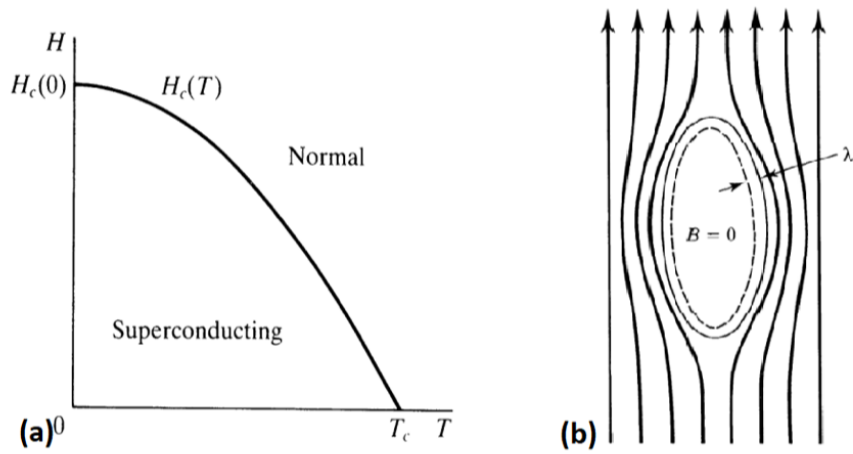


Figure 1.2. (a) Phase diagram for type-I superconductors. (b) Demonstration of the Meissner effect. Magnetic field is expelled by the superconductor. [1]

return to the normal state. For type-I superconductors, the critical field is usually referred as H_c . In Fig. 1.2(a), a phase diagram for type-I superconductors is shown.

1.2 Type-II Superconductors and Abrikosov Vortex

Since the discovery of superconductivity, a lot of physicists have worked in the field of low temperature physics both on experiments and theories. Type-II superconductors were first discovered by Rjabinin and Shubnikov experimentally in 1935[14]. They found that unlike type-I superconductors, where the bulk can repel the magnetic field completely, type-II superconductors allow partial magnetic field to penetrate through. In Fig. 1.3, we show a phase diagram for type-II superconductors. For type-II superconductors, there are two critical fields, H_{c1} corresponding to the field when the superconductor is partially penetrated and H_{c2} when the superconducting state is destroyed. This phenomenon is later explained by the theory developed by two Soviet physicists Lev Landau and Vitaly Ginzburg[15]. Alexei Alexeyevich Abrikosov also further developed the Ginzburg–Landau theory to incorporate type-II superconductors[16]. Due to the prediction of the existence of superconducting vortices, superconducting vortices are named after Abrikosov and he was awarded the Nobel Prize in 2003.

The Ginzburg–Landau theory is a phenomenological theory where the free energy of the superconductors can be expanded in terms of the order parameter. The order parameter is related to the density of superconducting electrons and is non-zero in the superconducting state. The Ginzburg–Landau theory also defines two characteristic parameters: the coherence length ξ and the penetration depth λ . The coherent length characterizes the decay of the order parameter and the penetration depth characterizes the distance to which a magnetic field can penetrate. Most superconductors discovered around that time were type-I superconductors and $\kappa = \lambda/\xi \ll 1$. However, Abrikosov showed that in the opposite limit, when $\kappa = \lambda/\xi > \sqrt{2}$, magnetic

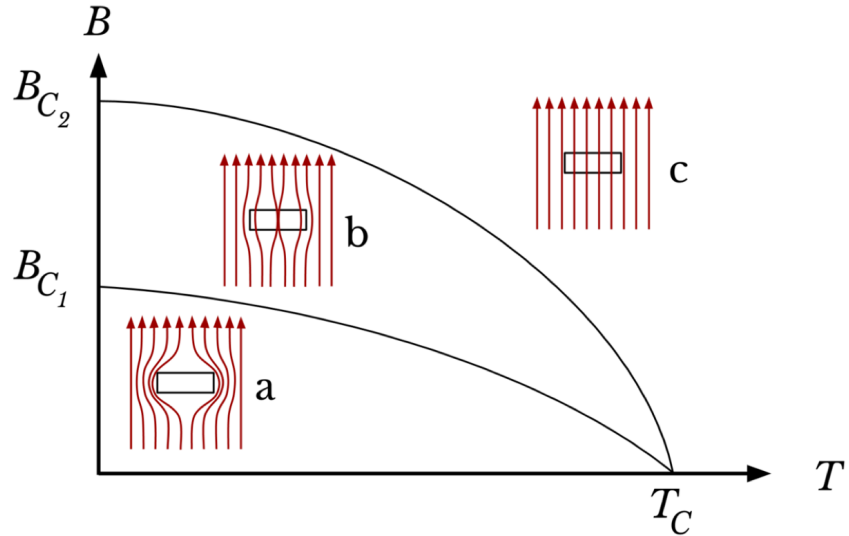


Figure 1.3. Phase diagram for type-II superconductors.

field can penetrate through the superconductors partially between H_{c1} and H_{c2} and the field penetrates as lines of quantized magnetic flux. The quantized magnetic flux is called superconducting vortex or Abrikosov vortex and the vortices are separated from each other by circulating super currents.

In 1957, a microscopic theory of superconductivity was proposed by Bardeen, Cooper and Schrieffer[17]. The BCS theory argued that around the Fermi surface, weak attractive interaction between electrons can form the so-called Cooper pairs and cause the superconducting phase transition. Two years later, Lev Gor'kov showed that the phenomenological Ginzburg–Landau theory can be derived from the BCS theory close to the critical temperature. The BCS theory has been accepted by the majority as the microscopic theory for the low temperature superconductors since then. For this work, the authors were awarded the Nobel Prize in 1972.

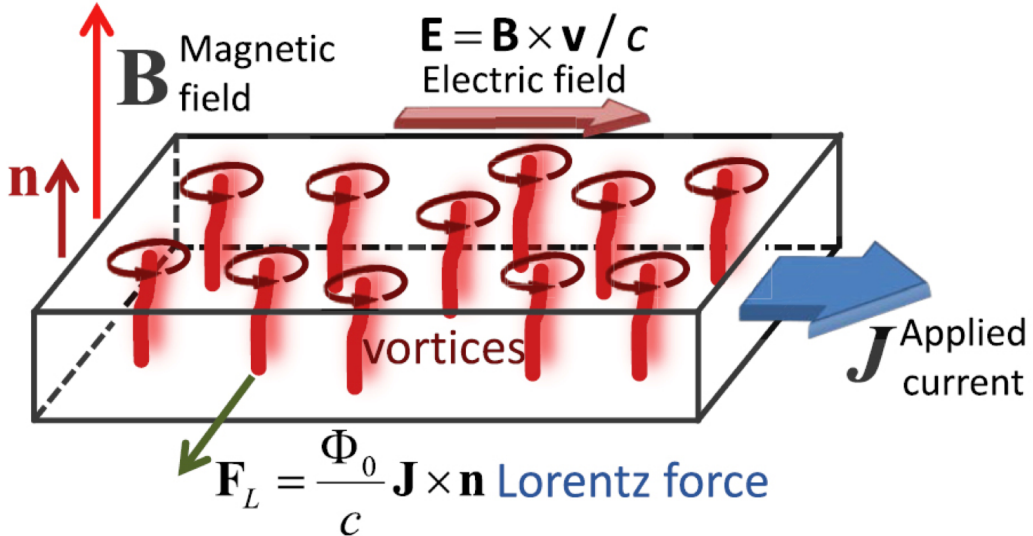


Figure 1.4. Demonstration of vortices driven by external driving current[2].

1.3 Vortex Dynamics

Vortices can be treated as point particles in the London limit($\kappa = \lambda/\xi \gg 1$) and vortex dynamics becomes a many-particle problem. There are several different interactions that determine the vortex dynamics: the vortex-vortex interaction, thermal fluctuations, external current drive and the interaction of vortices with material defects or pinning.

The vortices repel each other in superconductors and the vortex-vortex interaction has the form of modified Bessel function[1]. Without other interactions present, the vortices arrange themselves as triangular vortex lattice and with thermal fluctuations the vortex lattice can transition into the liquid phase like ordinary material matter.

External current can drive the vortices to move. In Fig. 1.4, we show a demonstration of vortices being driven by external current. An external current density \vec{J} can generate a Lorentz force on the vortices perpendicular to the current direction and the vortex line. The Lorentz force has the form $\vec{F}_L = (\Phi_0/c)\vec{J} \times \vec{n}$, where Φ_0 is the flux quantum $\Phi_0 = hc/2e$. Due to the vortex motion perpendicular to the external

current, an electric field is generated, $\vec{E} = \vec{B} \times \vec{v}/c$. The electric field is perpendicular to the vortex velocity and parallel to the external current. The electric field causes a flux-flow resistivity and energy dissipation. Therefore the superconductor loses its ability to carry dissipation-free currents with vortex motion present.

An effective way to increase the superconducting critical currents and suppress the vortex mobility is by introducing pinning sites to the system. They can be the intrinsic defects of the materials, artificial defects like radiation defects and holes or nanoscale bar magnets. The defect can be randomly distributed or patterned as ordered arrays with different geometries, such as triangular, square and conformal patterns[18–26]. By introducing different pinning, one can greatly enhance the current carrying performance of superconductors.

1.4 Molecular Dynamics Simulation

Computer simulations have been widely used in studying vortex dynamics. By solving the time dependent Ginzburg-Landau theory, one can obtain a realistic description of the superconducting order parameter and therefore the vortex dynamics[27, 28]. This approach is a compromise between phenomenological and microscopic description of vortex matter. Another commonly used simulation method and the focus of this thesis, is the molecular dynamics(MD) simulation[29–32]. Molecular dynamics is a computer simulation method for analyzing the physical movements of objects based on their equations of motion. It has been widely used in the field of biology and chemistry to describe the dynamics of molecules and atoms.

At low fields and when the distance between vortices is much larger than the size of the vortex core(coherence length ξ), one can only keep the vortex degrees of freedom and neglect all other perturbations of the superconducting order parameter[31]. If the distance between vortices is much larger than the thickness of the sample, eg. superconducting thin films, then vortices can be treated as pointlike particles and

the system can be seen as interacting objects moving in a 2D environment[31]. The dynamics of such systems can be described by an overdamped equation of motion with thermal Langevin kicks. (The detailed equations are included in the Method sections in the following chapters.)

Usually the simulation starts with random initial configurations, in this case the 2D coordinates of the vortices. With the overdamped equation of motion, we can calculate the vortex-vortex interacting force, pinning force, Lorentz force and the thermal fluctuations for all the vortices in the system. The total simulation time is divided into many small steps. For a given time step, with molecular dynamics we are able to numerically solve the equations of motion and simulate the vortex trajectories and therefore the system evolution. By applying the statistical techniques on the simulation, macroscopic properties of the system can be extracted. In our case, the macroscopic properties can be the critical currents of the superconductors, resistivity responses and voltage signals induced by vortex motion, etc. The details on our molecular dynamics simulation models for each project are presented in the "Method" sections of the following chapters.

1.5 Motivations

Since vortex movement can lead to energy dissipation, one of the keys to improve the performance of superconductors is by limiting the mobility of vortices so that we can increase the dissipation-free current carrying capacity. However, we cannot introduce as many pinning sites as we want because too many pinning sites would suppress the superconductivity and increase the fabrication cost. Therefore we need to design better pinning patterns to limit the vortex mobility and numerical studies of vortex dynamics are essential to exploring possibilities of better pinning strategies and potential superconductor applications.

On the other hand, vortex matter is a good example of a condensed matter system

with competing interactions. The competition between different interactions (vortex-vortex interaction, vortex-pin interaction, Lorentz driving force and thermal fluctuations) leads to various collective behaviors in system stability and order-disorder transition[33–35]. The research methods and results described in this thesis can also be generalized to other many-particle systems such as skyrmions and colloidal particles[36–40].

1.6 About This Thesis

This thesis is organized as follows. In Chapter 2 we present the study on vortex dynamics in a moiré pinning pattern. We find a series of magic angles at which the critical current shows a pronounced dip corresponding to lattices in which the vortices can flow along quasi-one-dimensional channels. In Chapter 3 we show that with the same simulation method but with a different pinning pattern, the Santa Fe artificial spin ice pinning pattern, we find no sharp peaks in the critical current profile due to the geometric frustration and we find transverse flow channels compared to only longitudinal flow channels in square lattice. In Chapter 4, we present the simulation results for the collaborative project with the Superconductivity and Magnetism Group at the Materials Science Division of Argonne National Lab on hybrid material of artificial spin ice and high temperature type-II superconductors, in which we show the possibility of controlling vortex flow in vortex liquid state. In Chapter 5, we focus on a novel approach based on network science to tackle the longstanding magic number problems in the field of mesoscopic confined vortex matter. Finally in Chapter 6, we describe the large scale computing techniques that we used for our simulations and explain how to efficiently perform large scale computing at Notre Dame.

CHAPTER 2

VORTEX DYNAMICS ON MOIRÉ PATTERNS

2.1 Overview

In mathematics and physics, a moiré pattern is a large-scale interference pattern that can be produced when two layers of identical patterns are placed on top of each other, with one of the layers shifted or rotated with respect to the other[41, 42]. Such patterns can produce intriguing phenomena in certain mathematical or physical systems. Recently, a research group at MIT discovered[43–45] that when two layers of graphene are stacked on top of each other but twisted relatively by a small angle, unconventional superconductivity occurs. In Fig. 2.1 we show an example of twisted bilayer graphene (TBG) at a small angle. The moiré pattern on TBG can form larger superlattices on top of the original hexagonal graphene lattice, giving rise to new electronic properties, ranging from non-conductive to superconductive[43, 44]. The study of how the twisted angle can change the material’s electronic properties is called twistronics.

Vortex matter in type-II superconductors is one of the most ideal systems for studying pinning and sliding dynamics on various patterned substrates. Different geometries, such as triangular[23, 33, 46], square[18, 19, 22, 23, 33, 47, 48], rectangular[21, 49, 50], conformal crystal[24, 25], frustrated[4, 51, 52], and other structures[53] of pinning patterns have been realized experimentally. Inspired by TBG, we investigate the pinning and dynamics of superconducting vortices interacting with the moiré pinning pattern. In a superconducting vortex system the pinning

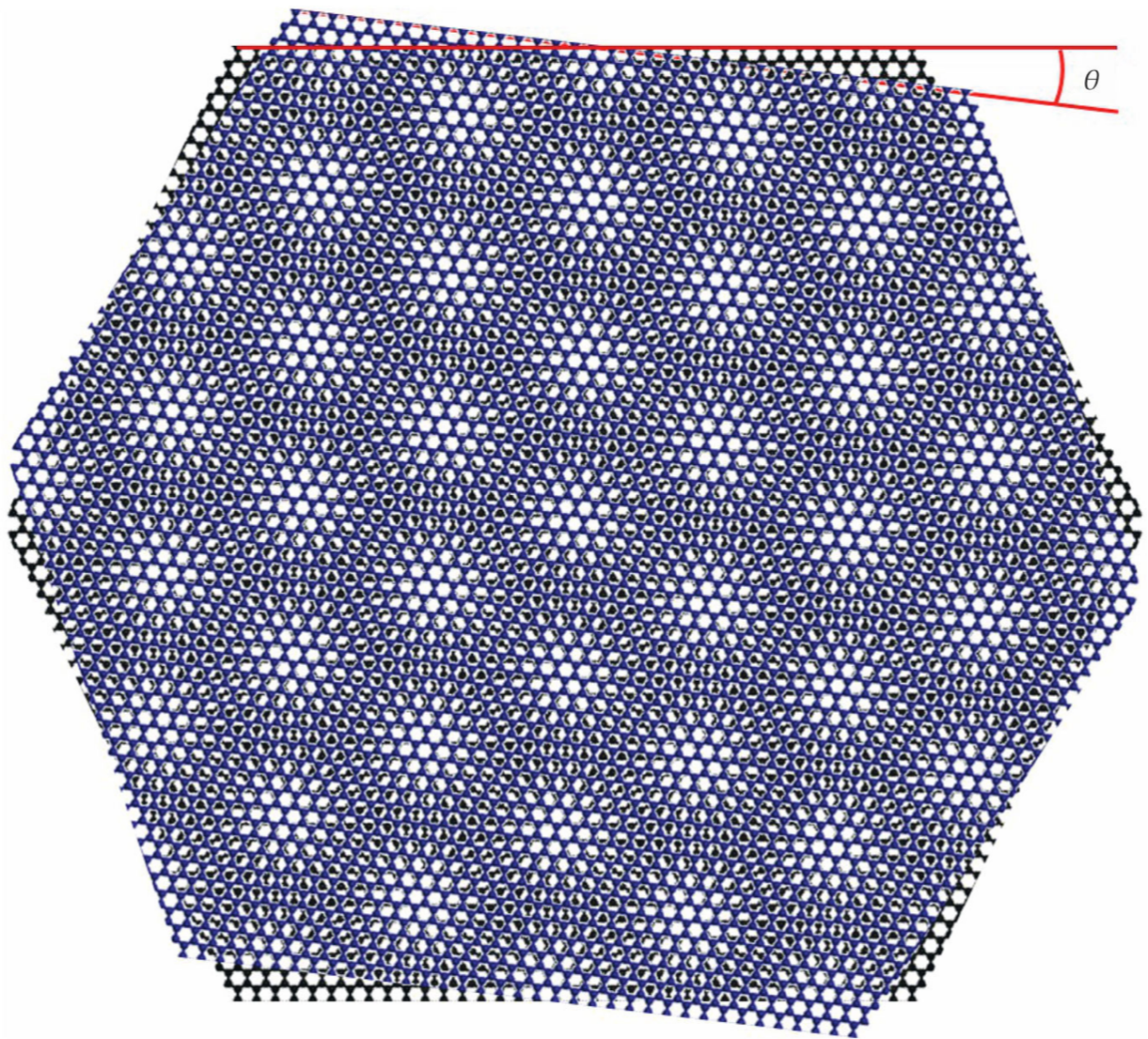


Figure 2.1. An illustration of twisted bilayer graphene (TBG).

properties are typically examined as a function of the magnetic field by varying the number of vortices. In this work, besides varying the number of vortices, we also vary the twisted angle θ between two sheets of triangular pinning patterns. We examine the vortex pinning and motion as a function of θ and observe a wide variety of vortex dynamics. At commensurate angles, where an ordered interference pattern appears, the critical current exhibits a series of dips and the vortices flow in ordered quasi-one-dimensional channels. At these angles, since the vortices can easily flow along the edge of the superlattice, the system develops a finite Hall angle. On the contrary, at incommensurate angles, these flow channels break apart. We also find that for certain angles, the pinning pattern forms five-fold symmetry[54, 55] and suppresses the easy flow channeling. This, in turn, corresponds to the peaks in the critical current profile.

2.2 Method

We consider a system of N_v vortices interacting with a moiré pattern of pinning sites. The equation of motion for vortex i can be described by the following equation:

$$\eta \frac{d\mathbf{R}}{dt} = \mathbf{F}_i^{vv} + \mathbf{F}_i^p + \mathbf{F}_i^d + \mathbf{F}_i^T . \quad (2.1)$$

Here η is the material specific damping coefficient which effectively sets the time scale of the damped motion. In the simulations we set $\eta = 1$ and $dt = 0.008$ is the time step. The repulsive vortex-vortex interaction force is given by $\mathbf{F}_i^{vv} = \sum F_0 K_1(R_{ij}/\lambda) \hat{\mathbf{R}}_{ij}$, where K_1 is the modified Bessel function, R_{ij} is the distance between vortex i and vortex j , $F_0 = \phi_0^2/2\pi\mu_0\lambda^3 = 8.0/\lambda^3$, ϕ_0 is the flux quantum and μ_0 is the permeability, and λ is the penetration depth which we set equal to $\lambda = 1.8$. The size of the system is $L \times L$ with $L = 20\lambda$ and with periodic boundary conditions in the x and y directions. The vortex density is $n_v = N_v/L^2$. The pinning force is

given by $F_i^p = -\sum_{k=1}^{N_p} F_p R_{ik} \exp(-R_{ik}^2/r_p^2) \hat{\mathbf{R}}_{ij}$ where we fix to $r_p = 0.6$. The pinning sites are arranged in two identical triangular lattices with a lattice constant of λ , and the lattices are rotated with respect to each other by an angle θ . The angle θ ranges from $\theta = 0$ to $\theta = 30^\circ$ in increments of $\delta\theta = 0.1^\circ$.

F_i^T is the thermal force arises from Langevin kicks with the following properties: $\langle F_i^T(t) \rangle = 0$ and $\langle F_i^T(t) F_j^T(t') \rangle = 2\eta k_B T \delta_{ij} \delta(t - t')$, where k_b is the Boltzmann constant, T is the temperature and t is time. The initial vortex configurations are obtained by starting from a high temperature liquid state and cooling down to 0K in 80 intervals, where we wait 10^4 time steps during each interval. After annealing we apply a drive in the form of a Lorentz force $F^D = (J \times \hat{\mathbf{z}})\phi_0 d$ which produces vortex motion along the x direction. Here J is the current density, $\hat{\mathbf{z}}$ is the direction of flux-quantum vorticity and d is the thickness of the superconducting sample.

The critical current of the system is obtained by measuring the total vortex velocity $V_x = N_t^{-1} \sum_t \sum_i \hat{\mathbf{x}} \cdot \mathbf{v}_i$, where N_t is the total number of time steps and \mathbf{v}_i is the vortex velocity. When V_x exceeds a threshold and a non-trivial steady state vortex motion occurs, the system is defined as being depinned. The simulations are performed with a parallelized code using the Condor pool at Notre Dame, where we can run at most 6,000 jobs simultaneously. We consider 3000 configurations for each of 300 different values of θ and 10 different vortex densities.

2.3 Results and Discussion

2.3.1 Pinning Pattern

In Fig. 2.2 we show some representative moiré pinning structures in our simulation model for varied angles $\theta = 5.0^\circ, 9.4^\circ, 13.2^\circ$, and 21.8° between the two lattices, colored blue and orange. The blue lattice is fixed and the original lattice is rotated with respect to the center of the substrate. The pinning sites form a superlattice

and we can see that as we increase the twisted angle θ , the superlattice constant decreases.

2.3.2 Annealing Process

The simulation starts with the annealing process. As mentioned previously, we begin the simulation at a high temperature, at which the system is in a molten state. We gradually decrease the temperature to 0K with small intermediate intervals. We obtain the ground states of the system as the initial vortex configurations. Fig. 2.3, 2.4 and 2.5 show the vortex configurations at $n_v = 0.25, 0.75, 2.5$ and $\theta = 5^\circ, 15^\circ, 25^\circ$ in our simulation model after the annealing process. The vortices are labeled as open circles and all the vortices are spread out evenly due to the repulsive vortex-vortex interaction in each configuration. However, as the number of vortices (vortex density) increases, the vortex distribution begins to reflect the underlying moiré pinning pattern.

2.3.3 Critical Current

Critical current is defined as the minimum current required to drive the vortices to move. In our simulation model, a threshold number 40 is set to measure the movement of the vortices. Since the movement of vortices can generate energy dissipation, the critical current is also the maximum current the superconductor can carry without energy dissipation, and therefore it is a very important transport property. In Fig. 2.6(a) we plot the critical current F_c versus θ for the system in Fig. 2.2 at vortex densities of $n_v = 0.25$ to 2.5 in increments of 0.25 . Generally speaking, the critical current decreases with increasing vortex density in superconducting vortex system. The initial peak in F_c at $\theta = 0.0^\circ$ appears due to the fact that when the pinning sites form a triangular lattice, the substrate provides higher pinning effect. We also observe a series of dips at specific angles. Figure 2.6(b) shows F_c versus θ for the

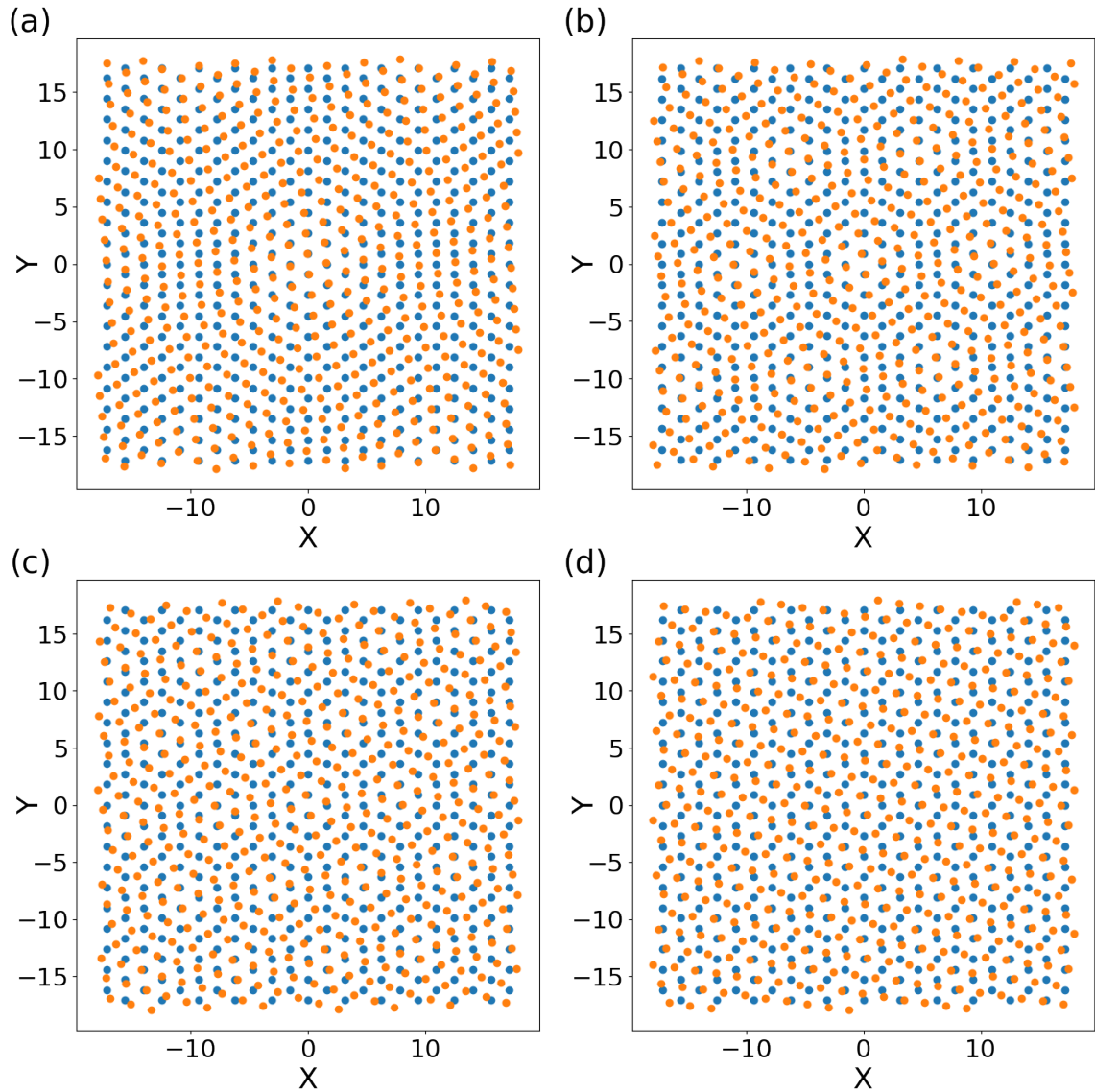


Figure 2.2. The pinning array structures for two triangular lattices where the blue lattice is kept fixed and the orange lattice is rotated by an angle θ of (a) 5.0° , (b) 9.4° , (c) 13.2° and (d) 21.8° .

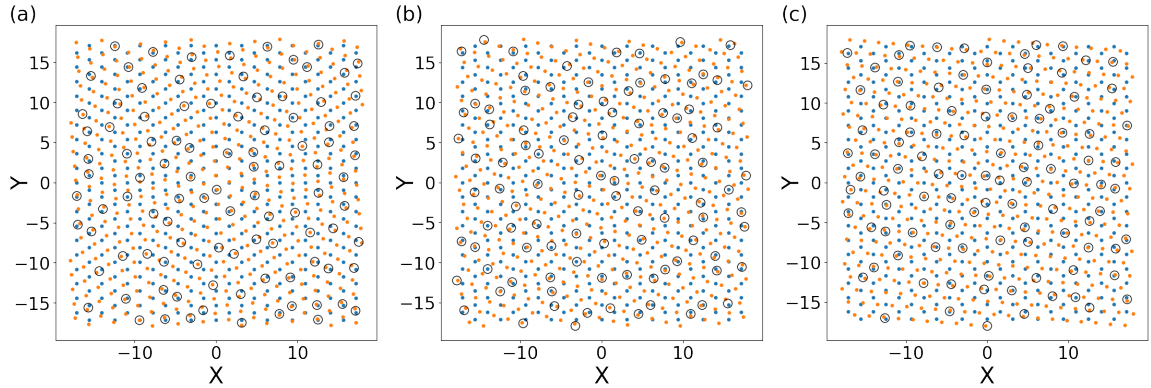


Figure 2.3. Vortex configurations after annealing for a system with 100 vortices (density $n_v = 0.25$) for $\theta = 5^\circ$ (a), 15° (b), and 25° (c). Blue dots: pinning site centers for a hexagonal lattice. Orange dots: a second hexagonal lattice rotated by θ . Large dots: vortices.

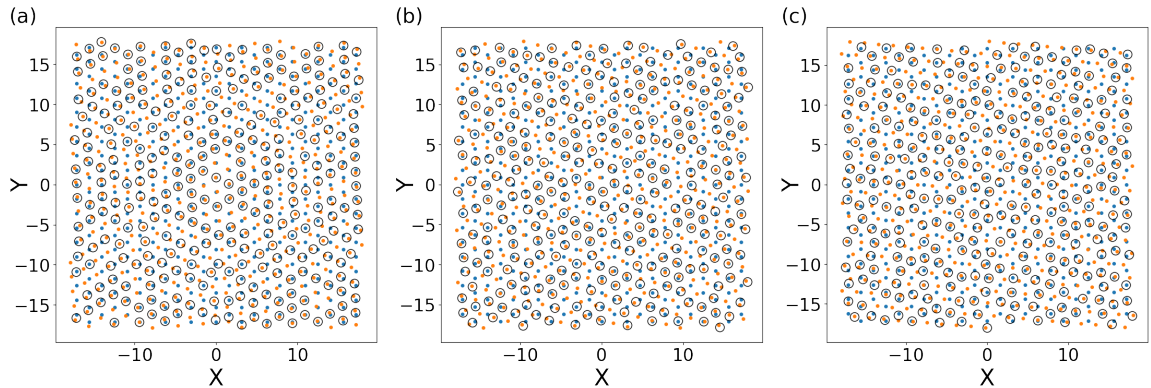


Figure 2.4. Vortex configurations after annealing for a system with 300 vortices (density $n_v = 0.75$) for $\theta = 5^\circ$ (a), 15° (b), and 25° (c). Blue dots: pinning site centers for a hexagonal lattice. Orange dots: a second hexagonal lattice rotated by θ . Large dots: vortices.

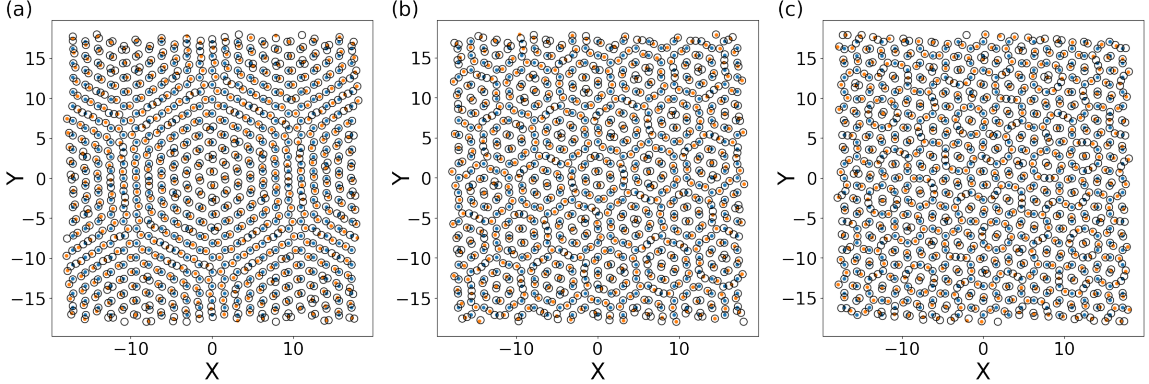


Figure 2.5. Vortex configurations after annealing for a system with 1000 vortices (density $n_v = 2.5$) for $\theta = 5^\circ$ (a), 15° (b), and 25° (c). Blue dots: pinning site centers for a hexagonal lattice. Orange dots: a second hexagonal lattice rotated by θ . Large dots: vortices.

samples with $n_v = 1.25$, where dips in F_c appear at $\theta = 9.4^\circ$, 13.2° , and 21.8° . It has been studied in the past that due to the geometry of triangular lattice, the ordered or commensurate structures in a moiré pattern formed from two triangular lattices occur at the following angles [56, 57]:

$$\cos(\theta) = \frac{3p^2 + 3pq + q^2/2}{3p^2 + 3pq + q^2} , \quad (2.2)$$

where p and q are integers. The values $p = 1$ and $q = 1$ correspond to $\theta = 21.786^\circ$, $p = 2$ and $q = 1$ correspond to $\theta = 13.7^\circ$, and $p = 3$, $q = 1$ corresponds to $\theta = 9.4^\circ$. The critical current dips in our simulation model (Figure 2.6(b)) match these commensurate angles very well.

To verify the correctness of our simulation model and to make sure the pronounced dips are not caused by the periodic boundary condition artifact, we have also tested these results for different system sizes. We find that the angles at which the dips and peaks occur are not sensitive to system size. Fig. 2.7 shows the same critical current plot as a function of the twist angle but with two different system sizes, one smaller

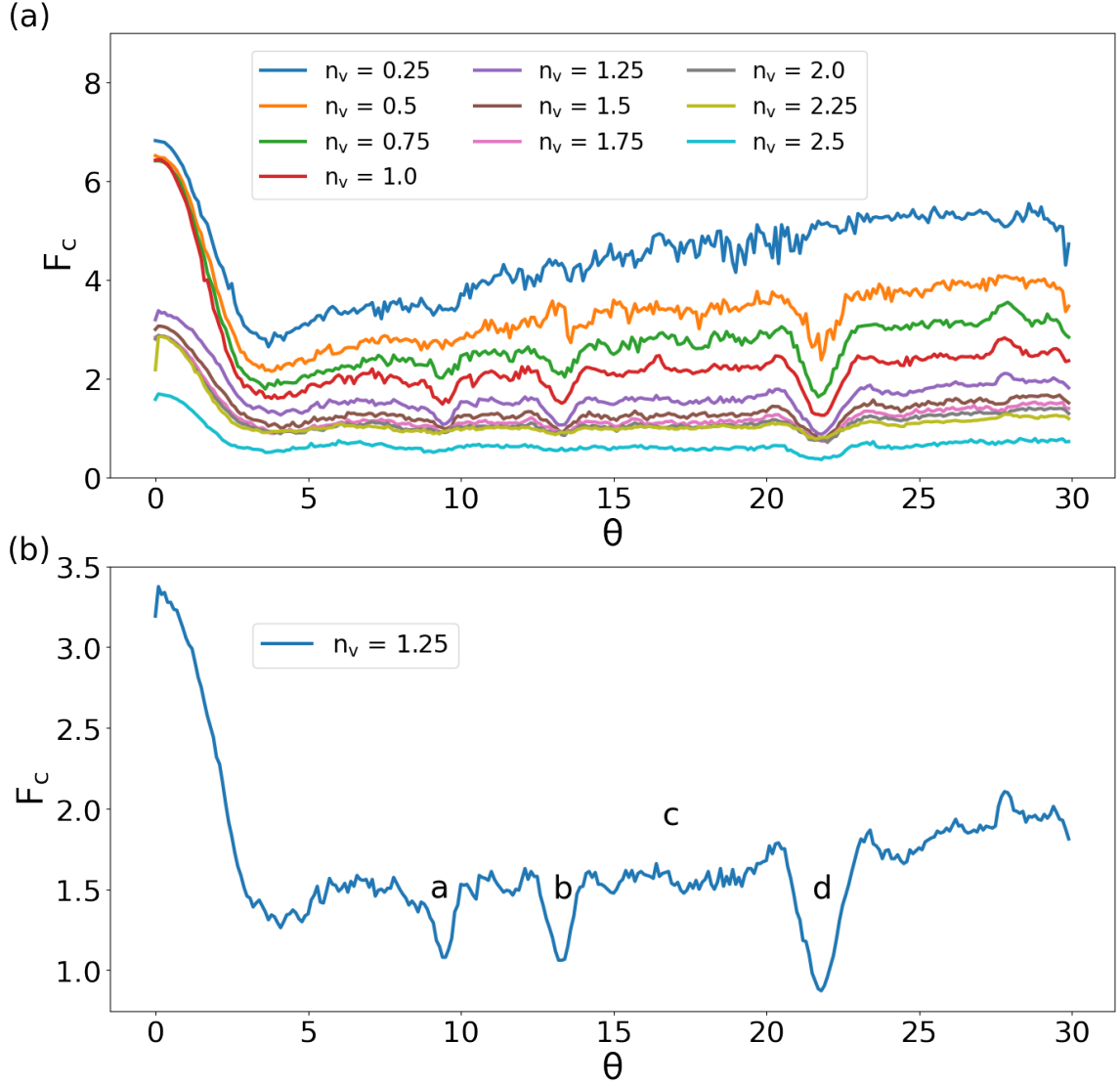


Figure 2.6. (a) The critical current F_c vs θ for the system in Fig. 2.2 at varied vortex densities of $n_v = 0.25$ to 2.5 in increments of 0.25 . (b) F_c vs θ at $n_v = 1.25$, showing dips at $\theta = 9.4^\circ$, 13.2° and 21.8° as well as a peak near 28° . The letters a, b, c, and d correspond to the locations of the images in Fig. 2.8.

and one larger. They both show the same dips as in the system size we initially choose.

2.3.4 Vortex Trajectories

In order to learn more about the vortex dynamics in this system, we plot the vortex trajectories under the driving forces at which the vortices are just able to depin (indicated in Fig. 2.6(b) with letters). As shown in Fig. 2.8, different colors in the plot represent the trajectories of different vortices and the vortices exhibit different dynamical behaviours under different twisted angle θ . Figure 2.8(a) shows the trajectories at $\theta = 9.4^\circ$ and $F_d = 1.5$, where the vortices flow in a series of quasi-one-dimensional channels along the edges of the superlattice. In Fig. 2.8(b), at $\theta = 13.2^\circ$ and $F_d = 1.5$, a similar set of trajectories form in which the motion follows the superlattice edge. Since the superlattice spacing decreases with increasing θ , the number of possible one-dimensional channels for motion increases with increasing θ . In Fig. 2.8(c), the trajectories at a non-commensurate angle of $\theta = 17^\circ$ and $F_d = 2.0$ are much more disordered. At $\theta = 21.8^\circ$ and $F_d = 1.5$ in Fig. 2.8(d), the vortex motion again follows well-defined channels. In general, the flow at incommensurate angles has reduced channeling compared to the flow at commensurate angles.

Some of the peaks in F_c in Fig. 2.6 do not correspond to commensurate angles. In Fig. 2.9(a) we show the pinning site configurations at one of the most prominent peaks near $\theta = 27.9^\circ$ for vortex densities $n_v = 1.25$. At this angle, we find features such as five-fold ordering similar to those observed in quasicrystals[58]. Figure 2.9(b) shows that the vortex trajectories over this substrate just above depinning have strongly reduced channeling. For triangular moiré patterns, the most incommensurate angle corresponds to $\theta = 30^\circ$ [56]. In our system we generally find a small dip in the critical current when $\theta = 30^\circ$, while the peak in F_c falls at $\theta = 27.9^\circ$. The downward shift of the peak location could be a result of the finite size of the pinning sites or of the

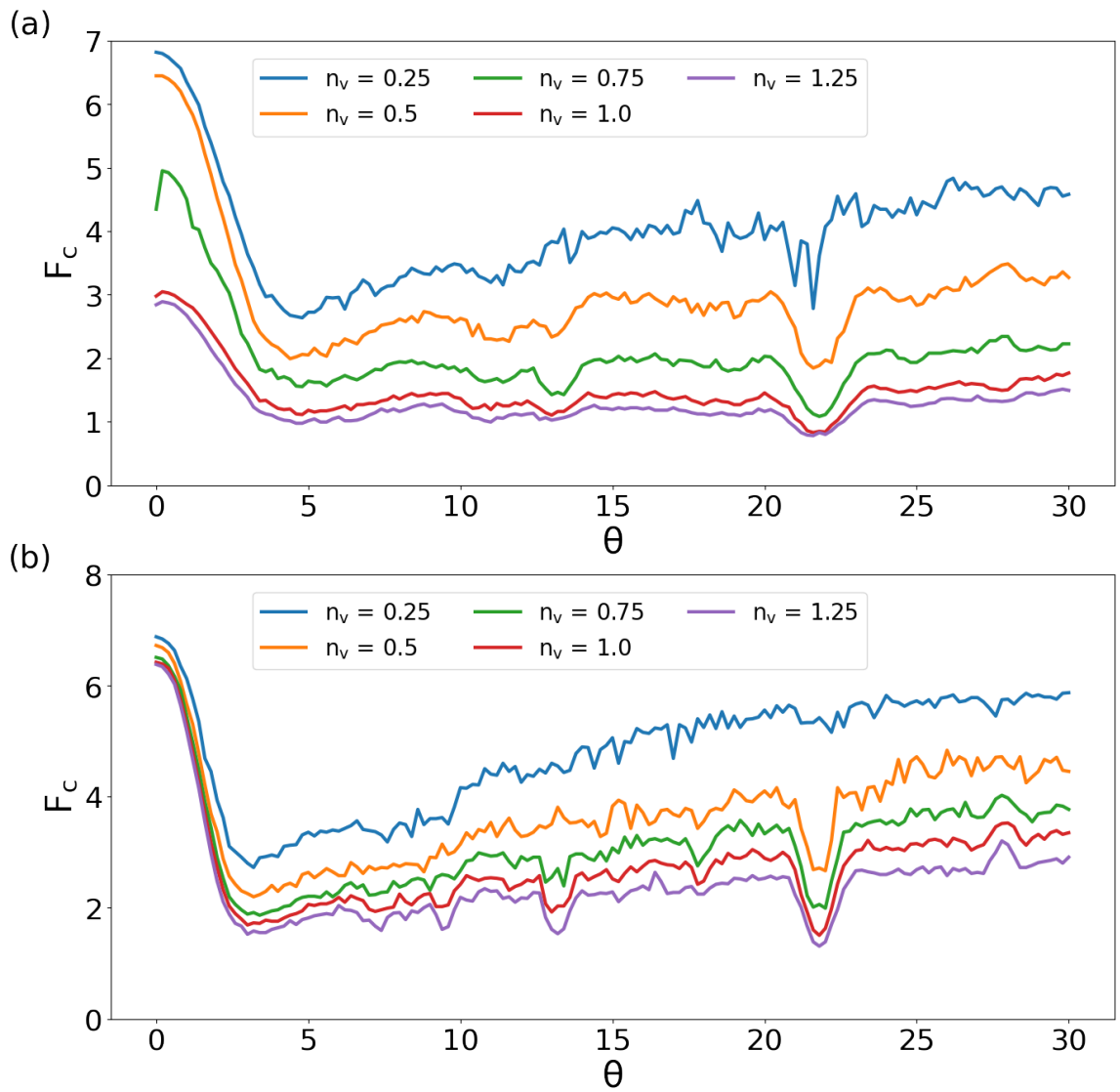


Figure 2.7. Critical current F_c vs θ in samples of size (a) $L = 16\lambda$ and (b) $L = 24\lambda$.

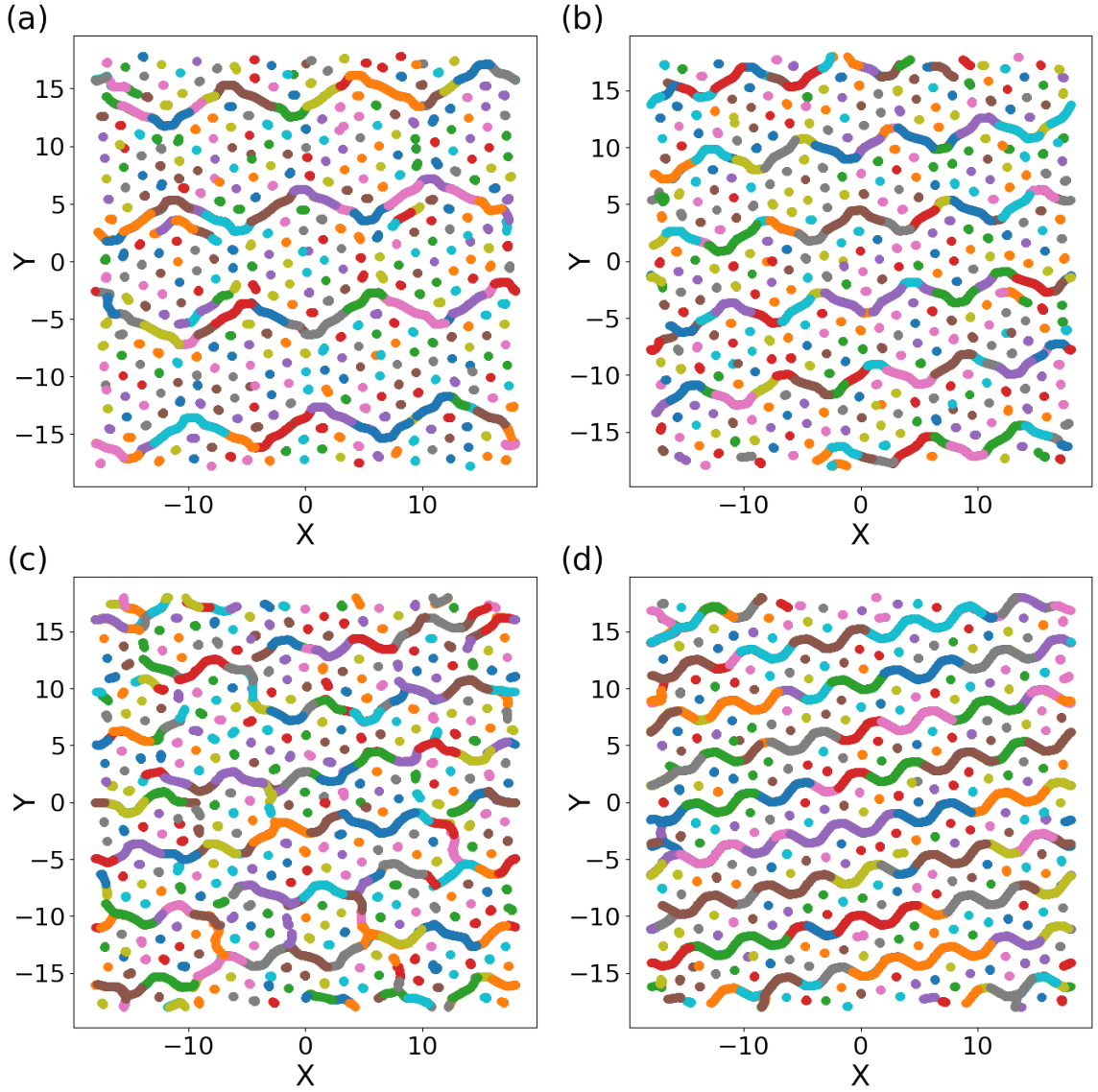


Figure 2.8. The vortex positions (dots) and trajectories (lines) just above depinning for the system in Fig. 2.6(b) with $n_v = 1.25$. Different colors indicate the motion of different individual vortices. (a) $\theta = 9.4^\circ$ and $F_d = 1.5$, where quasi-one-dimensional flow patterns form. (b) $\theta = 13.2^\circ$ and $F_d = 1.5$, with easy flow channeling. (c) $\theta = 17^\circ$ and $F_d = 2.0$, an incommensurate angle showing more disordered channeling. (d) $\theta = 21.8^\circ$ and $F_d = 1.5$, where there is strong channeling.

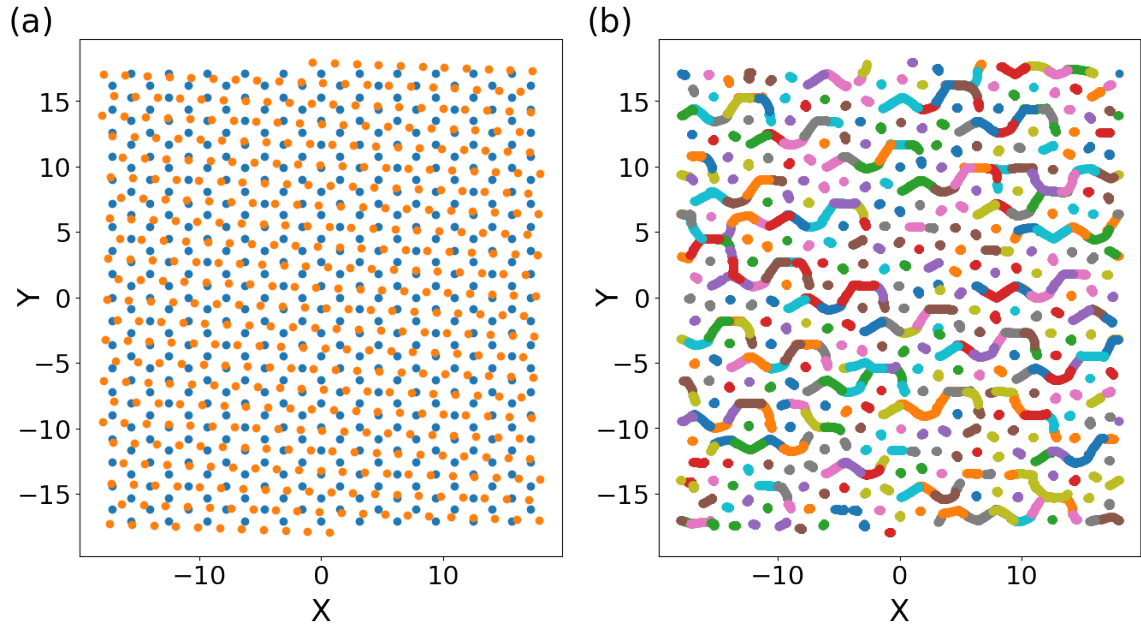


Figure 2.9. (a) The pinning site arrangement for the system in Fig. 2.6(b) at $\theta = 27.9^\circ$ where a peak appears in the critical current near $n_v = 1.25$. Here the substrate has considerable five-fold ordering or quasiperiodic type ordering. (b) The vortex flow pattern over the pinning sites at $F_D = 2.0$, showing a lack of ordered motion. Different colors indicate the motion of different individual vortices.

vortex-vortex interactions which can produce a collectively moving state.

2.3.5 Transverse Motion

The Hall effect is the phenomenon where a voltage is produced transverse to the electric current in the conductor and to an applied magnetic field.[59] In our simulated system, when vortex channeling happens, similar Hall effect or transverse motion occurs. As shown in 2.8, this Hall angle occurs due to the fact that the easy channels flow at finite angles with respect to the driving direction.

In Fig. 2.10 we plot $\langle V_y \rangle$ versus θ for the system in Fig. 2.6(b) at $F_d = 1.5, 2.0, 2.5$, and 3.0 . Peaks in the Hall velocity appear at $\theta = 21.8^\circ$ and 13.7° , with a weaker channeling effect at $\theta = 9.4^\circ$. There is also an extended region from $12^\circ < \theta < 23^\circ$ in which some biased flow in the y direction occurs as F_d increases. The vortex flow is generally more ordered for $\theta < 12^\circ$ even at incommensurate angles since the vortices follow large scale zig-zag patterns, such as is shown for $\theta = 6.6^\circ$ in Fig. 2.11.

2.3.6 Matching Effect

Matching effect occurs when the number of vortices matches the number of pinning sites or underlying potential energy landscape[50, 60]. With commensurate number of vortices, the system usually exhibits lower vortex mobility or higher critical current. Though as shown in Fig. 2.6, the critical current varies significantly as a function of the twist angle θ , we do not find pronounced features as a function of field, or so-called matching effects (Fig. 3.2 shows the matching effects on square pinning array. We will discuss more in the next chapter.). In Fig. 2.12, we show the critical current at three commensurate angles as a function of field. In general, F_c decreases smoothly with increasing n_v as expected. There is only a drop when the number of vortices crosses from less than to more than the number of pinning sites.

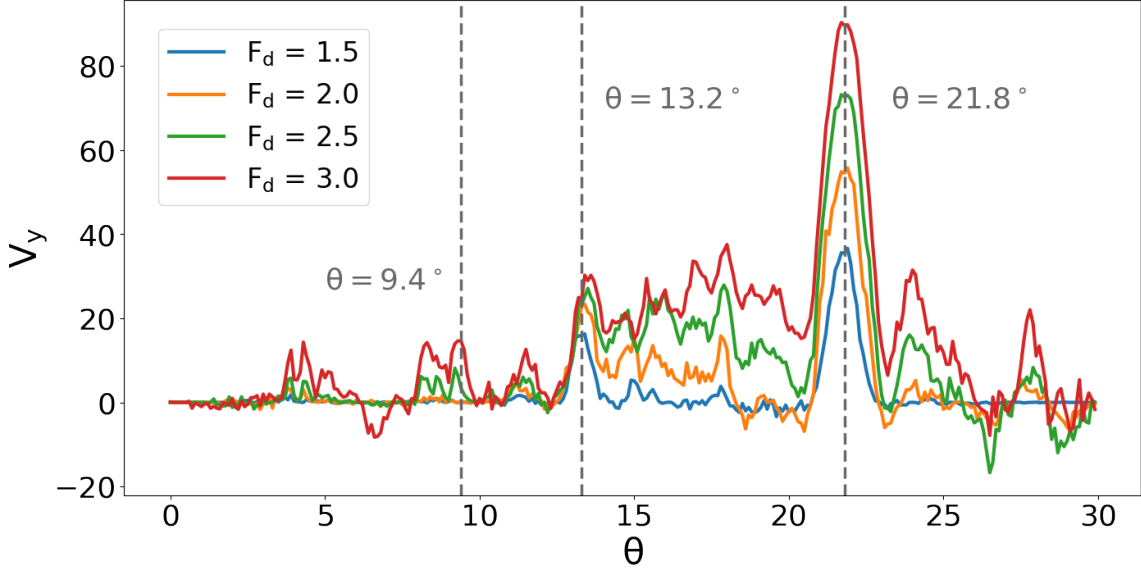


Figure 2.10. The transverse velocity $\langle V_y \rangle$ vs θ for the system in Fig. 2.6(b) at $F_d = 1.5, 2.0, 2.5$, and 3.0 , from bottom to top. There are strong transverse velocities at the commensurate angles, which correspond to the dips in the critical current.

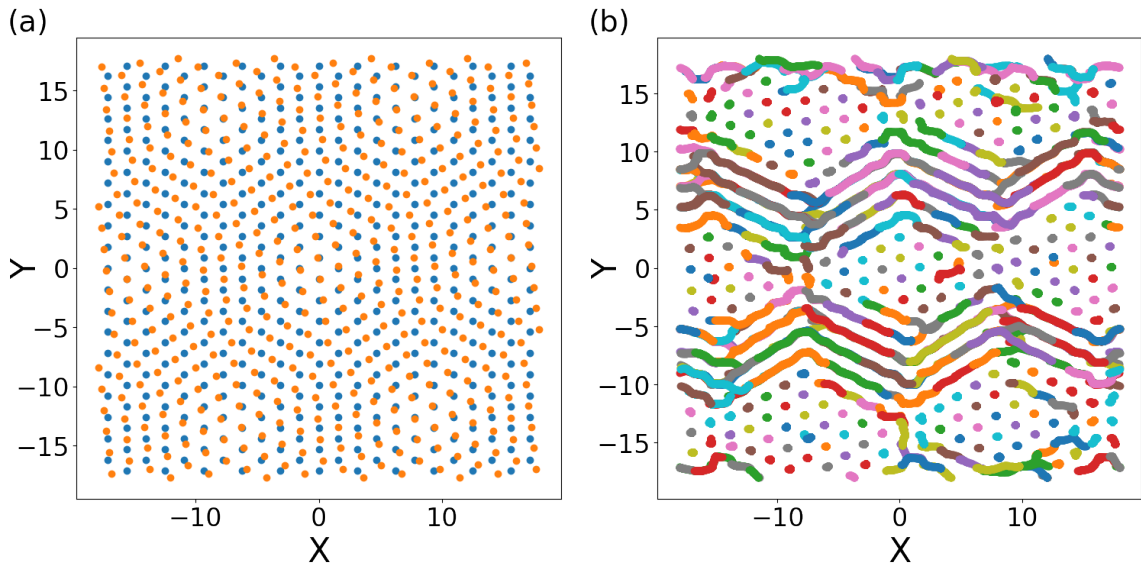


Figure 2.11. Vortex trajectories at $\theta = 6.6^\circ$, $n_v = 1.25$ and $F_d = 3.0$.

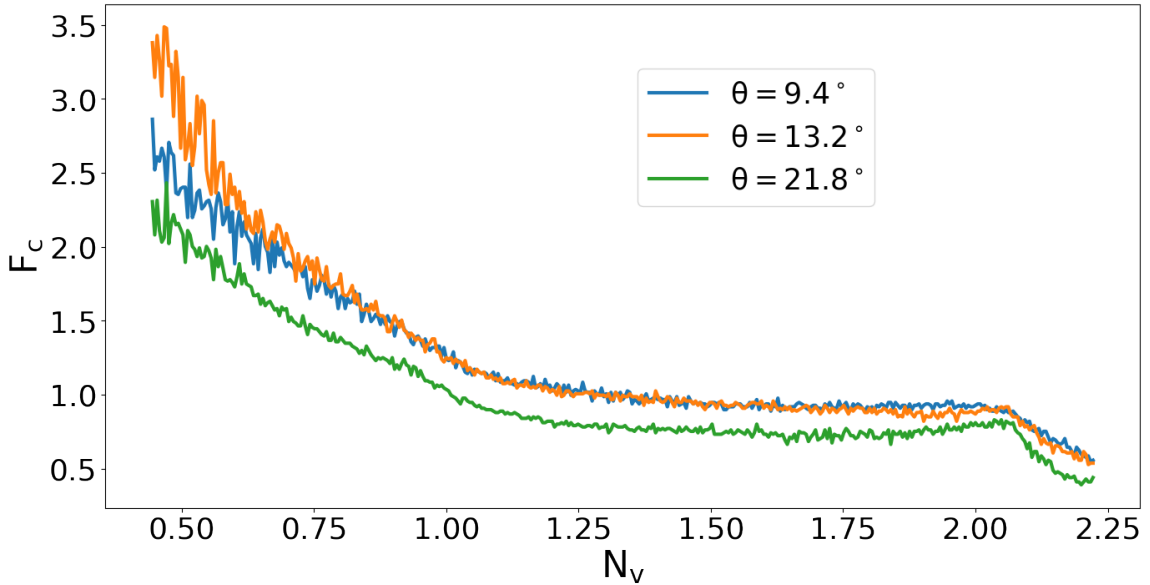


Figure 2.12. Critical current F_c vs magnetic field n_v for $\theta = 9.4^\circ$, 13.2° , and 21.8° . There is a drop in F_c when $N_v/N_p > 2.0$.

2.4 Summary

In this chapter, we examine the vortex dynamics and pinning in a moiré pinning array generated by two sheets of pinning arrays, each forming a triangular lattice. In general the vortex configurations and dynamics are able to reflect the underlying moiré pinning potential. We find that at commensurate angles, the critical current shows pronounced dips because the system enables easy quasi-one-dimensional channeling and the vortices develop transverse motion (Hall effect) along the edges of superlattices. In contrast, at the incommensurate angles the vortex flow is reduced. We also show that at certain angle, the substrate can form a five-fold symmetric or quasiperiodic type array, which suppresses the vortex flow and causes peaks in the critical current profile. Though the vortices exhibit a variety of dynamical behaviours as a function of twist angles, the system does not exhibit much difference with increasing magnetic field or vortex number.

Our results on superconducting vortex system can also be generalized to other particle like systems such as vortices in Bose-Einstein condensates[61], colloidal assemblies[36–39], skyrmions[40], and frictional systems[62].

CHAPTER 3

VORTEX ORDERING AND DYNAMICS ON SANTA FE ARTIFICIAL ICE PINNING ARRAYS

3.1 Overview

In ice phase of water, hydrogen atoms follow the so-called 'ice rules'. For each oxygen atom, there are four hydrogen atoms surrounding it forming the tetrahedral structure. The ice rules require that among the four hydrogen atoms, two of them should be closer to the surrounded oxygen atom and the rest of two being closer to the neighbouring oxygen atoms[63]. (Fig. 3.1 shows the tetrahedral structure of an ice molecule.) The number of configurations conforming to the ice rules grows exponentially with the system size. As a result, even at zero temperature the ground state of water ice is degenerate and the system is called frustrated. Such materials are called spin ices, with "spin" representing the magnetic moment.

However, it's difficult to measure the spin states experimentally without perturbing the system. For this purpose, several experimental groups came up with the idea to use nanoscale magnets to mimic the frustrated behaviour of spin ice[64–66]. The magnetic moment of each island can be described as a single classical spin[67]. The nanoscale magnets can form different patterns of island arrays, including square lattice, brickwork, hexagonal, Santa Fe and others[65, 68–71]. Studies of such arrays have shown that the frustrated interactions can significantly affect the properties of the system[72–74].

Besides the pure magnetic artificial spin ice systems, there are also several studies on hybrid systems of artificial spin ice with interacting particles[75], like colloidal par-

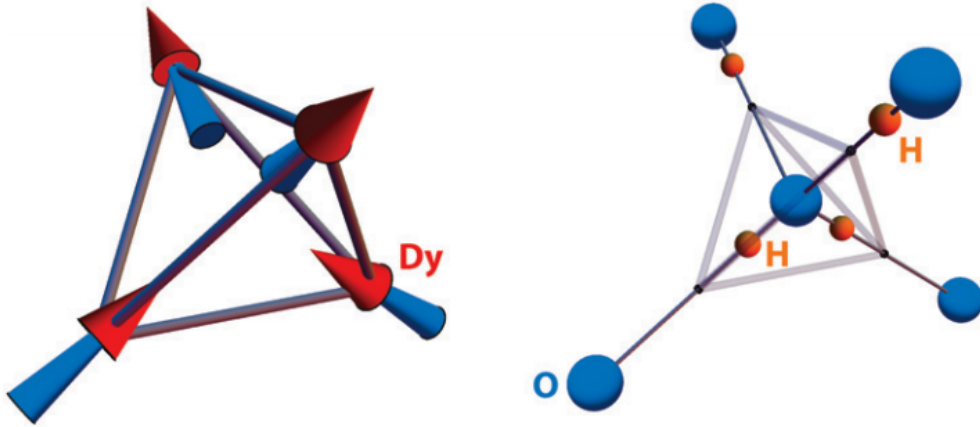


Figure 3.1. Illustration of the mapping between spin ice and water ice. A spin that points outward/inward indicates an hydrogen atom that is displaced away/toward the oxygen atom at the center of the tetrahedron.[3]

ticles coupled with ordered substrate[76–79], magnetic skyrmions[80], and superconducting vortices with nanostructured pinning arrays[4, 7, 51, 52, 81–83]. In Fig. 3.2, we show the experimental results on the system with superconducting vortices coupled with artificial spin ice square lattice array carried out by Kwok et al. from Argonne National Lab[4]. The sample is fabricated using a low temperature type-II superconducting material MoGe with artificial spin ice square lattice arrays of pinning holes. The resistivity response from this sample clearly shows the matching effect, where when the number of vortices (applied magnetic field) is commensurate with the number of pins, the mobility of the vortices is constrained and the system exhibits lower resistance.

In this chapter we focus on an artificial spin ice pattern called the Santa Fe spin ice[5, 68] (Fig. 3.3) interacting with superconducting vortices. As shown in Fig. 3.3(a), one unit cell in the Santa Fe geometry contains four composite squares

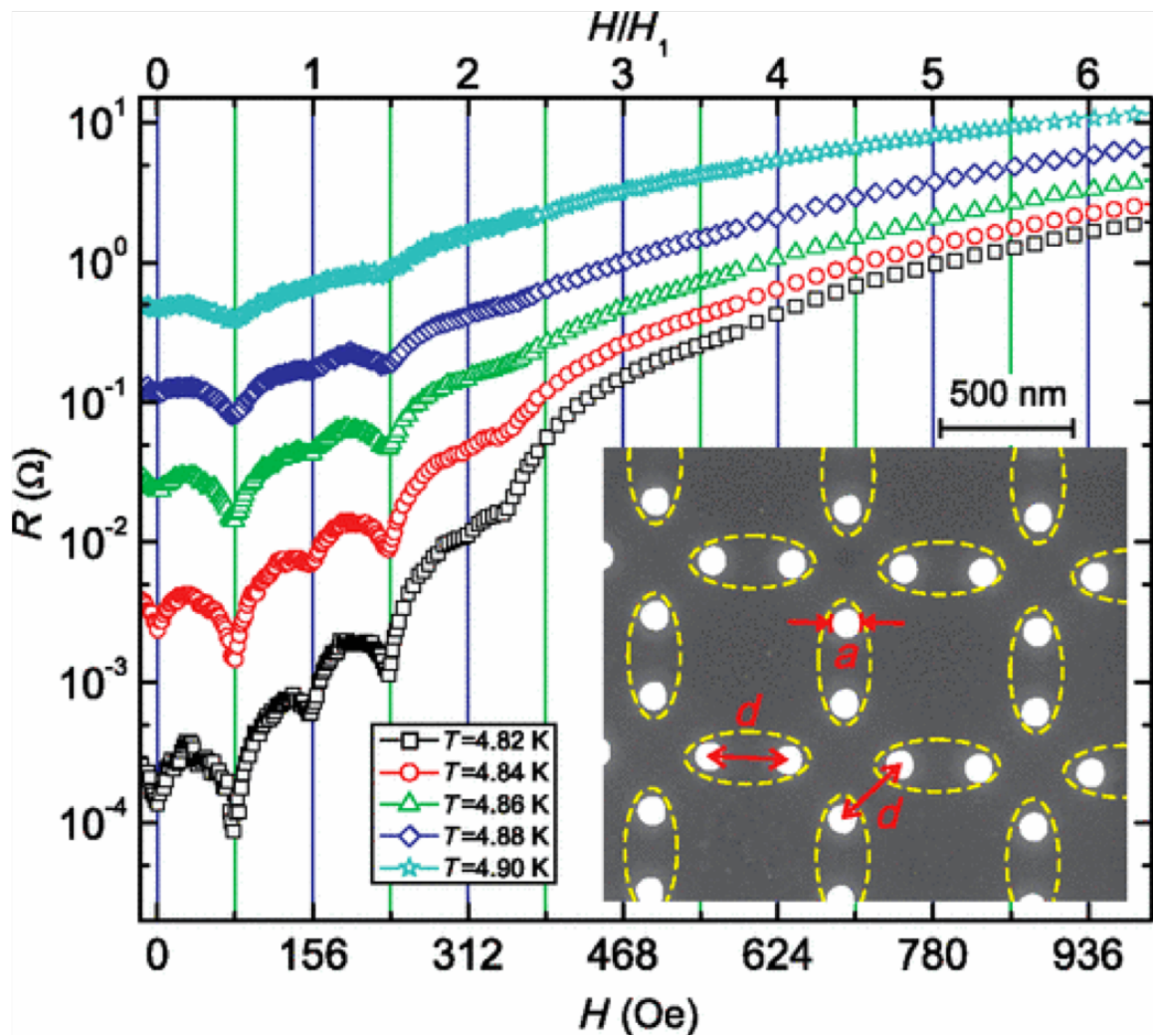


Figure 3.2. Experimental measurement of resistance vs magnetic field on MoGe film with square ice lattice of pinning holes. ($a = 102\text{nm}$ and $d = 300\text{nm}$) Inset shows a scanning electron microscopy image of the square lattice. [4]

and each composite square has eight rectangular plaquettes, which can be classified as two interior plaquettes and six peripheral plaquettes that surround them. There are some interesting properties about magnetic Santa Fe spin ice. For example due to the frustrated geometry, there will always be odd numbers of unhappy (frustrated) vertices in the interior plaquettes and even numbers of unhappy (frustrated) vertices in the peripheral plaquettes[5, 68]. In this chapter, we investigate the vortex configurations and vortex dynamics in a system with a Santa Fe artificial spin ice geometry. We find various distinct vortex patterns with increasing magnetic field or pinning densities. We also compare the results with square lattice and show that the matching effect is much weaker in the Santa Fe geometry and the vortex flow is more disordered.

3.2 Method

The simulation method used in this work is similar to the one described in the previous chapter but with a different pinning pattern. The pinning pattern is shown in Fig. 3.4(a), where the distance between every two pins is set to be $d = 0.825$. For our simulation, we also try $d = 0.4$ and 1.8 for comparison. The number of vortices is proportional to the applied magnetic field B and $N_v = N_p$ corresponds to the matching condition $B/B_\phi = 1.0$, where N_p is the number of pinning sites and N_v is the number of vortices. Periodic boundary conditions are also applied in the simulation. The equation of motion is the same as the one in the previous chapter, Eq. 2.1. The simulation details can also be found in the "Method" section in the previous chapter.

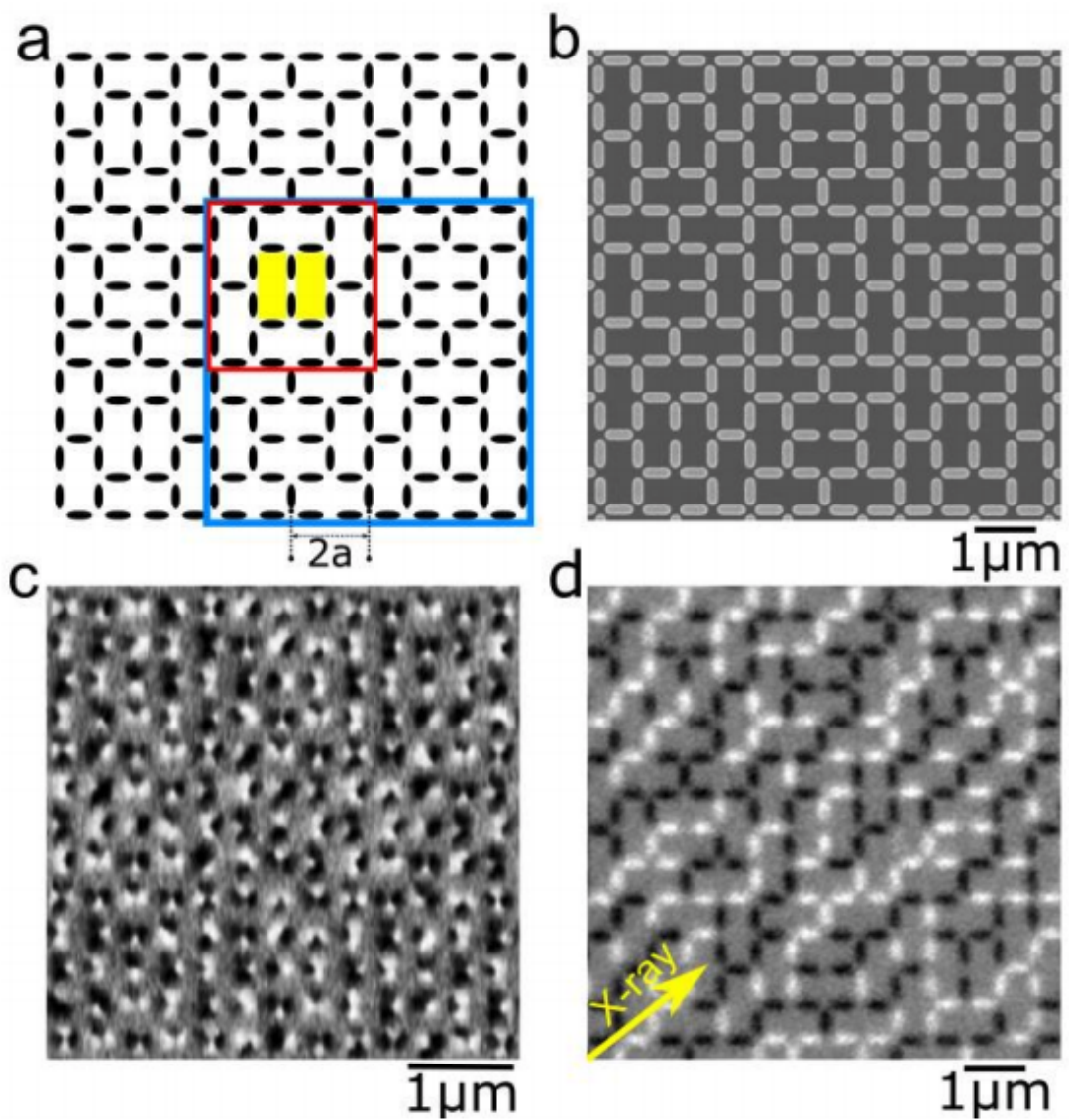


Figure 3.3. (a) Schematic of the Santa Fe ice (SFI) geometry. Experimental images of Santa Fe ice by (b) scanning electron microscopy, (c) magnetic force microscopy and (d) photoemission electron microscopy. [5]

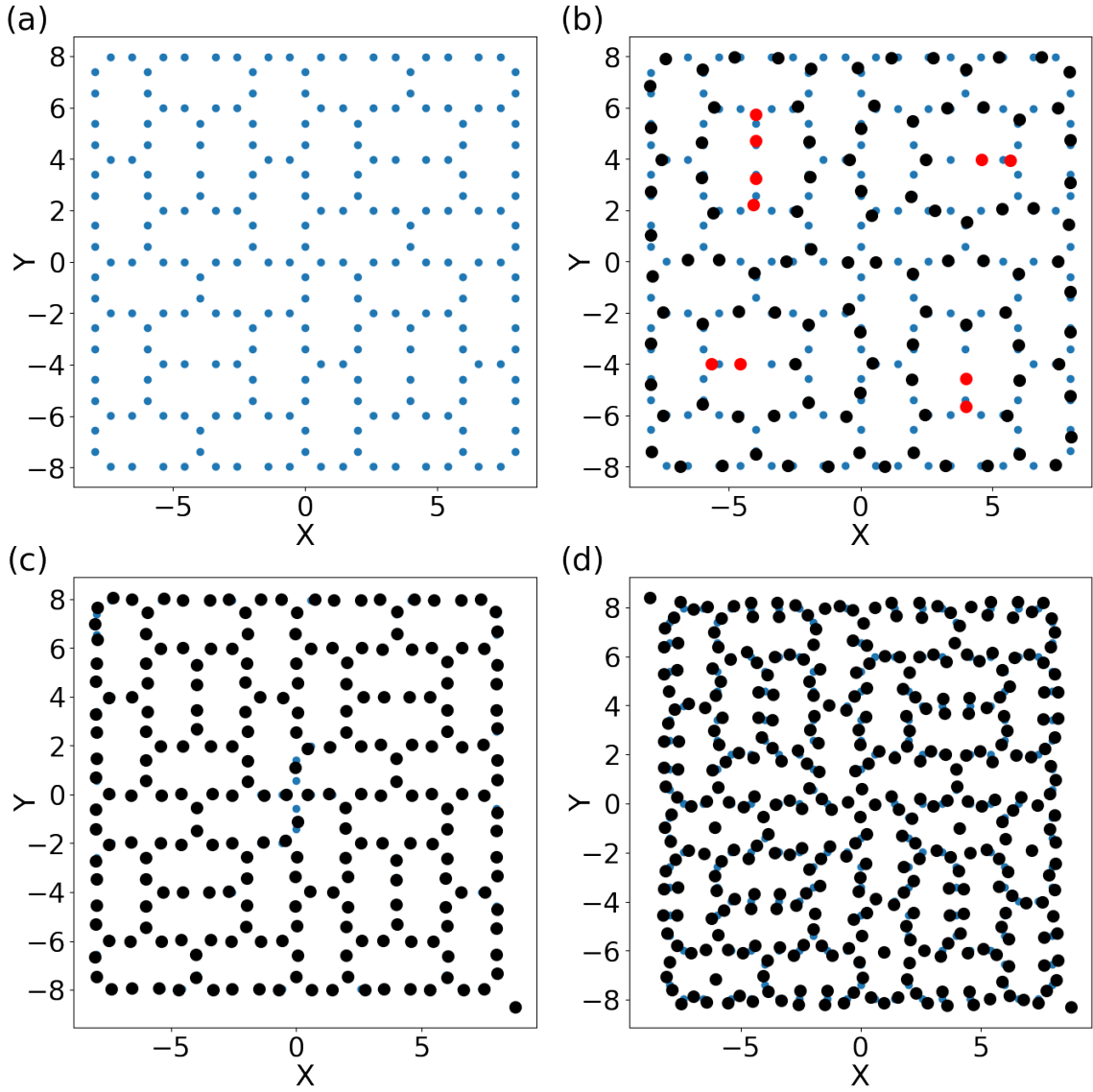


Figure 3.4. (a) Blue dots indicate the pinning sites arranged in a Santa Fe AFI geometry with $d = 0.825$. (b) The vortex positions (black dots) and pinning locations (blue dots) for the system in panel (a) at $B/B_\phi = 1/2$, where the ice rule is mostly obeyed but there are scattered excitations present (red dots). (c) $B/B_\phi = 1.0$. (d) $B/B_\phi = 1.5$.

3.3 Results and Discussion

3.3.1 Ground States

In Fig. 3.4(b)-(d), we show the ground states of vortex configurations in the Santa Fe ice pinning array with $d = 0.825$ after annealing process at $B/B_\phi = 0.5, 1.0, 1.5$. Without the presence of pinning sites, vortices would repel each other and form a triangular lattice[8]. However, when pinning sites are present, the system configuration is an outcome from the competition between vortex-vortex interaction and vortex-pin interaction. As shown in Fig. 3.4(b) when $B/B_\phi = 0.5$, two neighboring pinning sites can be seen as a single double well trap. An individual vortex can occupy either end of the double trap, forming a classical spin pointing either direction. As mentioned in the first section, for each spin ice vertex, the lowest energy state should be two spins pointing out and two spins pointing in. However, for the Santa Fe spin ice there must be vertices with excited configurations given the frustrated geometry[5, 68]. In Fig. 3.4(b), the majority of vortices can form the ground state except in a few inner plaquettes, where two vortices are close together creating a high energy excitation. The overall configuration is similar to the expected ice rule obeying state in the magnetic version of the Santa Fe spin ice[5]. In Fig. 3.4(b), we show the vortex configuration at $B/B_\phi = 1.0$. The vortex configuration reflects the Santa Fe geometry as most of the vortices occupy one pinning site individually. As the number of vortices increases (Fig. 3.4(d)), the geometry begins to get distorted and pinning sites are able capture more than one vortex. There are also cases where vortices are located in the interstitial regions in the middle of the rectangular plaquettes.

3.3.2 Critical Current

In Fig. 3.5(a) we show the critical current (critical depinning force) F_c as a function of the field for the Santa Fe system in Fig. 3.4 and for a square pinning lattice. There

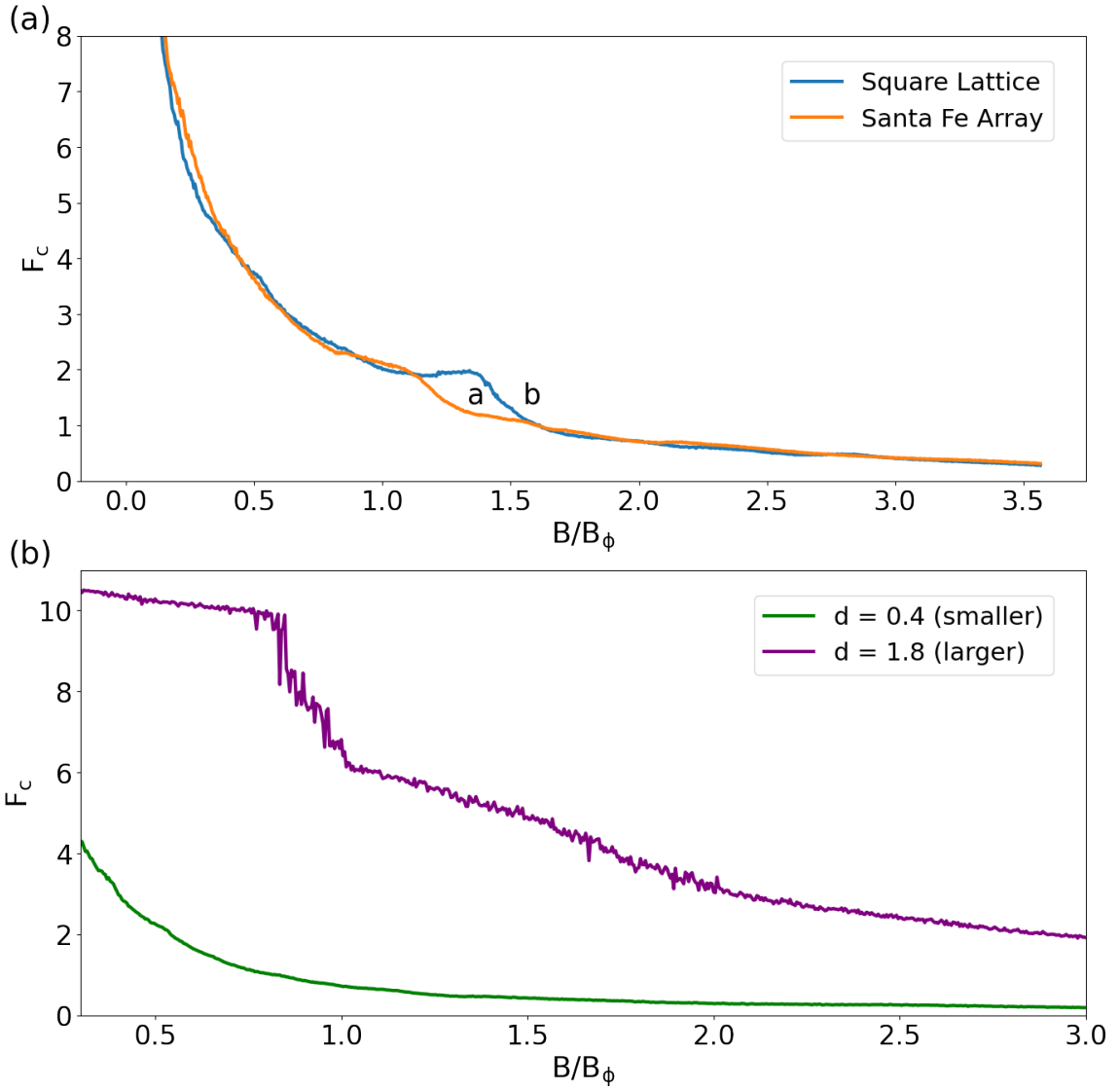


Figure 3.5. (a) The critical depinning force F_c vs B/B_ϕ for the SF system in Fig. 3.4(a) with $d = 0.825$ and for a square pinning array. The matching field B_ϕ is for the SF array; in these units, the matching field for the square array is at $1.286B_\phi$. The labels a and b indicate the values of B/B_ϕ at which the images in Fig. 3.4 were obtained. (b) The critical depinning force F_c vs B/B_ϕ for SF systems with different densities of $d = 0.4$ and $d = 1.8$.

are 288 pins in the square lattice and 224 pins in the Santa Fe lattice. The x axis is normalized by the number of pins for the Santa Fe lattice and the matching field for the square lattice is $1.286B_\phi$ instead of $1.0B_\phi$. There is a clear peak for the square lattice at the first matching field similar to the one shown in Fig. 3.2[4] while for the Santa Fe lattice the peak at the first matching field is much more broadened. Although previous work[18, 84] on the square lattice has shown the matching effect at $B/B_\phi = 0.5$, in our simulation we do not see any peaks either in the square lattice or in the Santa Fe lattice. It can be due to the fact that our simulation is in a different interaction regime. Fig. 3.5(a) shows that the overall pinning strength of the Santa Fe lattice is smaller than that of the square lattice because of the fact that there are fewer pins. However there are several regimes where the depinning force for the Santa Fe lattice is higher than the square lattice. This is because vortices in the square lattice tend to form easy flow one-dimensional channels .

3.3.3 Vortex Flow

In Fig. 3.6(a) and (b), we show the vortex trajectories on Santa Fe and the square lattice corresponding to the field 'a' indicated in Fig. 3.5(a). Due to the matching effect in the square lattice and frustration in the Santa Fe geometry, the vortex flow is more pronounced in the Santa Fe lattice while the vortices are pinned in the square lattice. However as we increase the field (vortex number) to 'b' indicated in Fig. 3.5(a), as shown in Fig. 3.6(c) and (d), the vortices in the square lattice form easy flow one-dimensional channels, while for the Santa Fe array, the motion occurs through a combination of longitudinal and transverse flow channels, so that some vortices move perpendicularly to the driving current direction. This perpendicular movement decreases the overall vortex mobility in the Santa Fe array.

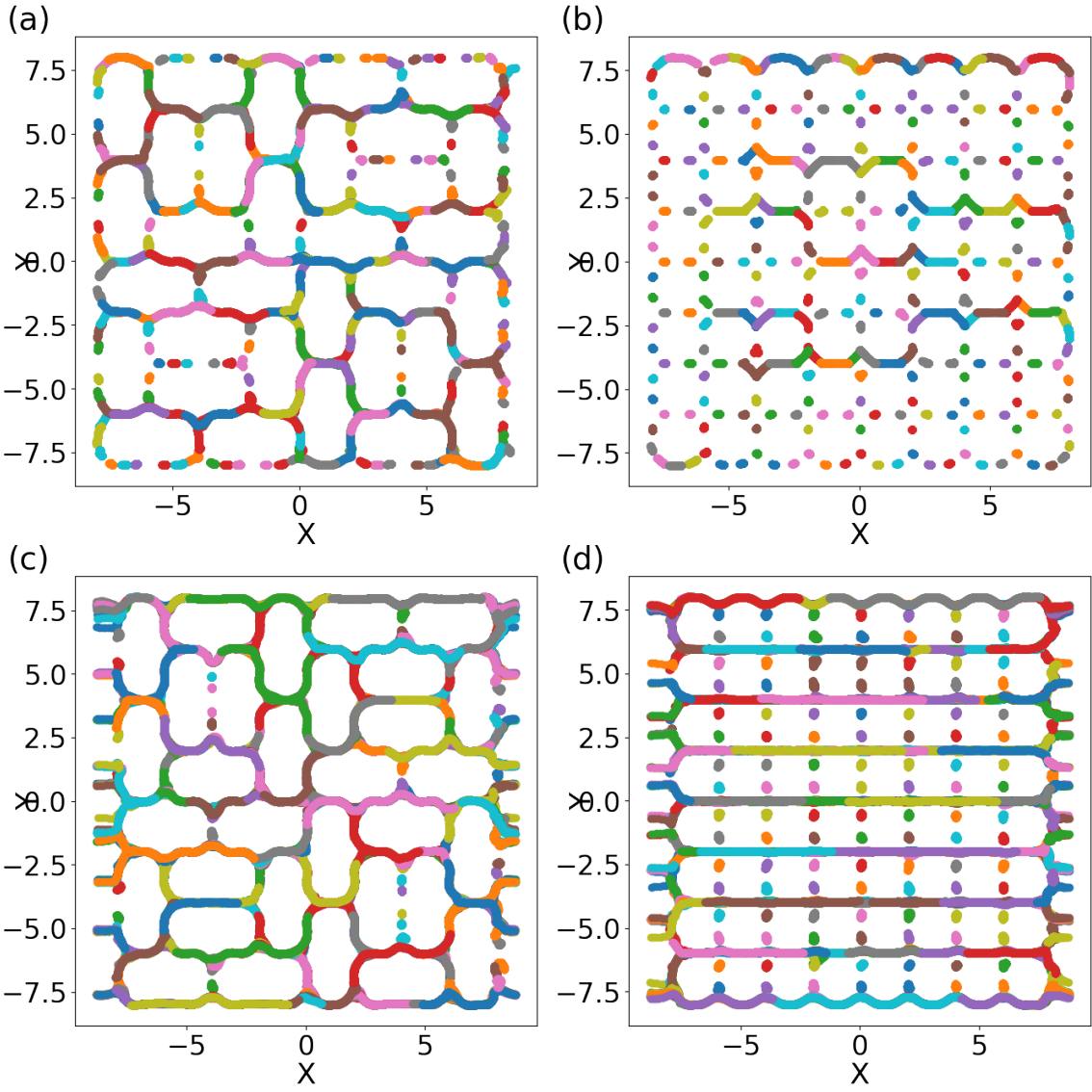


Figure 3.6. The vortex trajectories for the system in Fig. 3.5(a) with $d = 0.825$ at $B/B_\phi = 1.286$ ((a),(b)) and $B/B_\phi = 1.67$ ((c),(d)). (a) and (c) show that above depinning force, the SF lattice exhibits winding labyrinthine flow channels. (b) Under the depinning force, vortices are stuck by the square lattice. (d) The square lattice has easy flow one-dimensional channels. The different colors correspond to different times.

3.3.4 Different Pinning Densities

We also study the Santa Fe lattice vortex systems with different pinning densities. In Fig. 3.7(a), (b) and (c), we plot the vortex configurations for the $d = 1.8$ in the Santa Fe array at $B/B_\phi = 0.5, 1.5, 2.0$. At $B/B_\phi = 0.5$, unlike the vortex configuration in $d = 0.825$, the vortex populations are random and do not form ice rule obeying states due to the decrease in the vortex-vortex interaction. For $B/B_\phi = 1.0$ and 1.5 , there is a combination of doubly occupied sites and interstitial vortices. The vortex configurations for $d = 0.4$ are shown in Fig. 3.7(d), (e) and (f). As the sample size gets smaller, the vortex-vortex interaction becomes relatively larger and the pinning sites begin to overlap. It reduces the effectiveness of the pinning sites by creating paths of low potential along which the vortices can flow. The Santa Fe pattern is destroyed and instead labyrinthine vortex configurations appear.

The critical current for both densities are shown in Fig. 3.5(b) and neither shows any peaks at any matching field, but instead there is a downward step in the larger size system at around the first matching field. The critical current in the sparser system is higher due to the fact that when vortices are far apart, the vortex-vortex interaction becomes weaker and the pinning potential dominates the dynamical behaviour.

3.4 Summary

In this chapter, we show the simulation study on vortex configurations and dynamics in superconducting vortex system interacting with Santa Fe array pinning. Like the previous studies on nanomagnetic Santa Fe spin ice, our results also suggest the pinning geometry forces some vertices to occupy excited states. Especially at the half matching field, most of the vertices are in the low energy ice rule obeying states but a few higher energy vertices exist. In all the pinning densities we examine, the

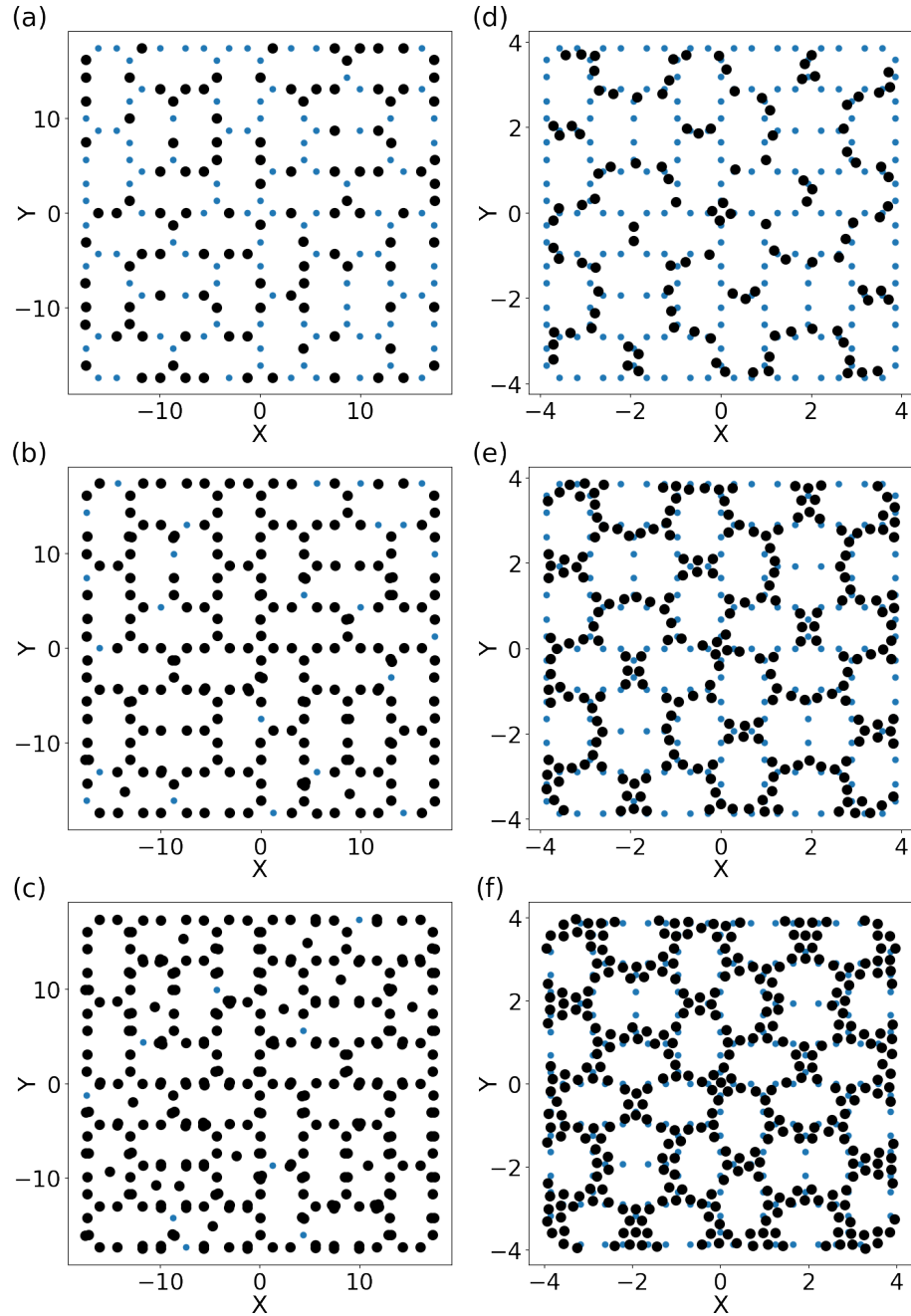


Figure 3.7. (a,b,c) The pinning site locations (blue dots) and vortex positions (black dots) for the system in Fig. 3.5(b) at $d = 1.8$ with weak vortex interactions where the ice rule is lost. (d,e,f) The same for the system in Fig. 3.5(b) with $d = 0.4$, where the pinning sites begin to overlap, creating labyrinth-like vortex states. (a,d) $B/B_\phi = 0.5$. (b,e) $B/B_\phi = 1.0$. (c,f) $B/B_\phi = 2.0$.

critical current profile does not suggest any pronounced peaks like one can observe in the square lattice. For certain magnetic field range, the Santa Fe pinning pattern is more effective than the square lattice because vortices in the Santa Fe array flow both transverse and parallel to the driving direction, while in the square lattice, easy straight parallel channels form.

In superconducting applications the number of pinning sites needs to be kept low, so that the patterning cost stays low. Furthermore, pinning sites/defects can decrease T_c , which is undesirable. For comparable number of pins, the Santa Fe pinning pattern appears to be a more effective pinning configuration than the square one. Consequently, this feature of the Santa Fe pinning configuration is potentially important in designing superconducting devices.

CHAPTER 4

HYBRID MATERIAL OF ARTIFICIAL SPIN ICE AND HIGH TEMPERATURE SUPERCONDUCTOR

4.1 Overview

In the last chapter, we show our numerical simulation results on vortex dynamics and pinning in Santa Fe and square artificial spin ice arrays. For each unit island, both of the two charges are modeled as attractive pinning sites, which correspond the pinning holes in real experiments[4]. However, to fully reproduce the frustrated interactions in artificial spin ices, magnetic charges are necessary, therefore both attractive and repulsive pinning sites should be present[65, 67, 85].

As briefly mentioned in the last chapter, a spin ice is a magnetic substance that has degenerate ground states and is usually subject to frustrated interactions[63, 86]. In recent decades, people found that coupled nanomagnets[64, 65, 67, 87] arranged on different lattices can exhibit similar frustrated behavior and also other interesting phenomena, such as emergent magnetic monopoles, collective dynamics and phase transitions. And therefore these materials are named artificial spin ices. Usually, the motion of emergent magnetic monopoles in an artificial spin system can be controlled with external stimuli such as magnetic and electric fields, strain, temperature gradients and electric currents[7, 83, 87].

Our collaborators from the Superconductivity and Magnetism Group at the Materials Science Division of Argonne National Lab managed to combine the controllable artificial spin ice system with superconductors[7, 87]. The tunable magnetic charges

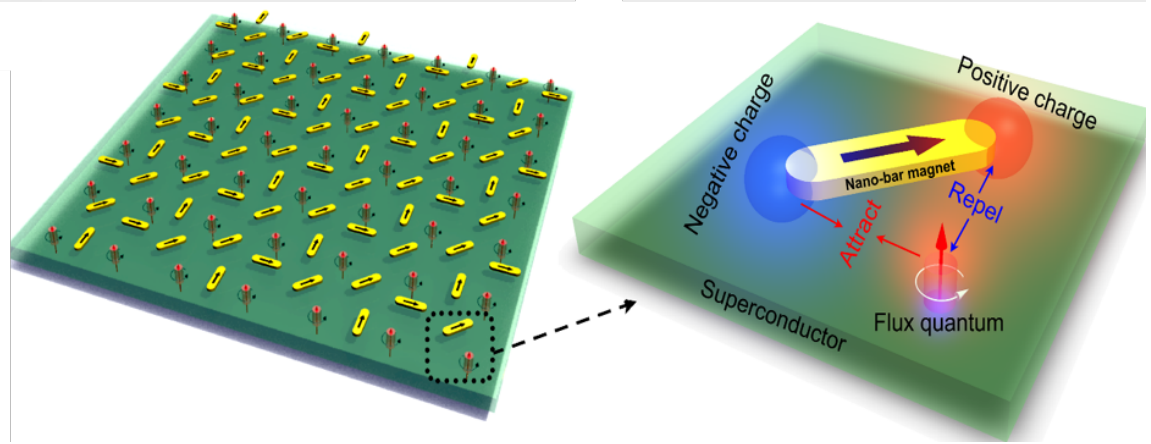


Figure 4.1. Experimental demonstration of the artificial spin ice superconductor heterosystem.

in the artificial spin ice system can interact with the superconducting vortices in the superconductor. Because of the ability to control the nanomagnets *in-situ*, we can switch the flux quanta between frustrated and crystallized states, enabling the control of superconducting critical current profile. A simple demonstration of the experimental setup is shown Fig. 4.1. There are two opposite charges on one nanomagnet, one being attractive and one being repulsive as shown on the right of Fig. 4.1. By tuning the magnetic orientation, the potential energy landscape of the hybrid system can change drastically.

The combination of artificial spin ice and the low temperature superconducting material MoGe has been realized and studied in the past[7]. In this chapter, we focus on the new experimental and simulation results on the high temperature superconductor, $\text{Bi}_2\text{Sr}_2\text{CaCu}_2\text{O}_{8+\delta}$ (BSCCO)[88]. There are three types of magnetic-charge orders that have been investigated in the experiment, as shown in Fig. 4.2(a)-(c), corresponding to type I, II and III. Red and blue circles represent attractive and repulsive pinning sites respectively. Different types of charge orders can be configured

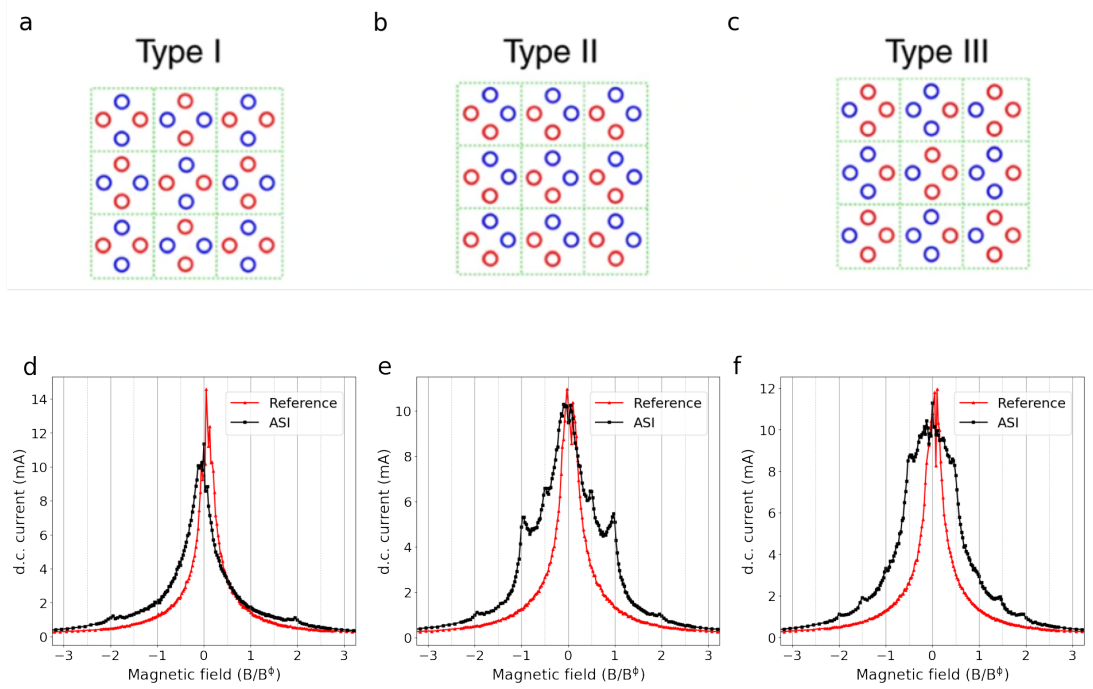


Figure 4.2. (a)-(c) Demonstrations for type I, II and III ASI magnetic charge orders. (d)-(f) The magnetic field dependence of current-voltage characterization under type I, II and III charge configurations

experimentally when the in-plane field is applied at different angles in sequence. The magnetic field dependence of current-voltage characterization under three types of charge configurations is measured by our collaborators. By defining the superconducting critical current I_c when voltages reach $1\mu V$, we obtain the superconducting critical current profile under different magnetic-charge orders, as illustrated in Fig. 4.2(d)-(f).

The magnetic field in X-axis is normalized to the first matching field B_0 , 40 Oe, which corresponds to one vortex every two nanomagnets. The red and black curves represent the reference section and ASI section, respectively. Under all three circumstances, I_c is clearly enhanced by the magnetic pinning generated by ASI, compared to the reference section. For each magnetic charge order, there are kinks emerging at

integer times or half of B_0 , indicating the vortex matching effect and effectiveness of magnetic pinning. It has been reported in the study on MoGe[7] that the matching effect in this system can be explained by the frustrated and crystallized ground states in different charge orders and flux-quantum densities(Please see Fig. B.1 for details). Crystallized ground states can lead to higher system stability and therefore higher critical current. This so-called matching effect can appear as kinks in the critical current profile, as shown in Fig. 4.2. For example, the first matching field for type I configuration is missing because of the frustrated ground state shown in Fig. B.1.

One main difference between BSCCO and MoGe is the critical temperature. BSCCO is one of the high temperature superconductors with critical temperature up to $100K$, while MoGe is a low temperature superconductor with T_c being at about $9K$. Due to the high thermal fluctuation, it has been reported that near the critical temperature, the vortex matter in BSCCO exists as liquid state instead of solid state. [2, 89–91]

Another difference between ordinary low temperature superconductors and unconventional high temperature superconductors is the anisotropy caused by the layered structure in the cuprate materials. For cuprate high temperature superconductors, the superconductiviy happens in the CuO_2 plane and electronic tunneling leads to the Josephson coupling between these planes. Normally this layered structure has dramatic influence on properties of the vortex matter. However in our simulation, the sample can be considered as a 2D material and the vortices can still be modeled as point particles.

It has been experimentally observed by our collaborators that in the liquid state, the resistivity response of the superconductor sample can be controlled by different artificial spin ice charge orders. In this chapter, we focus on the simulation side of this project and show that within our simulation model, the resistivity response indeed can be controlled in the liquid state. Besides the d.c. resistivity response from

the artificial spin ice system, we also study the vortex motion under a.c. current. We show that the ratchet effect exists in such systems, where ratchet motion of flux quanta is induced by an asymmetric potential.

4.2 Method

The simulation method is similar to the ones in the previous two chapters. Here we use molecular dynamics simulation and model the vortex motion on a 2D system with periodic boundary conditions in the x and y directions. The size of the system is $8\lambda \times 8\lambda$, where λ is the London penetration depth.

The equation of motion for vortex i is given by:

$$\eta \frac{d\vec{R}_i}{dt} = \vec{F}_i^{vv} + \vec{F}_i^{P_a} + \vec{F}_i^{P_r} + \vec{F}^d + \vec{F}_i^T$$

This equation is slightly different than Eq. 2.1 due to the existence of attractive and repulsive pinning sites. The interaction energy between the vortices and nanoscale bar magnets pinning sites is modelled as a Gaussian function, where attractive (repulsive) pinning sites have negative (positive) interaction energy. In Fig. 4.3, we show a numerical demonstration of the pinning potential energy landscape with the bar magnets. $\vec{F}_i^{P_a}$ and $\vec{F}_i^{P_r}$ are the gradients of the attractive and repulsive interaction energies, with the form

$$\vec{F}_i^{P_a} = - \sum_{k=1}^{N_{P_a}} F_p R_{ik}^{(P_a)} \exp(-R_{ik}^{(P_a)^2}/r_P^2) \hat{R}_{ik}^{(P_a)}$$

where N_{P_a} is the total number of attractive pinning sites, F_p is the pinning coefficient, r_P is the standard deviation of Gaussian function, $\vec{R}_k^{(P_a)}$ is the center of attractive pinning site k, $R_{ik}^{(P_a)} = |\vec{R}_i - \vec{R}_k^{(P_a)}|$ and $\hat{R}_{ik}^{(P_a)} = (\vec{R}_i - \vec{R}_k^{(P_a)})/R_{ik}^{(P_a)}$. $\vec{F}_i^{P_r}$ has the same form as $\vec{F}_i^{P_a}$ but with the opposite sign.

The simulation starts from a high temperature where vortices are in a molten

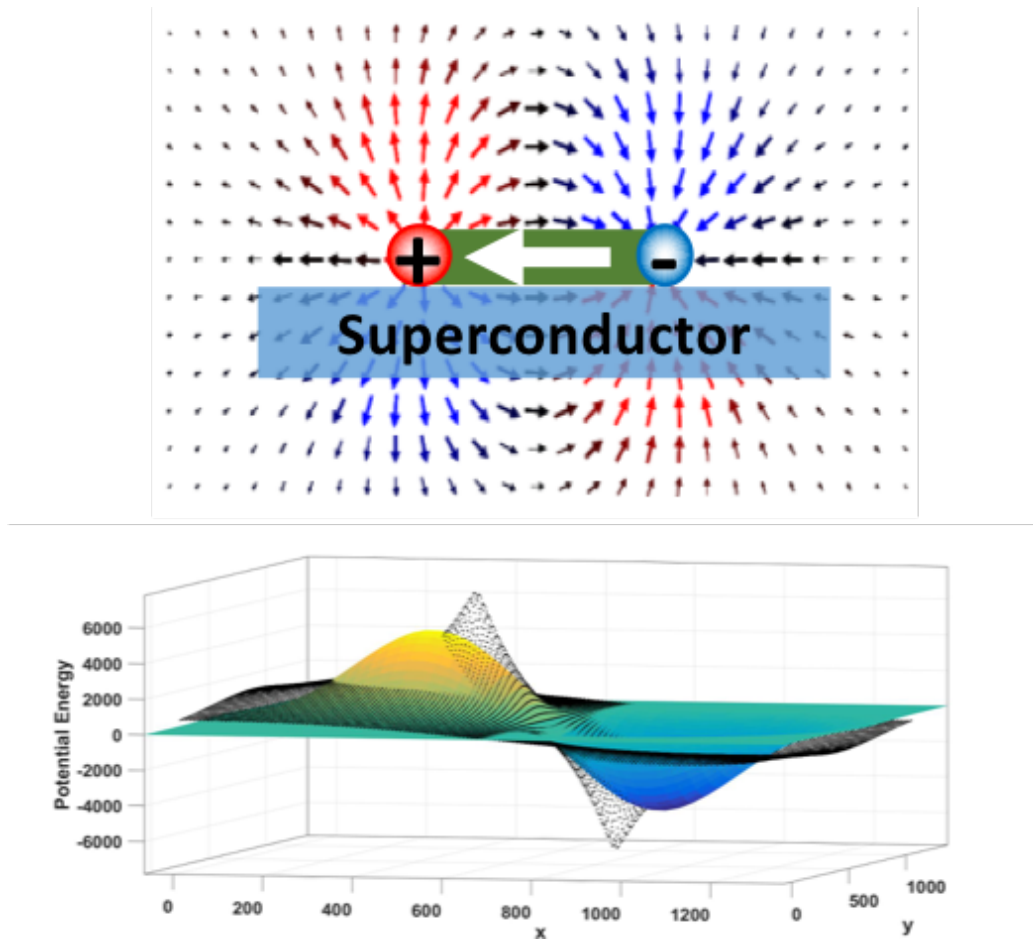


Figure 4.3. Demonstration of pinning potential energy landscape with nanoscale bar magnets.[6]

state and the temperature decreases slowly to 0K with 100 intermediate intervals, where we let the system evolve 10^5 steps during each interval. After the annealing process, we obtain the ground states as the initial vortex configurations. To get the d.c. resistivity responses in different ASI configurations, we drive the vortices under various temperatures with a constant current drive. As for the a.c. ratchet effect, we drive the systems using alternative current drives with different amplitudes and periods. After combining the data points, we obtain phase diagrams as shown in Fig. 4.9.

4.3 Results and Discussion

4.3.1 Vortex Liquid State

Normally in low temperature superconductors, vortex matter exists as solid state. But in our simulation, we want to simulate the high thermal fluctuation in BSCCO and measure the melting temperature. For this purpose, we exclude all the bar magnet pinning sites and measure the average standard deviation of all the vortices with increasing temperature. In Fig. 4.4(a), we show the average standard deviation in the system as a function of the unitless effective temperature. The standard deviation increases in general with increasing temperature but gets to a maximum value approximately when $T > 10$ due to the finite size constraint of the system. The liquid state can be classified using the Lindemann criterion[89, 92]. We can say for sure, that when the average standard deviation of all the vortices is comparable to the lattice size, the vortex solid state turns into liquid state. In our simulation model, it happens at about $T = 2.4$. In Fig. 4.4(b)-(g), we show the vortex movement trajectories at $T = 0.1, 0.5, 1.0, 2.0, 3.0, 4.0$. Below $T = 2.0$, we can clearly see that the system maintains the crystallized structure. As the temperature gets higher, above $T = 3.0$, the vortices have enough energy to break through the energy barrier and

the system turns liquid. The vortex trajectories further confirm the same conclusion as from the Lindemann criterion.

4.3.2 Resistivity Response

After we calibrate the effective temperature, we want to answer the question whether we can control the vortex flow in the vortex liquid state. Fig. 4.5(a) shows the different resistivity responses on three types of artificial spin ice configurations in the experiment carried out by our collaborators. Between $80K$ to $85K$, we can see the splitting between different artificial spin ice configurations and above $90K$ all the samples turn from superconducting phase to normal phase. It has been reported[2, 89–91] in the past by multiple research groups that near T_c , the vortex matter in BSCCO exists as the liquid state. So even though the splitting is tiny, our experimental data does suggest the ability to control the vortex flow in vortex liquid state by applying different magnetic energy landscapes.

By applying a d.c. current driving force in our simulation model, Fig. 4.5(b) shows the simulation results on the resistivity response from three types of ASI configurations as a function of the effective temperature. The simulation also indicates the splitting between different configurations. Remember from the last section, above $T = 2.4$, the system turns into vortex liquid. So in the majority of temperature scale, the vortices in our simulation model exist as a vortex liquid. Qualitatively speaking, both our experiment and simulation suggest the same pinning effect ordering. Type I configuration has the weakest ability to pin vortices among the three configurations in the vortex liquid state while type III can pin the vortices most effectively.

Normally, MD simulation model resides in the limit where each vortex is considered as a hard particle. Therefore it cannot simulate the phase transition from superconducting state to normal state. As shown in Fig. 4.5, though both the simulation and experiment resistivity responses show near flat behaviour in the high

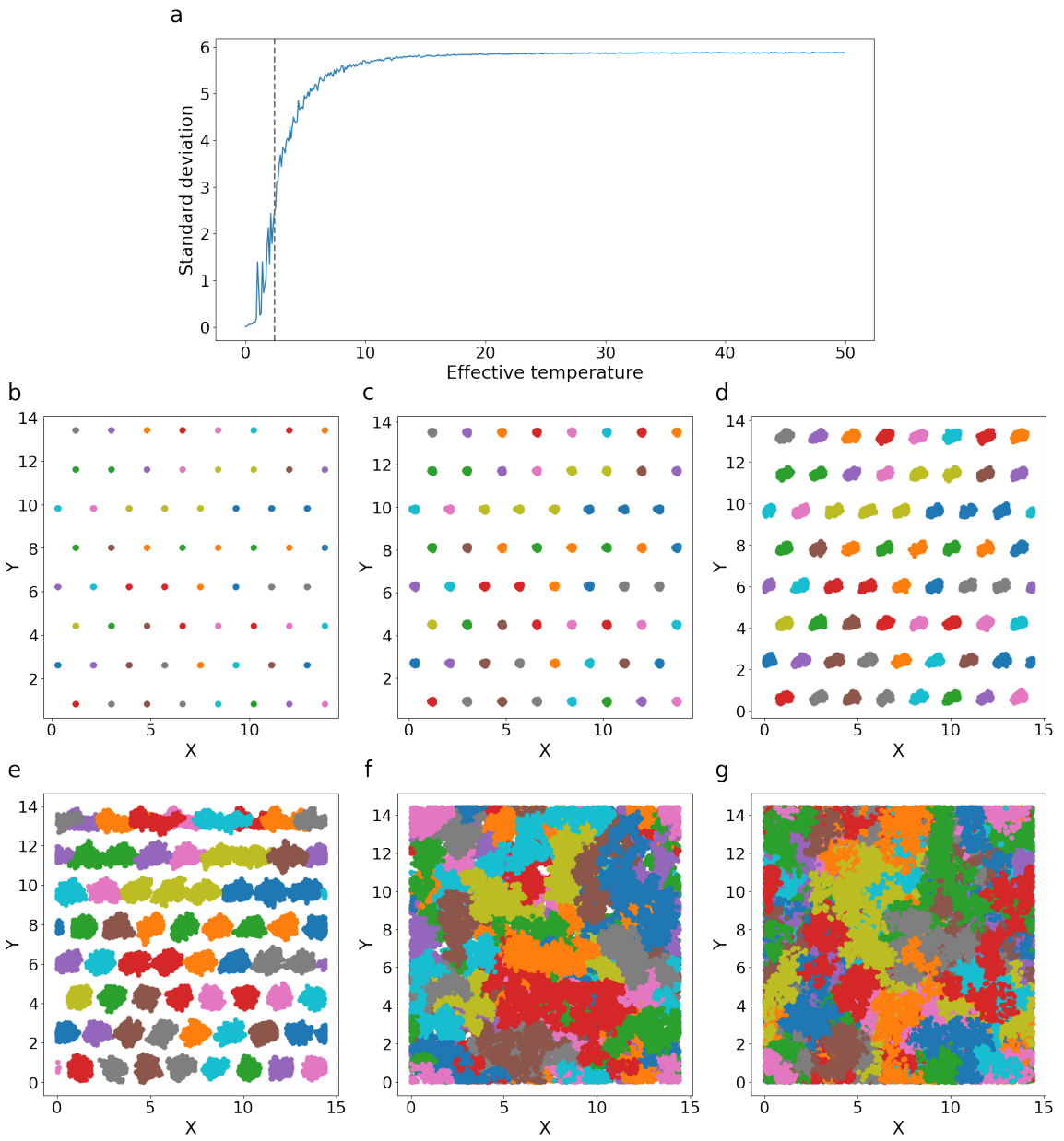


Figure 4.4. (a) Average standard deviation of vortices as a function of effective temperature. The dashed line $T = 2.4$ indicates when the standard deviation is comparable to the vortex lattice distance. (b)-(g) Vortex movement trajectories at $T = 0.1, 0.5, 1.0, 2.0, 3.0, 4.0$. The melting happens between 2.0 (e) and 3.0 (f). Different colors represent the trajectories of different vortices.

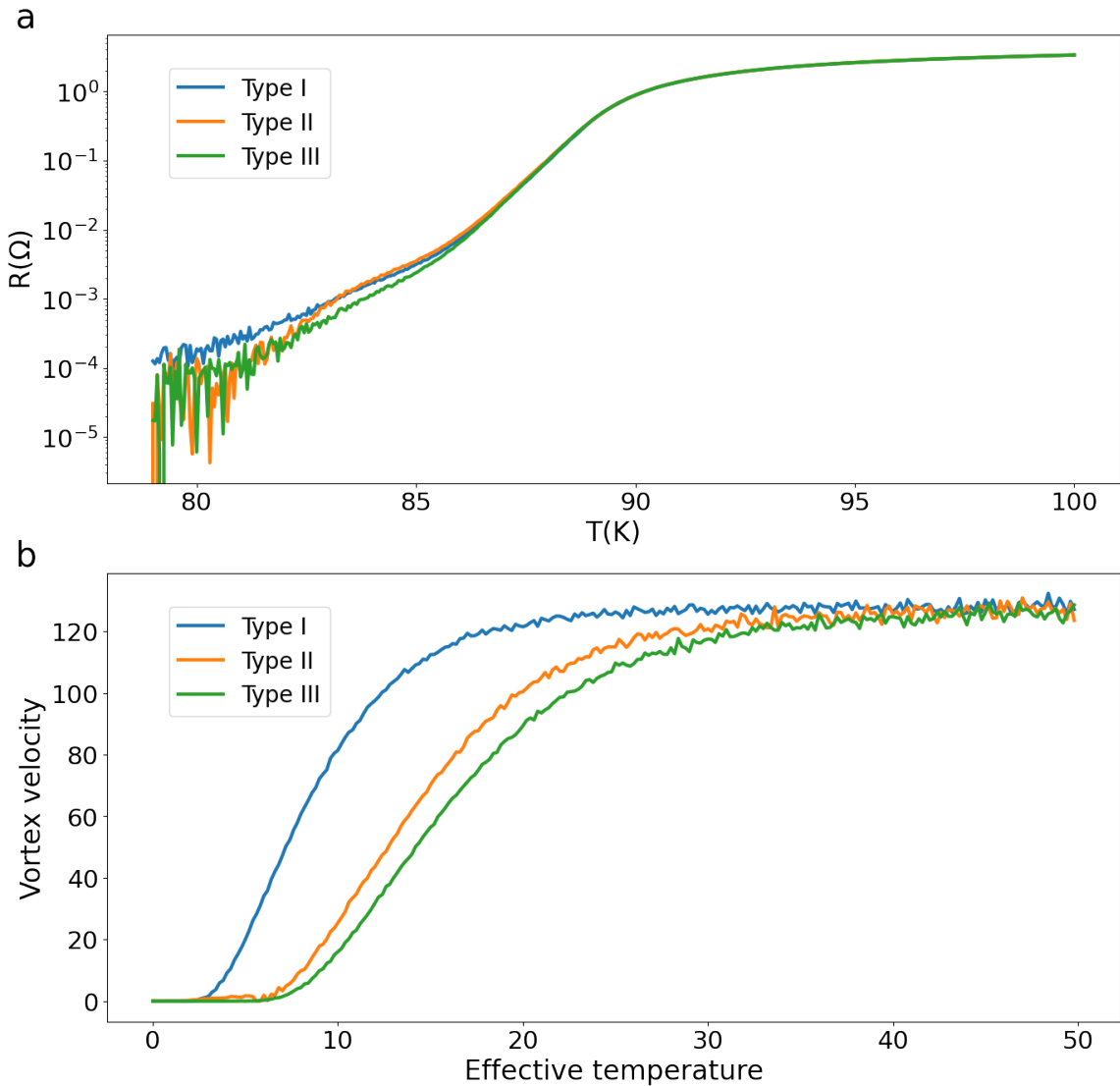


Figure 4.5. (a) Experiment and (b) simulation results on resistivity responses from three types of ASI configurations on BSCCO.

temperature regime, the simulation one indicates that with such high temperature fluctuations the magnetic energy difference between ASI configurations can be ignored, while the experimental one indicates the phase transition from superconducting state to normal state. Nevertheless, our simulations agree with experiments that the vortex flow in superconducting liquid states indeed can be controlled by different magnetic field landscapes produced by nanoscale bar magnets.

4.3.3 Vortex Ratchet Effect

The ratchet effect in vortex matter can appear when the system is driven by alternative current and the underlying pinning landscape is asymmetrical[93–95]. The net movement of the vortices is in one of the directions parallel to the a.c. source and as a whole the system generates a net d.c. voltage. It has been reported with 1D asymmetrical pinning potential, this mechanism can be used to remove vortices from low temperature superconductors[93]. With our 2D artificial spin ice hybrid system, the experiment also suggests such asymmetric movements from the vortices.

In Fig. 4.6(a), we show the schematic of the experimental setup. A.c. current source is applied to the sample and a d.c. voltage meter is used for d.c. voltage detection. Fig. 4.6(b) shows the measurement on type I configuration and we do not observe any d.c. response from type I configuration as expected, since type I configuration is symmetrical for the vortex movement both from left to right and from right to left.

However, for type II and type III configurations, the pinning potential landscapes are not symmetrical, as shown in the insets in Fig. 4.6. The d.c. voltage is measured as a function of the applied magnetic field and the a.c. current amplitude. For type II configuration, we can see a clear pattern at the second matching field while for type III configuration, the bright spot locates at the first matching field, and there are some weaker signals elsewhere. The magnetic charges in (d) and (f) are reversed

compared to those in (c) and (e), respectively. So we can see the complete opposite signals.

With molecular dynamics simulations, we are able to reproduce the ratchet effect observed in the experiment. In Fig. 4.7, we show the simulated d.c. response as a function of a.c current amplitude and magnetic field under type II and type III configurations. The simulation results match the experiment very well. We also observe the bright pattern at the second matching field for type II configuration and at the first matching field for type III configuration. The simulation also reproduces the reverse ratchet effect for type III configuration between the first and the second matching field, which is caused by the disordered vortex-vortex interaction[96–98]. The match between simulation and experiment further verifies our simulation model. As for type I configuration, there is no pattern both in the simulation and the experiment.

All the results shown previously are measured at a given a.c. current frequency. But the ratchet effect should also be highly correlated with the input a.c. frequency[93]. In Fig. 4.8(a), we show the simulation results on the d.c. voltage response in type II ASI configuration at the first matching field as a function of the a.c. driving current amplitude and period ($1/frequency$). We obtain a very interesting phase diagram with finger-like structure. Similar finger-like structures have been reported[93, 97] but with a different 1D asymmetric pinning potential. The reason for this structure is because when a.c. current drive is applied, the vortices also move in an alternative manner. But because of the existence of asymmetric magnetic potential, the distances a vortex can travel towards two opposite directions are different.

In Fig. 4.8(b)-(d), we show the vortex trajectories corresponding to "b" - "d" labelled in Fig. 4.8(a). In Fig. 4.8(b), when the applied current is too small, the vortices are not able to get out of the potential wells so they are all trapped in each cell. But with a fixed frequency and a slightly larger a.c. current amplitude (Fig. 4.8(c)), the vortices now can jump out of one side of the potential well but

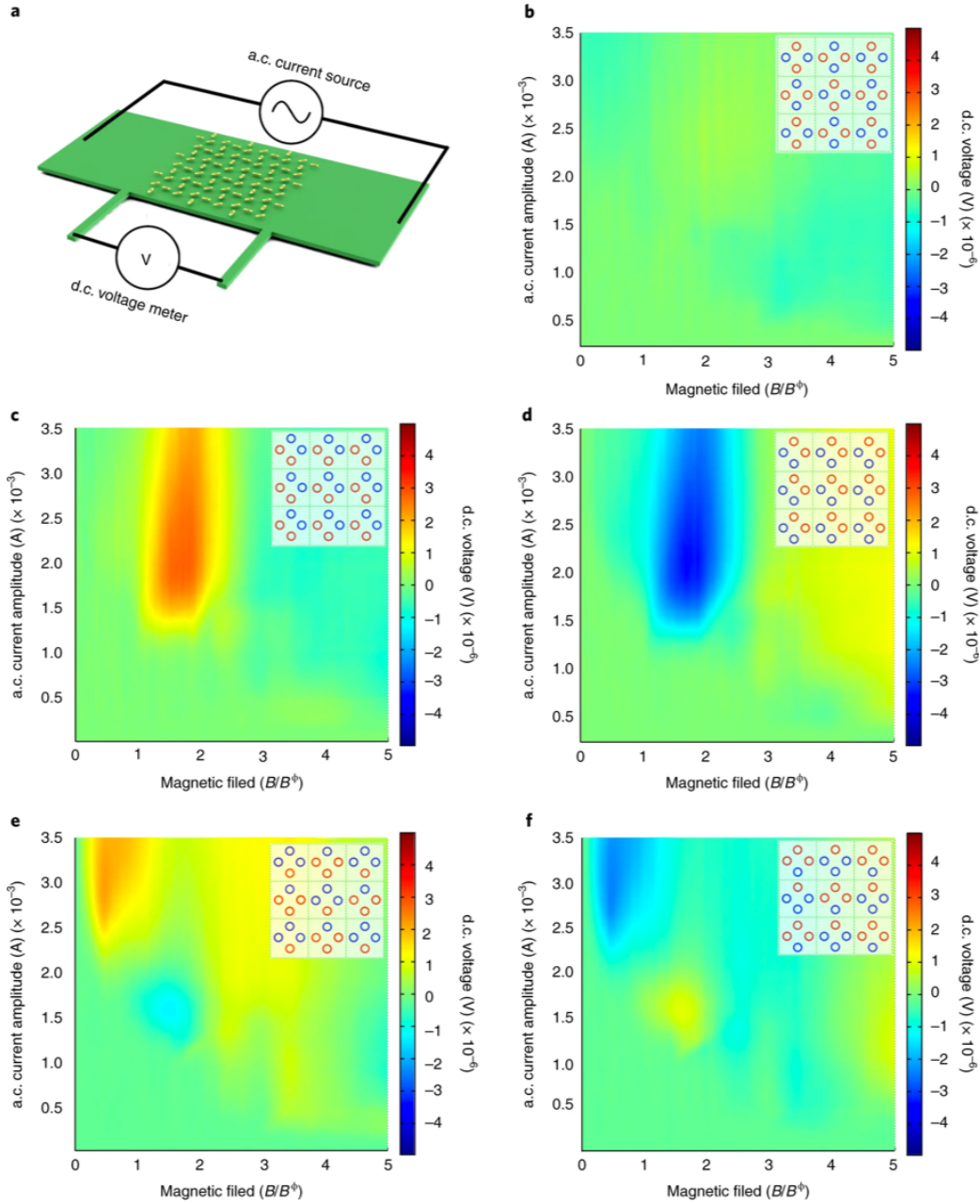


Figure 4.6. (a) Schematic of the experimental set-up with a.c. current drive and d.c. voltage detection. (b)–(f) Colour maps of the d.c. voltage response as a function of the a.c. current amplitude and magnetic field under the type I (b), II ((c) and (d)) and III ((e) and (f)) magnetic-charge orders shown in the insets. The magnetic charges in (d) and (f) are reversed (positive to negative and vice versa) compared with those in (c) and (e), respectively.[7]

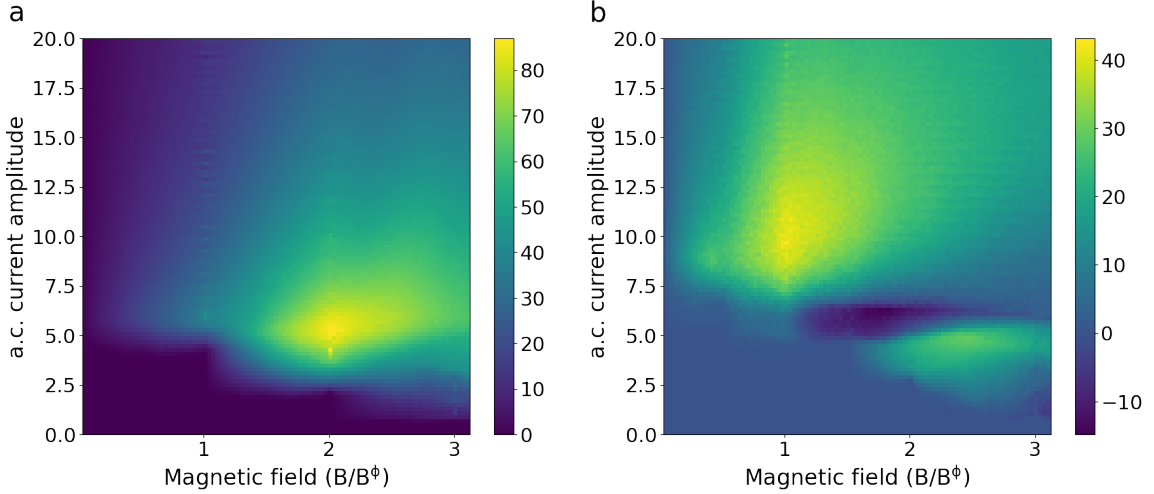


Figure 4.7. Simulated color maps of the d.c. voltage response as a function of the a.c. current amplitude and magnetic field under the type II (a) and III (b) configurations.

not the other one in one complete a.c. cycle, which causes the ratchet motion and corresponds to the bright pattern in Fig. 4.8(a). If we keep increasing the a.c. current amplitude, the ratchet effect disappears because the vortices now have the ability to jump out of the potential wells on both sides (Fig. 4.8(d)). The next "finger" corresponds to vortices moving two potential wells on one side and one potential well on the other side. This mechanism continues as the rest of "fingers" shown in Fig. 4.8(a).

Since we are dealing with BSCCO, a high temperature superconductor. We also want to see how thermal fluctuations can affect the ratchet effect. In Fig. 4.9, we show the d.c. voltage response as a function of the a.c. current amplitude and period under different effective temperatures. Remember from the last section, the system is in liquid state when $T > 2.4$. So Fig. 4.9(b)-(d) are all in the liquid state. We can see that the patterns get more blurry with increasing effective temperature. This is expected because higher thermal energy means higher thermal fluctuation on the

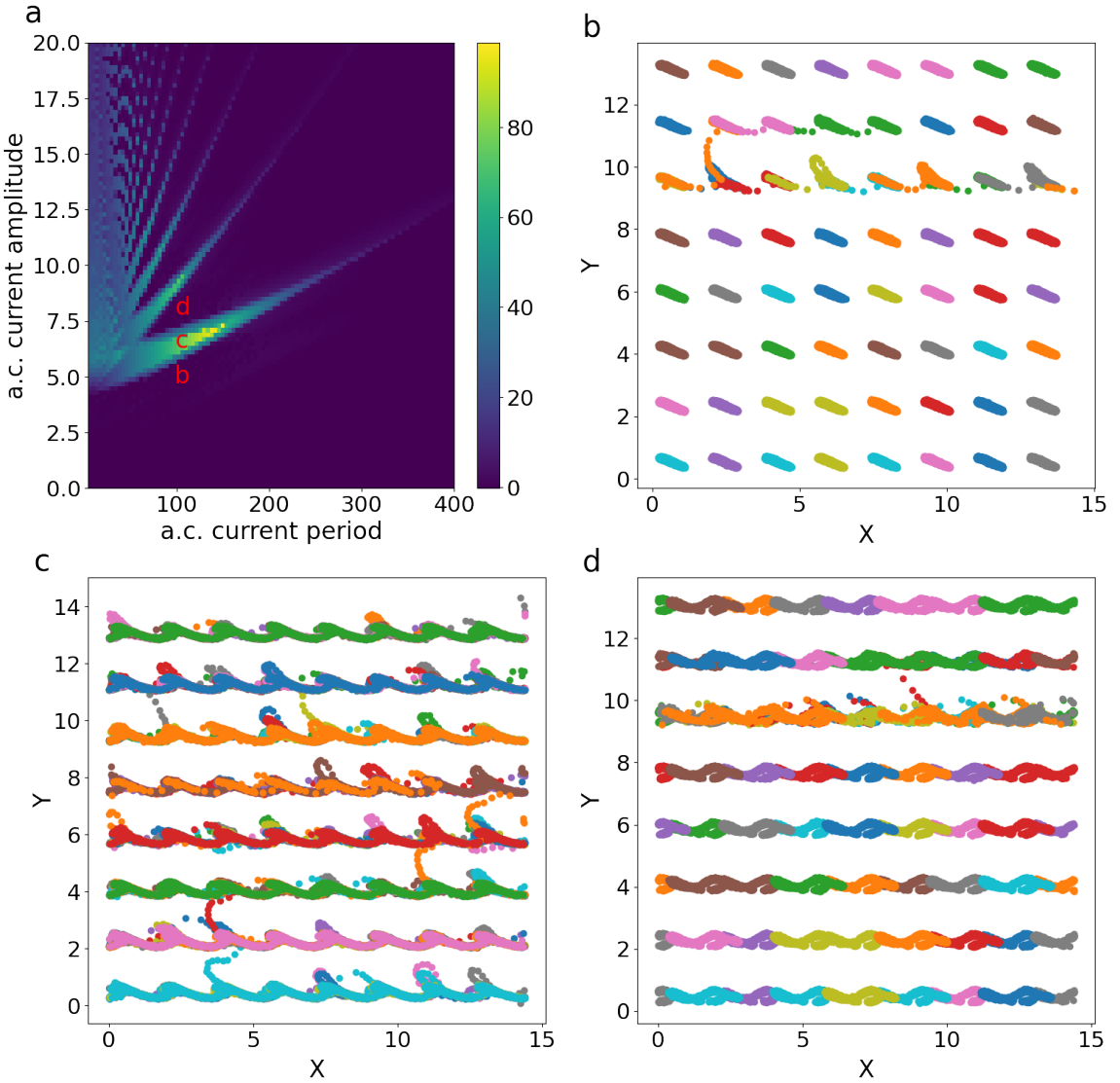


Figure 4.8. (a) Simulated color map of the d.c. voltage response as a function of the a.c. current amplitude and period under effective temperature of 1.0. (b)-(d), vortex trajectories corresponding to "b"- "d" labelled in a. For every a.c. period, (b) shows vortices being trapped in each plaquette, (c) shows vortices only jumping out of one side of the plaquette causing ratchet motion and (d) shows vortices jumping out of both sides of the plaquette. Different colors represent the trajectories of different vortices.

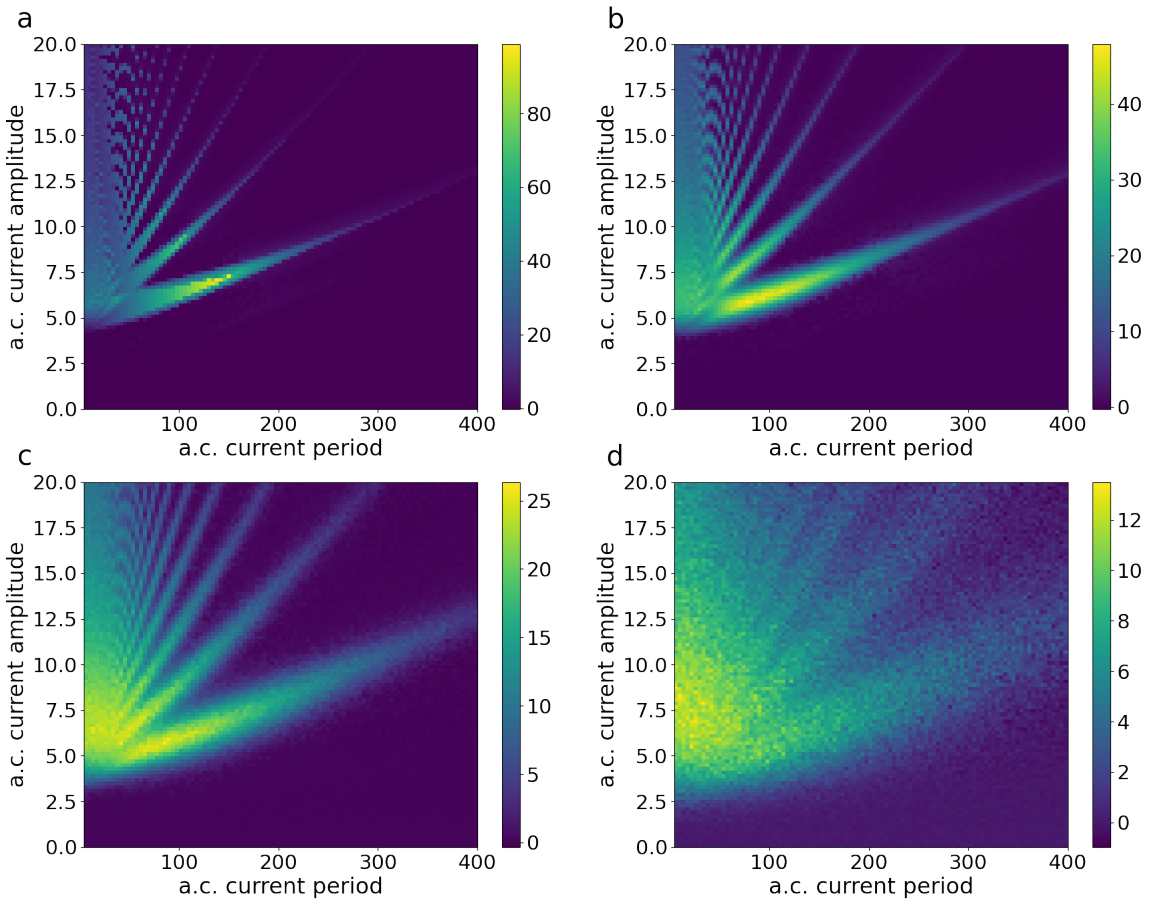


Figure 4.9. Simulated color maps of the d.c. voltage response as a function of the a.c. current amplitude and period under effective temperatures of 1.0 (a), 3.0 (b), 6.0(c) and 10.0(d). The pattern gets more blurry as the effective temperature increases.

vortices so that the magnetic charges cannot pin the vortices as efficient as in low temperature. Also as indicated in the color bars, the d.c. voltage magnitude also drops as we increase the effective temperature.

4.4 Summary

In this chapter, we explore the basic idea of the artificial spin ice superconductor heterosystem. We show that with our simulation method, we are able to include the high thermal fluctuations into the system and simulate the vortex liquid states. The simulation provides a strong supporting evidence that the superconducting vortex flow in liquid state indeed can be controlled by different magnetic potential energy landscapes induced by the artificial spin ice nanoscale bar magnets. We also simulate the d.c. voltage response from the hybrid system with a.c. current source and obtain a good match between the experiment and simulation. We predict that the ratchet effect phase diagram has finger-like structures due to the asymmetric motion of the vortices and explore the ratchet effect under different effective temperatures. The prediction can be further verified by the experiments in the future.

CHAPTER 5

POTENTIAL ENERGY LANDSCAPE NETWORKS OF CONFINED VORTEX MATTER

5.1 Overview

When Dr. Abrikosov predicted the existence of superconducting vortices[8], or Abrikosov vortices, he also predicted the shape of vortex lattice to be square lattice. Though later experiments and theory calculation showed that in the bulk limit, forming triangular lattice costs less energy in the majority of type-II superconductors, and hence more stable[2, 8, 99]. In Fig. 5.1, we showed an image captured by scanning tunneling microscopy (STM) on NbSe₂[8]. Due to the repulsive vortex-vortex interaction, we can see that in the bulk limit, vortices form a triangular lattice.

However, recent development on nanoscale patterning of superconducting films and submicron sized superconducting single crystals enables the experiments on Abrikosov vortex matter under extreme confinement[9, 10, 100–103]. Experiments have shown that in different shapes of mesoscope superconducting samples, the distributions of vortex matter differ from the triangular lattice in the bulk limit. Due to the extreme confinement from the potential walls, the distributions are able to reflect the shapes of the superconducting samples. Recent experiments have also shown that given the competition between the vortex-vortex interaction and vortex-potential-wall interaction, the numbers of vortices play an important role in the system stability, causing some configurations to be more stable than others[9–11]. The numbers of vortices that give higher stability to the system are called the "magic numbers".

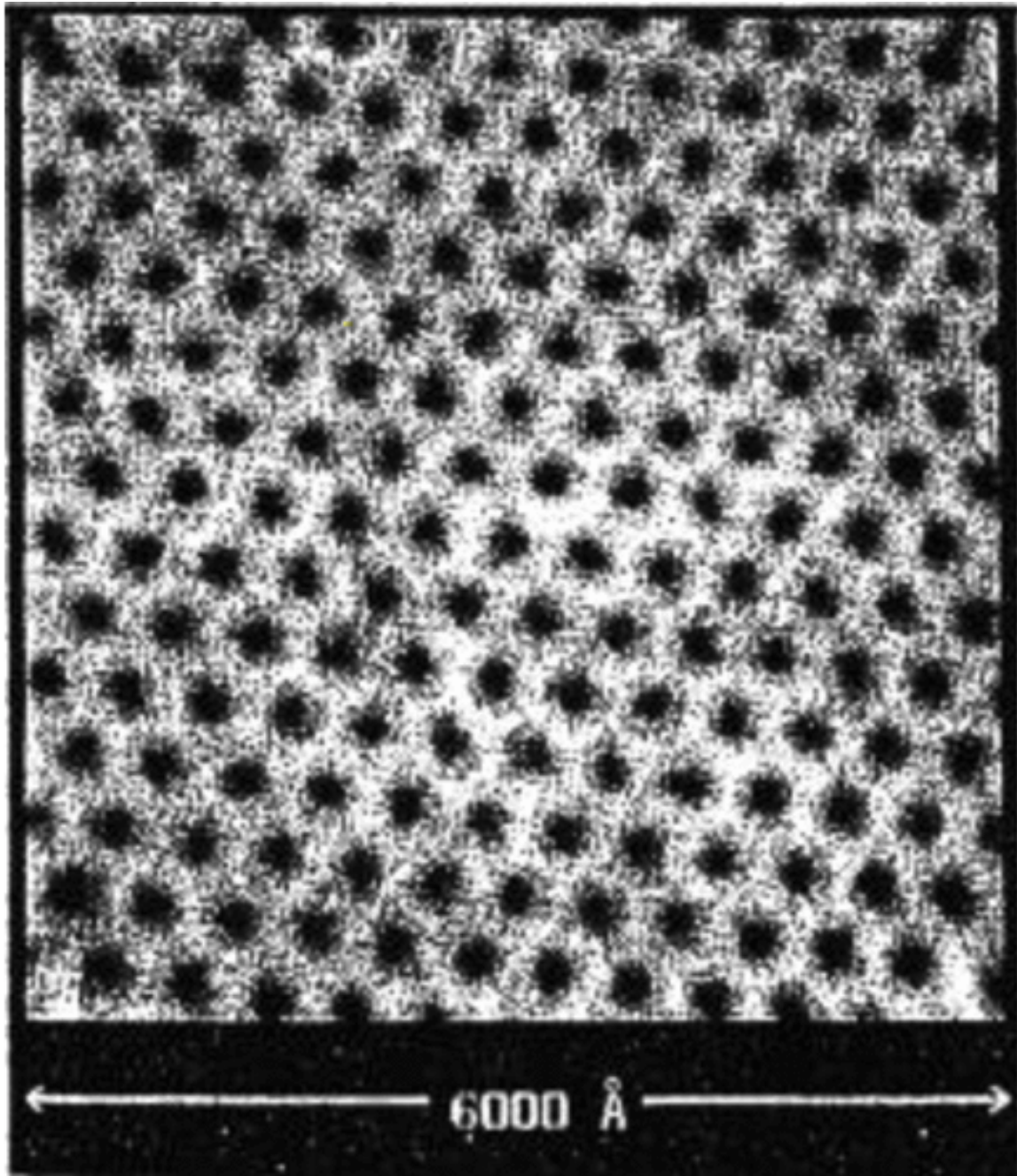


Figure 5.1. Vortices in NbSe₂ defined by scanning tunneling microscopy (STM). [8]

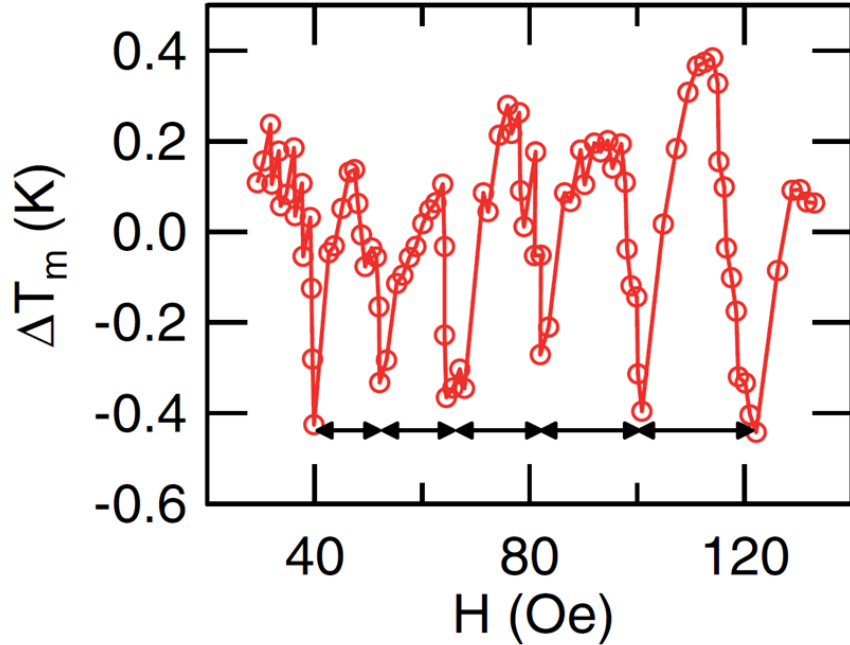


Figure 5.2. Experimental measure of melting temperature of vortices confined in mesoscopic square container. [9]

However, a systematic study on magic numbers has not been developed. In Fig. 5.2, we show the experimental measurement of the melting temperature of vortices confined in mesoscopic square container[9]. We can see the oscillatory behavior clearly in melting temperature as a function of vortex number.

In the past decades, the numerical studies on Abrikosov vortices mostly focused on the vortex pinning and motion with molecular dynamics (MD) simulations[84, 97, 98], or formation of vortices with solving Ginzburg-Landau equations[27, 104–106]. In this chapter, we present a systematic study on the potential energy landscape (PEL)[107, 108] of mesoscopic confined vortex matter with the science network approach. This novel method benefits from the fast development of large computing systems and the availability of such systems at Notre Dame. For this project, all the simulations together cost more than 5 million CPU-hours. Technical details about

large computing at Notre Dame will be presented in the next Chapter.

A potential energy landscape is a high-dimensional surface that describes the dependence of the potential energy as a function of the positions of the elements, such as atoms or molecules[109, 110]. If the system has N classical particles in 3D space, the potential energy of the system is a function of $3N$ variables. It is very hard to visualize such high dimensional surfaces and study the complex systems. However, as first brought up by Stillinger and Weber[108], such complicated surface can be mapped onto a complex network, if we take the metastable states (local minima) as vertices and the transition states connecting the metastable states as edges to form the complex network. This complex network has the graph properties that can be used to described the dynamics of the system. This method has been widely used to study atomic clusters such as Lennard-Jones particles[111] and water clusters[112].

With this novel approach, we show that the potential energy landscape of confined vortex matter can be mapped onto a network, with local minima being vertices and transition states being edges. We show that in the vast majority of cases, the ground state of the system belongs to the sub-network with the highest number of connections and the emergence of magic number configurations is directly connected to a decrease in network complexity. Furthermore, we show the dependence between magic number sequence and superconducting container symmetry and sample size.

5.2 Method

We start the simulation with random configurations on the simulated superconducting sample. In Fig. 5.3, we show the potential energy landscape of a square container with eight superconducting vortices. Within the London approximation[1], Abrikosov vortices can be described as classical interacting particles. The interaction energy between vortices is $E_{ij}^{vv} = E_0 K_0(r_{ij}/\lambda)$, where K_0 is the modified Bessel function of the second kind, $r_{ij} = |\mathbf{r}_i - \mathbf{r}_j|$, and r_i and r_j are the position of vortex i

and j respectively. $E_0 = \phi_0^2/(2\pi\mu_0\lambda^2)$ where $\phi_0 = h/2e$ is the flux quantum. In this simulation, E_0 is taken as 1, so that all other interactions are measured in units of E_0 .

To simulate the extreme confinement condition, we consider polygon containers with hard walls, and phenomenologically take the interaction energy between vortex and a container edge as $E^{vc} = \sum_i 1/d_i$, where d is the distance between a vortex and a container edge. The distribution of vortices is an outcome of competition between vortex-vortex interaction and vortex-potential-wall interaction. To find the local minima and transition states, we adopt a function minimization method called eigenvector following[113, 114], which is a variation of Newton-Raphson method. The details of these two methods are described below.

5.2.1 Newton-Raphson Method

With Newton-Raphson method, for a system with energy $E(\vec{X})$, we can expand the system energy at current configuration:

$$E(\vec{X} + \vec{h}) = E(\vec{X}) + \vec{g}(\vec{X})^T \vec{h} + \frac{1}{2} \vec{h}^T H(\vec{X}) \vec{h} \quad (5.1)$$

With $dE(\vec{X} + \vec{h})/d\vec{h} = 0$, we have

$$H\vec{h} = -\vec{g} \quad (5.2)$$

thus

$$\vec{h} = -H^{-1}\vec{g} \quad (5.3)$$

We diagonalize Hessian matrix H . The orthonormalized eigenvectors are \vec{v}_i with eigenvalue b_i

$$H\vec{v}_i = b_i\vec{v}_i \quad (5.4)$$

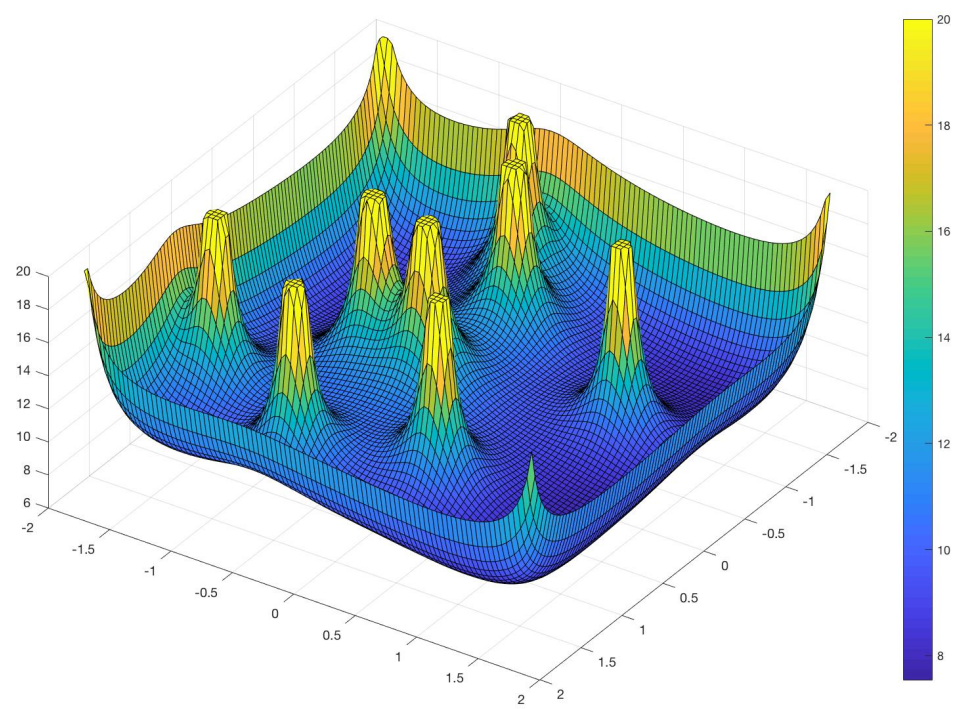


Figure 5.3. Potential energy landscape of a square superconducting sample with eight vortices.

$$\vec{v}_i \cdot \vec{v}_j = \delta_{ij} \quad (5.5)$$

Take it back into (5.2)

$$H \sum_{\alpha} h_{\alpha} \vec{v}_{\alpha} = - \sum_{\alpha} g_{\alpha} \vec{v}_{\alpha} \quad (5.6)$$

Thus

$$h_{\alpha} = -g_{\alpha}/b_{\alpha} \quad (5.7)$$

Take it back into (5.1), and calculate the energy change

$$\begin{aligned} \Delta E &= E(\vec{X} + \vec{h}) - E(\vec{X}) \\ &= \vec{g}(\vec{X})^T \vec{h} + \frac{1}{2} \vec{h}^T H(\vec{X}) \vec{h} \\ &= \sum_{\alpha} g_{\alpha} h_{\alpha} + \frac{1}{2} b_{\alpha} h_{\alpha}^2 \\ &= \sum_{\alpha} -\frac{g_{\alpha}^2}{2b_{\alpha}} \end{aligned} \quad (5.8)$$

So we find that if $b_{\alpha} > 0$ then Newton-Raphson method leads to $\Delta E < 0$, thus this process minimizes the system energy. Since $dE/d\vec{h} = 0$ leads the state to a local minimum, maximum or saddle point, and $b_{\alpha} > 0$ for every α that minimizes the energy, this will lead to the local minimum. But this is actually a very strong condition to preserve in the whole process, it's hard for application.

5.2.2 Eigenvector Following

We turn to a modified version of Newton-Raphson method, which is called eigenvector following method. We can modify this problem to an optimization problem under some constraints

$$|h_i| = c_i \quad (5.9)$$

Which imposes separate restrictions on the step size for each Hessian eigendirection.

With Lagrange multipliers μ_i for each this constraint

$$\begin{aligned} E(\vec{X} + \vec{h}) &\rightarrow E(\vec{X} + \vec{h}) - \sum_{\alpha} \frac{1}{2} \mu_{\alpha} (h_{\alpha}^2 - c_{\alpha}^2) \\ &= E(\vec{X}) + \sum_{\alpha} g_{\alpha} h_{\alpha} + \frac{1}{2} b_{\alpha} h_{\alpha}^2 - \frac{1}{2} \mu_{\alpha} (h_{\alpha}^2 - c_{\alpha}^2) \end{aligned} \quad (5.10)$$

With $dE/d\vec{h} = 0$

$$h_{\alpha} = \frac{g_{\alpha}}{\mu_{\alpha} - b_{\alpha}} \quad (5.11)$$

$$\begin{aligned} \Delta E &= \sum_{\alpha} g_{\alpha} h_{\alpha} + \frac{1}{2} b_{\alpha} h_{\alpha}^2 \\ &= \sum_{\alpha} (\mu_{\alpha} - b_{\alpha}/2) g_{\alpha}^2 / (\mu_{\alpha} - b_{\alpha})^2 \end{aligned} \quad (5.12)$$

Then, we can choose

$$\mu_{\alpha} = b_{\alpha} \pm \frac{1}{2} |b_{\alpha}| (1 + \sqrt{1 + 4g_{\alpha}^2/b_{\alpha}^2}) \quad (5.13)$$

With "+" for $\Delta E > 0$ (maximization), and "-" for $\Delta E < 0$ (minimization). According to (5.11), this gives steps

$$h_{\alpha} = \frac{\pm 2g_{\alpha}}{|b_{\alpha}| (1 + \sqrt{1 + 4g_{\alpha}^2/b_{\alpha}^2})} \quad (5.14)$$

Thus, we can search for local minimum/maximum without constraint from sign of eigenvalues of Hessian matrix. Besides, this method can also be used for transition state search, which we define as first-order saddle point.

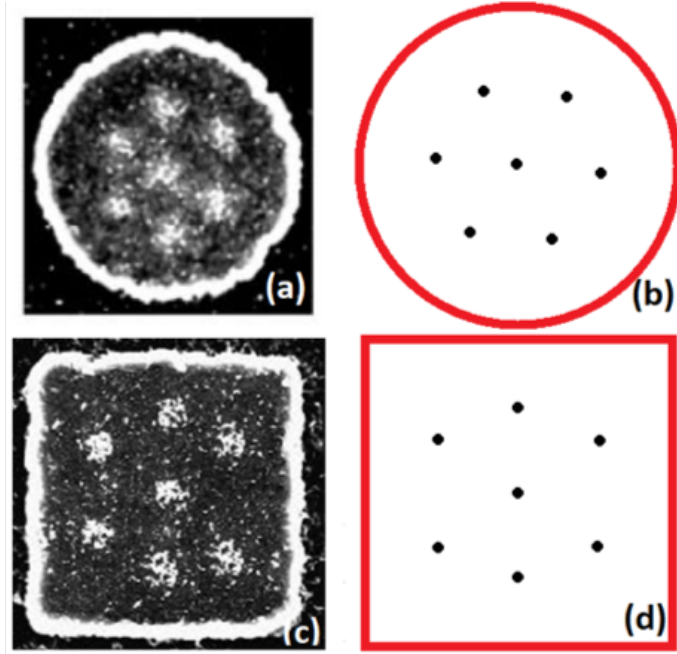


Figure 5.4. Experimental results of 7 vortices confined circular(a) and square(c)[10] containers. The corresponding simulation results are shown in (b) and (d).

5.3 Results and Discussion

5.3.1 Local Minima

In Fig. 5.4, we show the comparison between the experimental imagining[10] and our simulation on the ground states of confined 7 vortices in circular and square mesoscopic containers. We can see that with the computation methods mentioned above, we are able to obtain a good match between the experiments and simulations.

We also apply the algorithms on triangular containers, as shown in Fig. 5.5, and compare them with experiments. On the top of Fig. 5.5, we show the experimental images taken by scanning SQUID[11] from a research group in Japan and our simulation results are shown in the bottom of Fig. 5.5. By comparing the experiments and simulations, we can see that they both reflect the geometry of the containers and

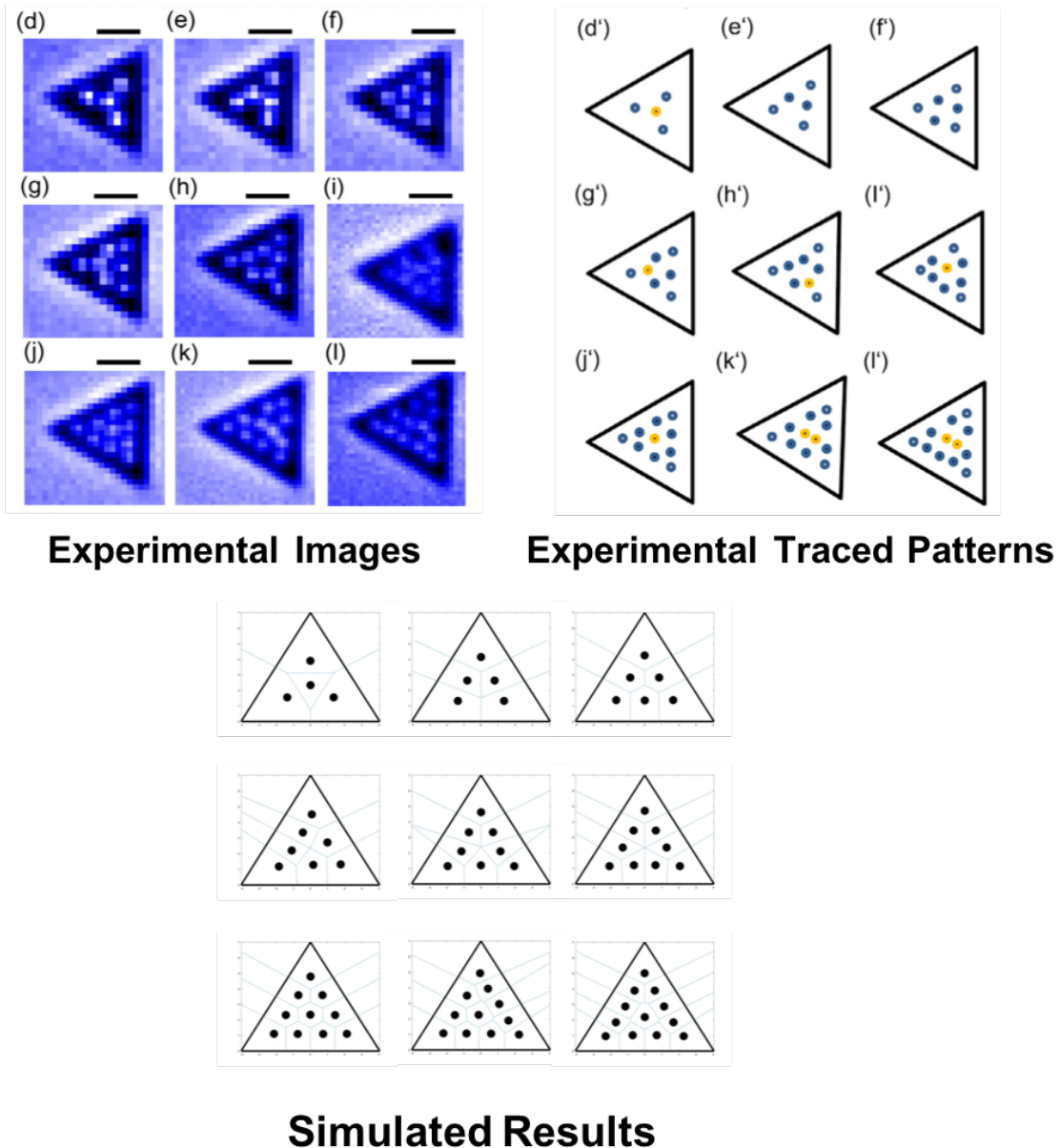


Figure 5.5. Top: Images taken with scanning SQUID on mesoscopic triangular containers with increasing vortices[11]. Bottom: Simulation results generated from our simulation.

have a good agreement.

5.3.2 Network Representation

An example of the network representation for confined vortex matter is shown in Fig. 5.6. Here we consider 47 vortices confined in a square container with hard confinement walls, which means that the interaction between vortex and container diverges at the boundary. In Fig. 5.6(a), we show the network representation of such system. Each node in the network represents a local minimum state and each edge represents the transition state that connects the two adjacent local minima. The nodes with larger size correspond to the states with lower energy and the large nodes form hubs of the whole network.

As illustrated in Fig. 5.6(b), in order for the system to travel from one local minimum to another one, there is an energy barrier to cross. And the minimum amount of energy for the barrier corresponds to a transition state. Fig. 5.6(c) shows different configurations in the square container with two configurations being the local minima and one being the transition state that connects them. Though it's hard to distinguish these configurations with human eyes, they correspond to very different energy states in the system.

5.3.3 K-Core Decomposition

In graph theory, the k -core of a graph is the largest subgraph where each vertex has at least k interconnections. This degeneracy measure can characterize the sparseness of the graphs.[115] The k -core of a graph can be found by repeatedly removing the vertices with degree less than k , as well as the edges associated with these vertices. In Fig. 5.7(a) and (b), we show the k -core decomposition on the potential energy landscape network of systems with 50 superconducting vortices on square and triangular containers. As highlighted with red circles, for these two cases the ground

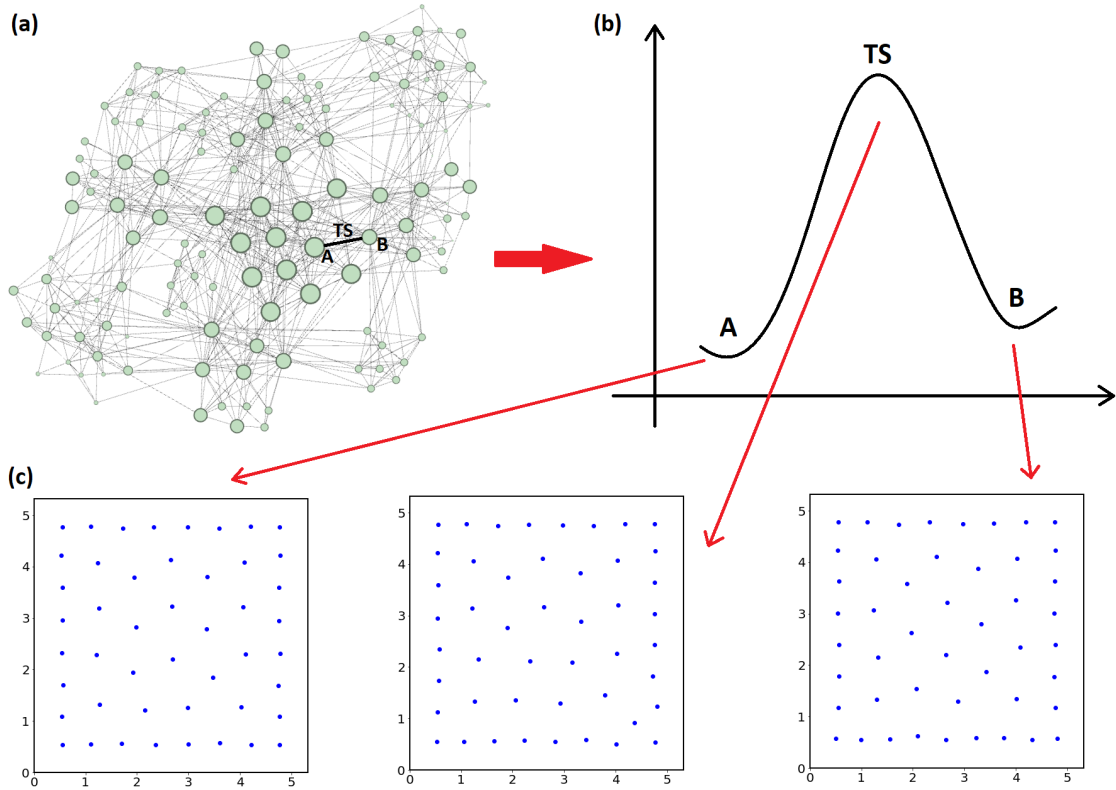


Figure 5.6. Network representation and its relation to real space configurations. (a) Network representation of the potential energy landscape (PEL) of 47 vortices in a square container. Each vertex corresponds to a metastable state, and those with larger sizes are of lower energy. An edge between 2 vertices means that there is at least 1 transition state connecting the 2 metastable states represented by the 2 vertices. (b) Energy change along a transition path from state A to state B through transition state TS, overcoming an energy barrier. (c) Real space configurations correspond to the metastable states and transition state along the transition path in (b).

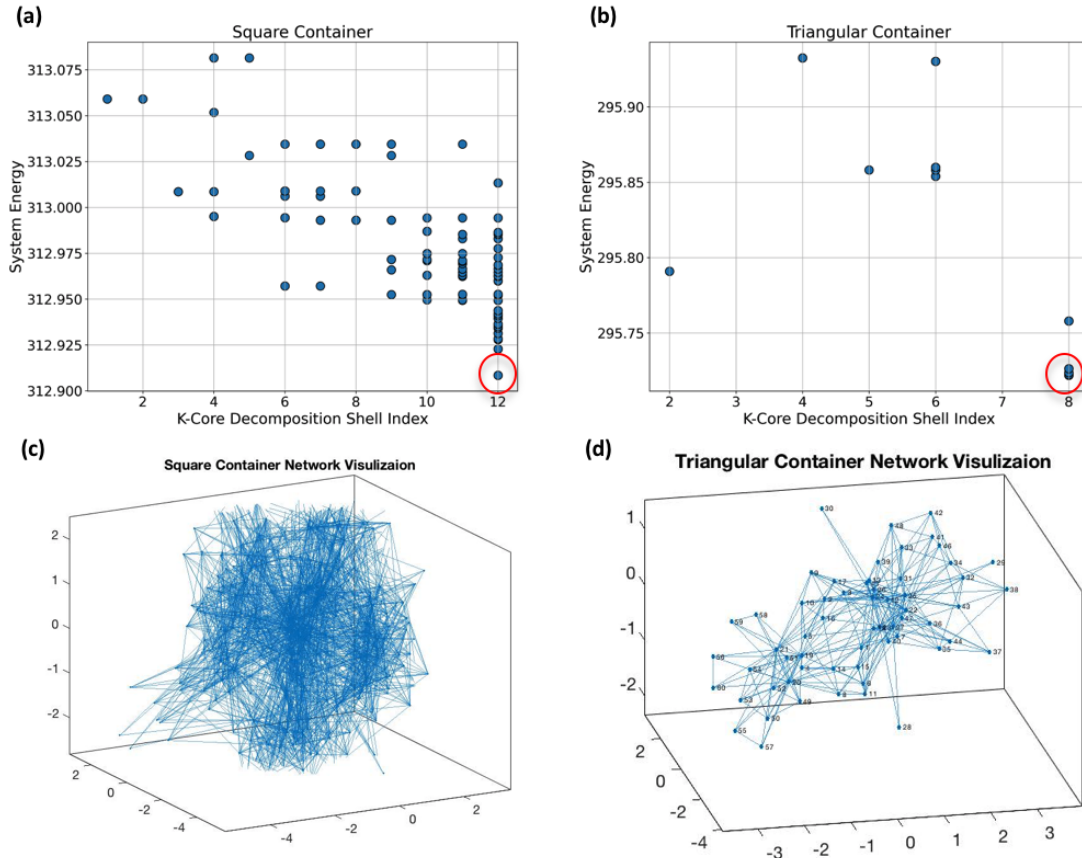


Figure 5.7. Energy of states in different k-core decomposition shells with 50 superconducting vortices for (a) square container (b) triangular container.

The corresponding potential energy landscape network representation is shown in (c) and (d). The size of each container is $25\lambda^2$. The ground state is always in the shell with the largest k-core decomposition shell index as highlighted with red circles.

states belong to the largest coreness shells. We also find that this conclusion is valid for many other systems, including different numbers of vortices in different containers and also clusters formed by Lennard-Jones particles[111].

In Fig. 5.7(c) and (d), we show the network representations corresponding to systems in (a) and (b). We can see that the networks show certain clustering patterns and also with this network approach, we are able to relate the energetic properties of the system with the topology of the potential energy landscape. The k-core decomposition process can be visualized as peeling the network layer by layer and approach the interior. The innermost core of the network is the hub connecting the dynamics of the system. This is similar to the role of the ground state, as all excited states are inclined to decay to the ground state.

5.3.4 Network Complexity

To obtain more information about the potential energy landscape network of the confined vortex matter, we calculated the complexity of the networks with varying numbers of superconducting vortices in triangular and square containers. The network complexity is measured via the vertex degree magnitude-based information content, $I_{av} = -\sum_{i=1}^N (a_i/A) \log_2 (a_i/A)$ [116, 117], where a_i is the degree of vertex i in the network, and $A = \sum_{i=1}^N a_i$ is the graph total adjacency[118]. This is an extension of the Shannon information-theoretic approach to the description of chemical structures[119][116].

As shown in Fig. 5.8(a), generally speaking, the network complexity increases as the number of vortices in the system increases. In addition to the general trend of increasing complexity with more vortices, we can see that the complexity drops to a very low level at some vortex numbers. These are the states where the vortex numbers match the geometry of the containers, as shown in Fig. 5.8(b)-(f). As a result, these systems have less meta stable states and exhibit lower network complexity since

less meta stable states means it's less likely for excitation, which corresponds to higher melting temperature, and the so-call magic number configurations. Similar experimental results have been reported from other research groups[9], showing that the states preserving the containers symmetries tend to be more stable. Though there are exceptions, for example when $N = 15$ in triangular container, the system should be stable but the network complexity does not indicate a drop. But it is still worth noting that with the network approach, we are able to obtain different potential energy landscape networks for different geometric containers and shed light on the magic-number problems.

5.3.5 Melting Temperature

For each ground state configuration in triangular container with varying vortex numbers and container sizes, a melting process with molecular dynamics simulation is conducted to extract the melting temperature. As shown in Fig. 5.9(a), for vortex numbers preserving the symmetry of the container (Fig. 5.9(c)-(g)), they show a relatively high melting temperature, corresponding to a relatively high stability. In triangular container, these are the states with triangular numbers of vortices, where $N = 6, 10, 15, 21$, etc.

As the container gets smaller, the vortices are squeezed more by the container confinement. As a result, the configuration symmetry gets destroyed, as shown in Fig. 5.9(h) and (i). We can also notice the corresponding stability drop as indicated by the red arrows in Fig. 5.9(b). In Fig. 5.9(j)-(l), we show the vortex configurations where the systems also indicate higher stability. These are the states that preserve the three-fold symmetry in the triangular container even without the perfect triangular numbers of vortices.

Some of these stable states can also be found in Fig. 5.8(a), corresponding to the significant drop in the network complexity. These are the “magic number” states of

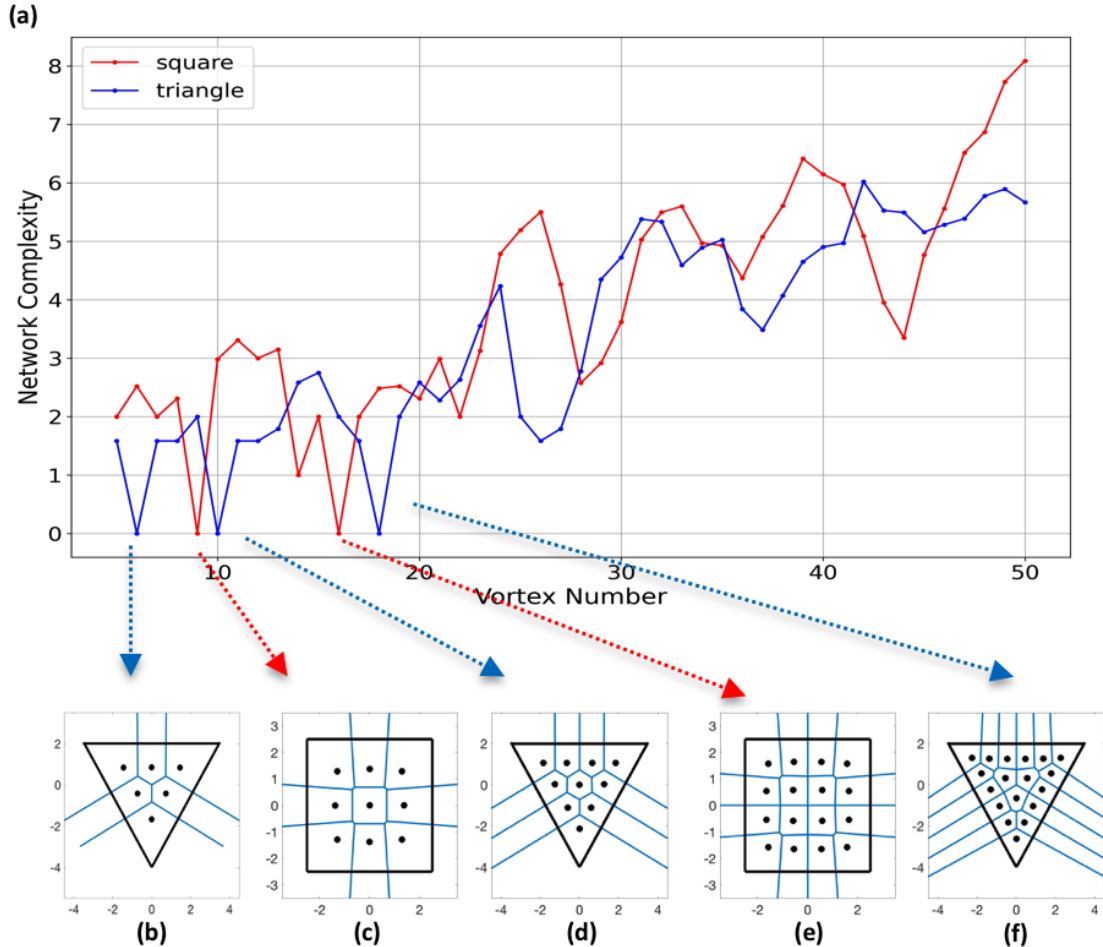


Figure 5.8. (a) Normalized network complexity for the potential energy landscape in square and triangular containers with varying vortex numbers.
 (b)-(f) Vortex configurations in square and triangular containers corresponding to the network complexity dips in (a).

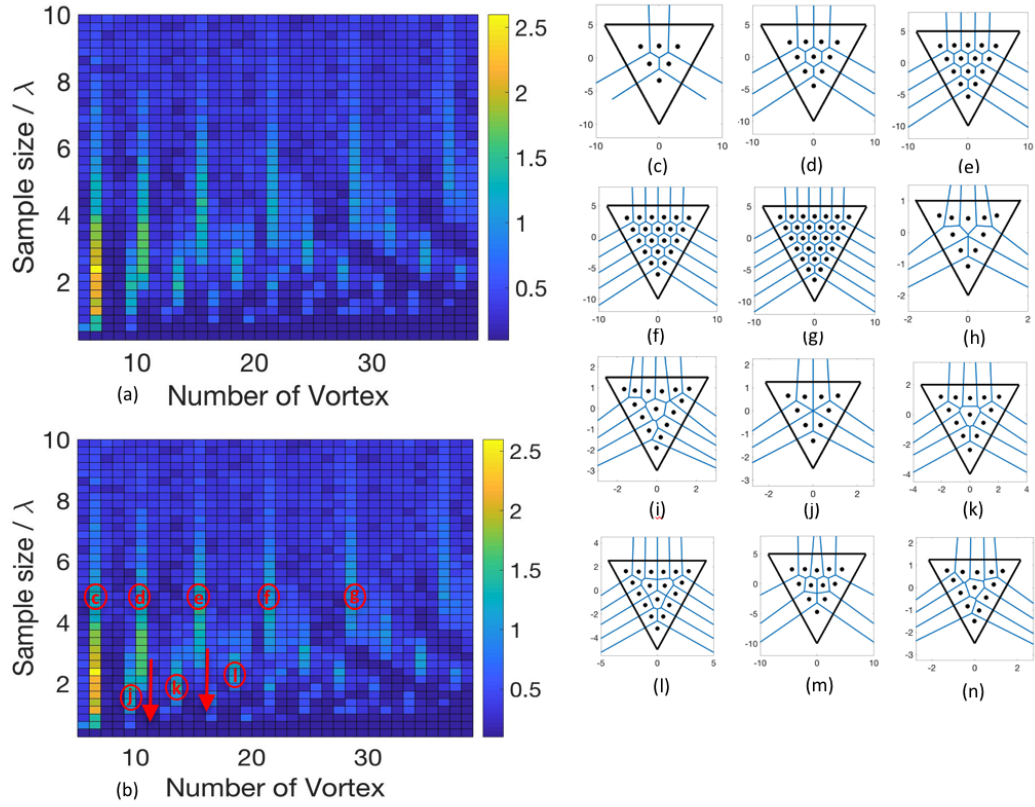


Figure 5.9. (a) Melting temperatures in triangular containers corresponding to varying vortex numbers and sample sizes. (c) – (g) Vortex configurations corresponding to the data points (c) – (g) in (b). These states have higher stability due to the perfect symmetry between vortex numbers and container geometry. In triangular containers, when the numbers of vortex are the triangular numbers: 6, 10, 15, 21, 28, etc., the containers can be perfectly filled, which leads to higher stability. Panels (h) and (i) show the transition from (d) and (e) as labelled by arrows in (b). As the containers get smaller, the vortices are squeezed by the container walls such that the perfect symmetry is destroyed. This is the size effect that we mention in our main text and can result in the decrease of stability. (j) – (l) Vortex configurations corresponding to the data points (j) - (l) in (b). These states preserve the three-fold symmetry of the system. They also show higher stability than the states with two-fold symmetry ((h), (i), (m)) and the states with no mirror symmetry ((n)). (m) – (n) Random unstable states.

the system, and can be decomposed into layers of vortices with certain symmetry. For example, for the “magic number” states in a triangular container, each layer of vortices should preserve the three-fold symmetry, and thus the “magic number” should be a combination of 1, 3, 6... 3n.

The combination of such “magic shell numbers” is non-trivial and depends on the container size, as a result of competition between vortex-vortex interaction and vortex-container interaction. In the phase diagram of system stability in terms of vortex number and container size as shown in Fig. 5.9(a), we can clearly see the persistence of “magic number” over some range of parameters, as well as its shift when the system size changes gradually. Interestingly, for some ground state configurations with relatively high stability but do not preserve container symmetry, in the melting process, the layer with different symmetry from the container will rotate first, thus drive the system into a “dynamic symmetry-preserving” state.

5.4 Summary

In this chapter, we present a network science approach to tackle the ”magic number” problems in the confined vortex matter. We compare the stable states from our simulation models in different geometric containers to the ones observed in experiments, including circular, triangular and square containers. In all cases, our simulation has a good agreement with the experiments. By taking the metastable states as vertices and transition states as edges, we construct the complex networks for the potential energy landscape in confined vortex matter. The complex network has the graph properties to describe the dynamics of the system. We find that in the majority cases, the ground state of the system belongs to the sub-network with the highest number of connections and the complexity of the potential energy landscape network is highly correlated to the stability of the system, which directly leads to the emergence of magic number sequence. By the large scale molecular dynamics

simulation on the triangular container, we show the correlation between the system stability and the container symmetry and sample size. Although we focus on the superconducting vortices in this chapter, this approach can also be easily generalized to other many-particle systems.

CHAPTER 6

CONCLUSION AND FUTURE WORK

In this thesis, we investigate the pinning and vortex dynamics in different systems. We first show that in moiré pinning patterns, easy quasi-one-dimensional channels develop along the edges of the superlattice causing the dips in the critical current profile and transverse movements at the commensurate angles. As we change the twist angle in moiré patterns, the vortex dynamics can range from easy quasi-one-dimensional channels to suppression of vortex movement. This project can be further verified in follow-up experiments by placing two superconducting thin films such as MoGe with triangular pinning lattice on top of each other, and measure the electric properties of the system while varying the twist angle. Our simulation study provides a numerical basis for a novel approach in controlling the vortex dynamics in correlated systems.

We also study the vortex configurations and dynamics in superconducting vortex system interacting with Santa Fe array pinning. Our simulation results suggest that due to the frustrated pinning potential, there is no matching effect in the Santa Fe array and some vertices at the half matching field occupy excited states instead of the low energy states. Also since the transverse vortex flow develops in Santa Fe array, it can provide better pinning effect compared to the square lattice. It would be interesting to see experiments on direct comparison between the Santa Fe pinning array and square lattice. Because of the better pinning effect, the Santa Fe pinning array is potentially important in designing superconducting devices.

In the artificial spin ice project, we provide numerical evidence for the experiments

showing that vortex dynamics in high temperature regime (vortex liquid) is indeed controllable via switching between different artificial spin ice configurations. We also study the vortex ratchet effect in such systems and show that the phase diagram has finger-like structures. Follow-up projects can include experimental verification on the finger-like structures. This diode behavior in vortex dynamics could potentially provide the basis for computing logic gates. On the other hand, we only study three types of charge configurations. It would also be interesting to explore other types of configurations with our simulation model as well.

For the confined vortex matter project, we present a novel approach based on the network science to understand the underlying potential energy landscapes of the systems. We show that by taking the metastable states as vertices and transition states as edges, the constructed network has the topological properties to describe the dynamics of the system. In the majority cases, the ground state of the system belongs to the sub-network with the highest number of connections and the complexity of the network is highly correlated to the system stability. This network approach not only applies in vortex systems, it can be generalized to other interacting particle systems. However, in order to map out the entire potential energy landscapes, this approach consumes extensive computing power. Due to the computing limit, we perform the simulations with limited numerical precision. Future projects can include designing faster algorithms with higher numerical precision. Also with more computing power, we can study larger systems and include defects in the containers to construct more complex networks.

APPENDIX A

LARGE SCALE COMPUTING AT NOTRE DAME

A.1 Overview

In the previous chapters, we show a lot of simulation results on superconducting vortex dynamics. Some of the results are extremely expensive in terms of CPU-hours. For example, Fig. 5.9 can take up to 100,000 CPU-hours. If we used a normal 12-core machine to generate the data, it would take 347 days(almost a year!) to finish. But imagine if with 1000 cores, this can be done in less than a week. Luckily at Notre Dame, we have a high performance distributed computing system with roughly 15,000 computing cores. This is a very powerful computing system and can be very useful for any simulation related research groups. As shown in Fig. A.1, only in the year of 2020, we have used more than 8,000,000 CPU-hours for our simulation works¹.

However, using this computing pool is non-trivial and requires some computing techniques. In order for the following students to pick up the large scale computing method, so in this chapter, we focus on introducing some key concepts to the computing pool at Notre Dame and showcase how we incorporate these computing techniques with our research.

¹According to <https://resources.rescale.com/the-real-cost-of-high-performance-computing/>, the cost of one CPU-hour is roughly 10 cent and this computing facility is complete free to anyone at Notre Dame.

Top Condor Users for the Last Year				
	CPU Hours	Percent Total	Max Jobs Running	Max Jobs Queued
wli12@nd.edu	8255867	35.89%	6895	22300
mzhu4@nd.edu	5030304	21.87%	7954	110637
rbucci@nd.edu	1636817	7.12%	1721	5262
abegmoha@nd.edu	1348582	5.86%	6000	43293
xmeng@nd.edu	984148	4.28%	5984	20005
jhuber3@nd.edu	854009	3.71%	5993	60794
gkeller1@nd.edu	828468	3.60%	5880	15344
kmukherj@nd.edu	783911	3.41%	2408	19398
dmitche6@nd.edu	674816	2.93%	5940	19680
pamorimv@nd.edu	632899	2.75%	5787	99975
scavany@nd.edu	503797	2.19%	6000	8980
jherri1@nd.edu	351650	1.53%	3753	25068
ocracchi@nd.edu	175932	0.76%	1197	119765
kgao@nd.edu	162214	0.71%	5699	43954

Figure A.1. Top Condor users in the year of 2020 at University of Notre Dame.

A.2 Condor

Condor is a distributed batch computing system developed by University of Wisconsin–Madison in 1988. It has been widely used since then at many institutions around the world, including Notre Dame. Condor allows users to share their computing resources and is good at harnessing idle machines. The core idea of Condor is that we put all the computing resources on campus together, when the owners of the machines are not using them, other users can take over and harness the free computing power. Since most workstations are idle most of the time, this mechanism can highly increase the computing power availability on campus.

However, Condor protects the interests of the owners as well. Owners can come back to their machines anytime and kick off the current jobs. Because of the possibility of jobs being killed anytime, when using Condor it's better to submit a lot of jobs at the same time and make sure each job won't take too long to finish. Because when the job is killed, everything that has been run on that machine will be lost. Condor cannot guarantee any single job will finish quickly, but it will allow people to accomplish a lot more overall work than only using their machines.

To use Condor at Notre Dame, it's as simple as submitting a Shell script. Please refer to: <http://ccl.cse.nd.edu/operations/condor/using.shtml> for submitting simple Condor jobs at Notre Dame. Condor can be used directly with a Shell script, but it's inconvenient to include any workflow logic, which means all you can do is submit the jobs and wait for them to finish. Therefore using simple Condor script is not the focus of this chapter and we need something more powerful.

A.3 Work Queue

In order to unleash the power of 15,000 computing cores, the Notre Dame Cooperative Computing Lab(CCL) has developed a framework called Work Queue. The

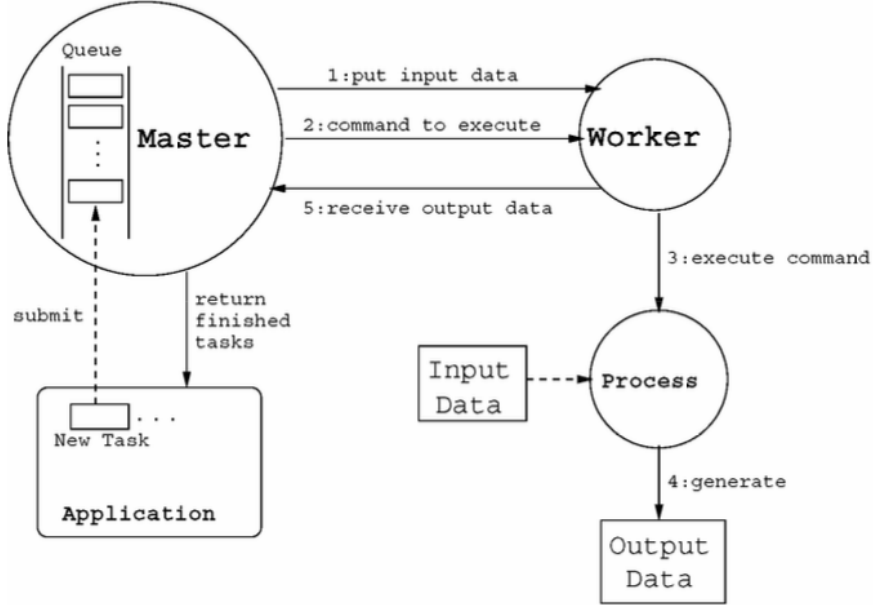


Figure A.2. The general framework of a Work Queue application.

core of this framework is still Condor, but it provides rich APIs for Python and C++ users. Instead of writing a Shell script, with Work Queue, we can pack everything with only Python or C++. So we can integrate complicated workflows with the distributed system.

As shown in Fig. A.2, Work Queue has a master-worker architecture. The master is responsible for creating a task queue and distributing the jobs to the workers. Each worker takes the input data and execution commands from the master and runs the job in the computing pool. One worker can be one core or multiple cores depending on the user's needs. Once the job is finished, the worker will send the output back to the master and the master can decide the next move.

The benefit of this architecture is with Work Queue APIs, everything can be done only using Python or C++. It largely reduces the burden of incorporating Shell commands with the simulation languages. Also because of this, we can design complicated algorithms and workflows with the master based on the outputs received.

We will give an example in the next section on how our simulations benefit from it.

A.4 Example

In this section, we show an example about how we integrate the master-worker architecture with our simulation. As shown in Listing. A.1, this is the Work Queue script that is used to generate Fig. 2.6. There are 3,000 data points in Fig. 2.6(a) and the idea is to perform parallel computing for each data point. In order to accelerate the process of finding the critical currents, binary search is used in the algorithm. Up until line 74, the code demonstrates how we can set up the Work Queue client, split the jobs and queue the jobs to the master. From line 77 to the end, the code shows how to handle outputs from the workers and perform binary search to find the critical currents.

To actually use the script, we need a machine as the host to keep this script running and set up the environment properly for Work Queue. (Refer to https://cctools.readthedocs.io/en/latest/work_queue/ for details.) As soon as the process shuts down, all the workers will stop working. It is ideal to put this process in user's own machine. But if the user doesn't have a machine, it's possible to keep it running on `condorfe` with command `nohup python <your_script> &`.

Once the master is running, the user can submit workers on `condorfe`. (Also refer to the Work Queue guide for details.) If everything is set up properly, the workers will be running the jobs for the master. Note that although there are 15,000 cores in the computing pool, only 6,000 workers are allowed for all the users combined to avoid the file system failure. So it means if we want to use all the computing power, we need to implement multi-threads in the simulations. This can be done in C++ easily. But if the simulation doesn't benefit from multi-threads or the simulation is in Python(Python doesn't support multi-threads), the most computing power the user can get is one core per worker, so 6,000 cores in total.

Here are some other important notes:

- The maximum number of files under one folder in AFS is about 30,000. Depending on the length of the files names, the number can be smaller. So when designing the parallel computing algorithm, we need to make sure the number of files is within the limit.
- If we want to keep the master process alive after logging out the cluster, we need to make sure the process has permission to access the AFS file system.²
- There is a priority ranking in the pool, which means the more CPU-hours one user has used, the lower priority they have.

A.4.1 Sample Code

```
1 from __future__ import division
2 from work_queue import *
3
4 import os
5 import sys
6
7 # Work Queue project port and name
8 port = 0
9 project_name = "bilayer_current"
10
11 # Define simulation related parameters
12 max_n = 1000
13 n_step = 100
14 n_list = []
15 n = 100
16 while n <= max_n:
17     n_list.append(n)
18     n += n_step
19
```

²Refer to <https://douglasduhaime.com/posts/keeping-screens-alive-on-afs/filesystems.html>

```

20 max_angle = 30.0
21 angle_step = 0.1
22 angle_list = []
23 angle = 0.0
24 while angle <= max_angle:
25     angle_list.append(angle)
26     angle += angle_step
27
28 # We use the binary search for finding the critical current
29 precision = 0.01
30 target_velocity = 40.0
31
32 min_current = 0
33 max_current = 50.0
34 mid_current = (min_current + max_current) / 2
35
36 left_current = []
37 right_current = []
38 task_n = []
39
40 # Work Queue setup
41 q = WorkQueue(port)
42 q.specify_master_mode(WORK_QUEUE_MASTER_MODE_CATALOG)
43 q.specify_name(project_name)
44 print "listening on port %d..." % q.port
45
46 # Since we are doing parallel computing, we send each configuration
47 # to each worker.
47 for n in n_list:
48
49     for angle in angle_list:
50

```

```

51     this = (n, angle)

52

53     left_current[this] = min_current
54     right_current[this] = max_current

55

56     # Define the execution commands
57
58     command1 = "source /opt/crc/Modules/current/init/bash\n"
59
60     command2 = "module load python\n"
61
62     command3 = "python current.py {} {} {}".format(n, angle,
63
64         mid_current)
65
66     t = Task(command1 + command2 + command3)

67
68     # Define input files
69
70     infile = 'data.out_n_' + str(n) + '_angle_' + str(angle)
71
72     t.specify_file("current.py", "current.py", WORK_QUEUE_INPUT,
73         cache=False)
74
75     t.specify_file(infile, infile, WORK_QUEUE_INPUT, cache=False
76     )

77     # Define output files
78
79     outfile = 'velocity.out_n_' + str(n) + '_angle_' + str(angle
80     )
81
82     t.specify_file(outfile, outfile, WORK_QUEUE_OUTPUT, cache=
83         False)
84
85
86     # Submit the jobs
87
88     taskid = q.submit(t)
89
90     task_n[taskid] = this
91
92     print "submitted task (id# %d): %s" % (taskid, t.command)
93
94
95     # This while loop is for receiving the outputs and follow-up logic
96
97     while not q.empty():

```

```

78     t = q.wait(10)
79
80     if t:
81
82         print "task (id# %d) complete: %s (return code %d)" % (t.id,
83         t.command, t.return_status)
84
85         # If the job failed
86
87         if t.return_status != 0:
88
89             print t.output
90
91
92     else:
93
94         # Retrieve the job and output
95
96         n, angle = task_n[t.id]
97
98         this = (n, angle)
99
100
101        outfile = 'velocity.out_n_' + str(n) + '_angle_' + str(
102        angle)
103
104        with open(outfile, 'r') as f:
105
106            velocity = float(f.readline())
107
108            os.system('rm {}'.format(outfile))
109
110
111        # Binary search
112
113        mid = (right_current[this] + left_current[this]) / 2
114
115        if velocity > target_velocity:
116
117            right_current[this] = mid
118
119        else:
120
121            left_current[this] = mid
122
123
124        if right_current[this] - left_current[this] < precision:
125
126            with open('current.out_n_' + str(n) + '_angle_' +
127            str(angle), 'w') as f:
128
129                f.write('{}\n'.format(right_current[this]))
130
131        else:
132
133            # Submit new jobs if the search is not finished
134
135            mid = (right_current[this] + left_current[this]) / 2

```

```

107             command1 = "source /opt/crc/Modules/current/init/
108             bash\n"
109
110             command2 = "module load python\n"
111
112             command3 = "python current.py {} {} {}".format(n,
113
114             angle, mid)
115
116
117             t = Task(command1 + command2 + command3)
118
119             t.specify_file("current.py", "current.py",
120
121             WORK_QUEUE_INPUT, cache=False)
122
123
124             infile = 'data.out_n_' + str(n) + '_angle_' + str(
125
126             angle)
127
128             t.specify_file(infile, infile, WORK_QUEUE_INPUT,
129
130             cache=False)
131
132
133             outfile = 'velocity.out_n_' + str(n) + '_angle_' +
134
135             str(angle)
136
137             t.specify_file(outfile, outfile, WORK_QUEUE_OUTPUT,
138
139             cache=False)
140
141             taskid = q.submit(t)
142
143             task_n[taskid] = this
144
145             print "submitted task (id# %d): %s" % (taskid, t.
146
147             command)

```

Listing A.1: Sample code of finding critical current with Work Queue.

APPENDIX B
SUPPLEMENT INFORMATION

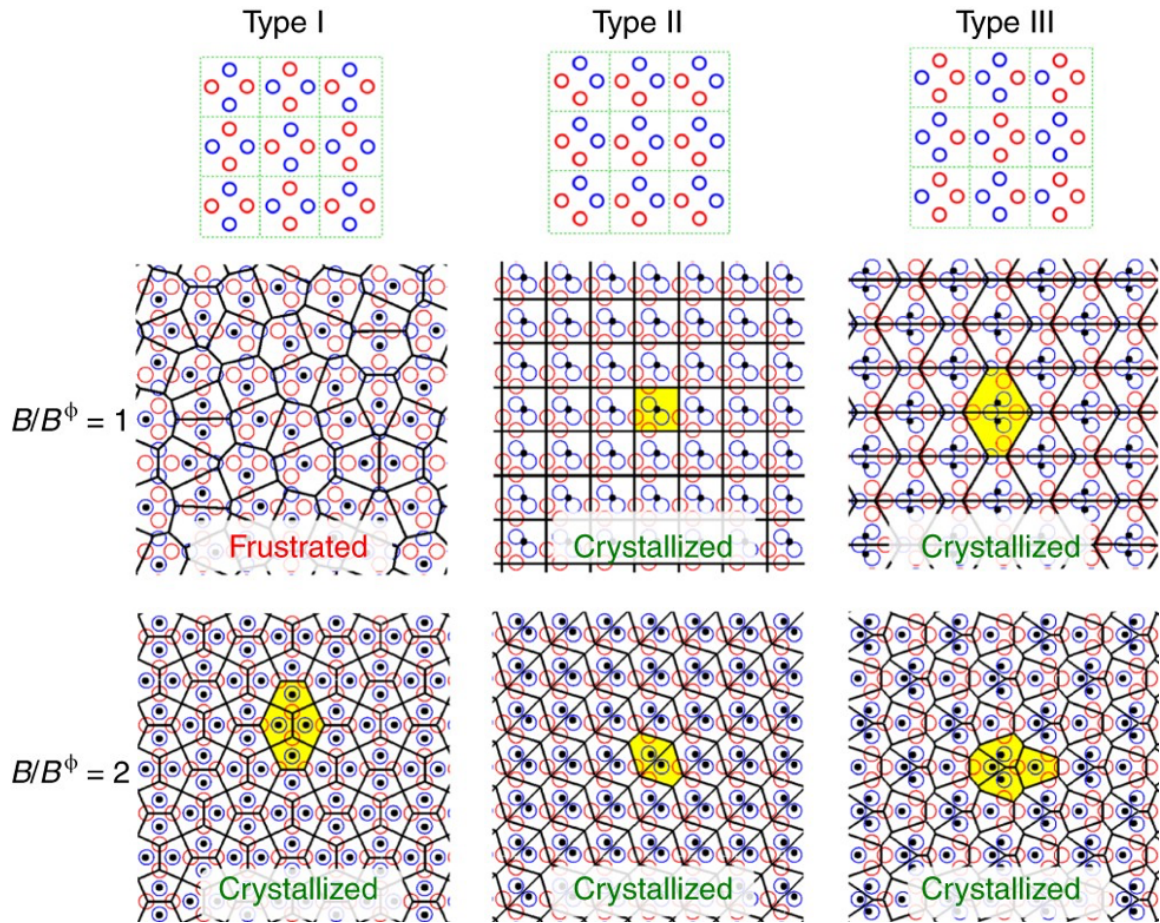


Figure B.1. Simulated distributions of flux quanta under type I, II and III magnetic-charge orders and various flux-quantum densities. Solid black lines constitute Voronoi diagrams elucidating the flux-quantum ordering. One repeating unit structure in each of the crystallized flux-quantum lattices is highlighted in yellow.[7]

BIBLIOGRAPHY

1. Michael Tinkham. *Introduction to Superconductivity*.
2. Wai-Kwong Kwok, Ulrich Welp, Andreas Glatz, Alexei E Koshelev, Karen J Kihlstrom, and George W Crabtree. Vortices in high-performance high-temperature superconductors. *Reports on Progress in Physics*, 79(11):116501, sep 2016.
3. C. Castelnovo, R. Moessner, and S.L. Sondhi. Spin ice, fractionalization, and topological order. *Annual Review of Condensed Matter Physics*, 3(1):35–55, 2012.
4. M. L. Latimer, G. R. Berdiyorov, Z. L. Xiao, F. M. Peeters, and W. K. Kwok. Realization of artificial ice systems for magnetic vortices in a superconducting MoGe thin film with patterned nanostructures. *Phys. Rev. Lett.*, 111:067001, 2013.
5. X. Zhang, A. Duzgun, Y. Lao, N. S. Bingham, J. Sklenar, H. Saglam, S. Subzwari, J. T. Batley, J. D. Watts, D. Bromley, C. Leighton, L. O’Brien, C. Nisoli, and P. Schiffer. Excitation strings and topological surgery in artificial spin ice. *arXiv e-prints*, page arXiv:2008.07571.
6. M. V. Milošević, S. V. Yampolskii, and F. M. Peeters. Magnetic pinning of vortices in a superconducting film: The (anti)vortex-magnetic dipole interaction energy in the london approximation. *Phys. Rev. B*, 66:174519, Nov 2002.
7. Y.-L. Wang, X. Ma, J. Xu, Z.-L. Xiao, A. Snezhko, R. Divan, L. E. Ocola, J. E. Pearson, B. Jánko, and W.-K. Kwok. Switchable geometric frustration in an artificial-spin-ice-superconductor heterosystem. *Nature Nanotechnol.*, 13(7):560, 2018.
8. A. A. Abrikosov. Nobel lecture: Type-ii superconductors and the vortex lattice. *Rev. Mod. Phys.*, 76:975–979, Dec 2004.
9. S. Ooi, T. Mochiku, M. Tachiki, and K. Hirata. Oscillatory behavior of vortex-lattice melting transition line in mesoscopic $\text{Bi}_2\text{Sr}_2\text{CaCu}_2\text{O}_{8+y}$ superconductors. *Phys. Rev. Lett.*, 114:087001, Feb 2015.
10. I. V. Grigorieva, W. Escoffier, J. Richardson, L. Y. Vinnikov, S. Dubonos, and V. Oboznov. Direct observation of vortex shells and magic numbers in mesoscopic superconducting disks. *Phys. Rev. Lett.*, 96:077005, Feb 2006.

11. N. Kokubo, H. Miyahara, S. Okayasu, and T. Nojima. Vortex shells in mesoscopic triangles of amorphous superconducting thin films. *Physica C: Superconductivity and its Applications*, 530:42 – 45, 2016. 28th International Symposium on Superconductivity.
12. H. Kamerlingh Onnes. *Leiden Comm.*, 120b, 122b, 124c, 1911.
13. W. Meissner and R. Ochsenfeld. Ein neuer effekt bei eintritt der supraleitfähigkeit. *Naturwissenschaften*, 21(44):787–788, Nov 1933.
14. J. N. RJABININ and L. W. SHUBNIKOW. Magnetic properties and critical currents of supra-conducting alloys. *Nature*, 135(3415):581–582, Apr 1935.
15. V. L. Ginzburg and L. D. Landau. *On the Theory of Superconductivity*. Springer Berlin Heidelberg, Berlin, Heidelberg, 2009.
16. A.A. Abrikosov. The magnetic properties of superconducting alloys. *Journal of Physics and Chemistry of Solids*, 2(3):199 – 208, 1957.
17. J. Bardeen, L. N. Cooper, and J. R. Schrieffer. Theory of superconductivity. *Phys. Rev.*, 108:1175–1204, Dec 1957.
18. M. Baert, V. V. Metlushko, R. Jonckheere, V. V. Moshchalkov, and Y. Bruynseraede. Composite flux-line lattices stabilized in superconducting films by a regular array of artificial defects. *Phys. Rev. Lett.*, 74:3269–3272, 1995.
19. V. Metlushko, U. Welp, G. W. Crabtree, R. Osgood, S. D. Bader, L. E. DeLong, Z. Zhang, S. R. J. Brueck, B. Ilic, K. Chung, and P. J. Hesketh. Interstitial flux phases in a superconducting niobium film with a square lattice of artificial pinning centers. *Phys. Rev. B*, 60:R12585–R12588, 1999.
20. U. Welp, Z. L. Xiao, J. S. Jiang, V. K. Vlasko-Vlasov, S. D. Bader, G. W. Crabtree, J. Liang, H. Chik, and J. M. Xu. Superconducting transition and vortex pinning in nb films patterned with nanoscale hole arrays. *Phys. Rev. B*, 66:212507, Dec 2002.
21. G. Karapetrov, J. Fedor, M. Iavarone, D. Rosenmann, and W. K. Kwok. Direct observation of geometrical phase transitions in mesoscopic superconductors by scanning tunneling microscopy. *Phys. Rev. Lett.*, 95:167002, 2005.
22. K. Harada, O. Kamimura, H. Kasai, T. Matsuda, A. Tonomura, and V. V. Moshchalkov. Direct observation of vortex dynamics in superconducting films with regular arrays of defects. *Science*, 274(5290):1167–1170, 1996.
23. G. R. Berdiyorov, M. V. Milošević, and F. M. Peeters. Novel commensurability effects in superconducting films with antidot arrays. *Phys. Rev. Lett.*, 96:207001, 2006.

24. D. Ray, C. J. Olson Reichhardt, B. Jankó, and C. Reichhardt. Strongly enhanced pinning of magnetic vortices in type-II superconductors by conformal crystal arrays. *Phys. Rev. Lett.*, 110:267001, 2013.
25. Y. L. Wang, M. L. Latimer, Z. L. Xiao, R. Divan, L. E. Ocola, G. W. Crabtree, and W. K. Kwok. Enhancing the critical current of a superconducting film in a wide range of magnetic fields with a conformal array of nanoscale holes. *Phys. Rev. B*, 87:220501, 2013.
26. Y. L. Wang, L. R. Thoutam, Z. L. Xiao, B. Shen, J. E. Pearson, R. Divan, L. E. Ocola, G. W. Crabtree, and W. K. Kwok. Enhancing superconducting critical current by randomness. *Phys. Rev. B*, 93:045111, Jan 2016.
27. H. J. Zhao, V. R. Misko, F. M. Peeters, V. Oboznov, S. V. Dubonos, and I. V. Grigorieva. Vortex states in mesoscopic superconducting squares: Formation of vortex shells. *Phys. Rev. B*, 78:104517, Sep 2008.
28. Igor S. Aranson and Lorenz Kramer. The world of the complex ginzburg-landau equation. *Rev. Mod. Phys.*, 74:99–143, Feb 2002.
29. C. J. Olson, C. Reichhardt, and Franco Nori. Nonequilibrium dynamic phase diagram for vortex lattices. *Phys. Rev. Lett.*, 81:3757–3760, Oct 1998.
30. A. E. Koshelev and V. M. Vinokur. Dynamic melting of the vortex lattice. *Phys. Rev. Lett.*, 73:3580–3583, Dec 1994.
31. E. H. Brandt. Computer simulation of vortex pinning in type ii superconductors. ii. random point pins. *Journal of Low Temperature Physics*, 53(1):71–152, Oct 1983.
32. C. J. Olson, C. Reichhardt, B. Jankó, and Franco Nori. Collective interaction-driven ratchet for transporting flux quanta. *Phys. Rev. Lett.*, 87:177002, Oct 2001.
33. C. Reichhardt, C. J. Olson, and F. Nori. Commensurate and incommensurate vortex states in superconductors with periodic pinning arrays. *Phys. Rev. B*, 57:7937–7943, 1998.
34. T. Giamarchi and P. Le Doussal. Phase diagrams of flux lattices with disorder. *Phys. Rev. B*, 55:6577–6583, Mar 1997.
35. I. Guillamón, R. Córdoba, J. Sesé, J. M. De Teresa, M. R. Ibarra, S. Vieira, and H. Suderow. Enhancement of long-range correlations in a 2d vortex lattice by an incommensurate 1d disorder potential. *Nature Physics*, 10(11):851–856, Nov 2014.
36. K. Mangold, P. Leiderer, and C. Bechinger. Phase transitions of colloidal monolayers in periodic pinning arrays. *Phys. Rev. Lett.*, 90:158302, 2003.

37. T. Bohlein, J. Mikhael, and C. Bechinger. Observation of kinks and antikinks in colloidal monolayers driven across ordered surfaces. *Nature Mater.*, 11(2):126–130, 2012.
38. A. Vanossi, N. Manini, and E. Tosatti. Static and dynamic friction in sliding colloidal monolayers. *Proc. Natl. Acad. Sci. (USA)*, 109(41):16429–16433, 2012.
39. D. McDermott, J. Amelang, C. J. Olson Reichhardt, and C. Reichhardt. Dynamic regimes for driven colloidal particles on a periodic substrate at commensurate and incommensurate fillings. *Phys. Rev. E*, 88:062301, 2013.
40. C. Reichhardt, D. Ray, and C. J. O. Reichhardt. Nonequilibrium phases and segregation for skyrmions on periodic pinning arrays. *Phys. Rev. B*, 98:134418, 2018.
41. K. Kobayashi. Moiré pattern in scanning tunneling microscopy: Mechanism in observation of subsurface nanostructures. *Phys. Rev. B*, 53:11091–11099, 1996.
42. H. Miao, A. Panna, A. A. Gomella, E. E. Bennett, S. Znati, L. Chen, and H. Wen. A universal moiré effect and application in X-ray phase-contrast imaging. *Nature Phys.*, 12(9):830–834, 2016.
43. Y. Cao, V. Fatemi, S. Fang, K. Watanabe, T. Taniguchi, E. Kaxiras, and P. Jarillo-Herrero. Unconventional superconductivity in magic-angle graphene superlattices. *Nature (London)*, 556(7699):43, 2018.
44. Yuan Cao, Valla Fatemi, Ahmet Demir, Shiang Fang, Spencer L. Tomarken, Jason Y. Luo, Javier D. Sanchez-Yamagishi, Kenji Watanabe, Takashi Taniguchi, Efthimios Kaxiras, Ray C. Ashoori, and Pablo Jarillo-Herrero. Correlated insulator behaviour at half-filling in magic-angle graphene superlattices. *Nature*, 556(7699):80–84, Apr 2018.
45. S. Shallcross, S. Sharma, E. Kandelaki, and O. A. Pankratov. Electronic structure of turbostratic graphene. *Phys. Rev. B*, 81:165105, 2010.
46. J. I. Martín, M. Vélez, J. Nogués, and I. K. Schuller. Flux pinning in a superconductor by an array of submicrometer magnetic dots. *Phys. Rev. Lett.*, 79:1929–1932, 1997.
47. A. N. Grigorenko, S. J. Bending, M. J. Van Bael, M. Lange, V. V. Moshchalkov, H. Fangohr, and P. A. J. de Groot. Symmetry locking and commensurate vortex domain formation in periodic pinning arrays. *Phys. Rev. Lett.*, 90:237001, 2003.
48. A. Crassous, R. Bernard, S. Fusil, K. Bouzehouane, D. Le Bourdais, S. Enouz-Vedrenne, J. Briatico, M. Bibes, A. Barthélémy, and J. E. Villegas. Nanoscale electrostatic manipulation of magnetic flux quanta in ferroelectric/superconductor $\text{BiFeO}_3/\text{YBa}_2\text{Cu}_3\text{O}_{7-\delta}$ heterostructures. *Phys. Rev. Lett.*, 107:247002, 2011.

49. J. I. Martín, M. Vélez, A. Hoffmann, I. K. Schuller, and J. L. Vicent. Artificially induced reconfiguration of the vortex lattice by arrays of magnetic dots. *Phys. Rev. Lett.*, 83:1022–1025, 1999.
50. C. J. Olson Reichhardt, A. Libál, and C. Reichhardt. Vortex configurations and dynamics in elliptical pinning sites for high matching fields. *Phys. Rev. B*, 73:184519, 2006.
51. A. Libál, C. J. Olson Reichhardt, and C. Reichhardt. Creating artificial ice states using vortices in nanostructured superconductors. *Phys. Rev. Lett.*, 102:237004, 2009.
52. J.-Y. Ge, V. N. Gladilin, J. Tempere, V. S. Zharinov, J. Van de Vondel, J. T. Devreese, and V. V. Moshchalkov. Direct visualization of vortex ice in a nanostructured superconductor. *Phys. Rev. B*, 96:134515, 2017.
53. I. A. Sadovskyy, A. E. Koshelev, W.-K. Kwok, U. Welp, and A. Glatz. Targeted evolution of pinning landscapes for large superconducting critical currents. *Proc. Natl. Acad. Sci.*, 116(21):10291–10296, 2019.
54. V. Misko, S. Savel’ev, and F. Nori. Critical currents in quasiperiodic pinning arrays: Chains and Penrose lattices. *Phys. Rev. Lett.*, 95:177007, 2005.
55. M. Kemmler, C. Gürlich, A. Sterck, H. Pöhler, M. Neuhaus, M. Siegel, R. Kleiner, and D. Koelle. Commensurability effects in superconducting Nb films with quasiperiodic pinning arrays. *Phys. Rev. Lett.*, 97:147003, 2006.
56. W. Yao, E. Wang, C. Bao, Y. Zhang, K. Zhang, K. Bao, C. K. Chan, C. Chen, J. Avila, M. C. Asensio, J. Zhu, and S. Zhou. Quasicrystalline 30° twisted bilayer graphene as an incommensurate superlattice with strong interlayer coupling. *Proc. Natl. Acad. Sci.*, 115(27):6928–6933, 2018.
57. J. M. B. Lopes dos Santos, N. M. R. Peres, and A. H. Castro Neto. Continuum model of the twisted graphene bilayer. *Phys. Rev. B*, 86:155449, 2012.
58. Dov Levine and Paul Joseph Steinhardt. Quasicrystals: A new class of ordered structures. *Phys. Rev. Lett.*, 53:2477–2480, Dec 1984.
59. N. David Mermin Neil Ashcroft. *Solid State Physics*.
60. C. Reichhardt and C. J. Olson Reichhardt. Commensurability effects at non-matching fields for vortices in diluted periodic pinning arrays. *Phys. Rev. B*, 76:094512, 2007.
61. S. Tung, V. Schweikhard, and E. A. Cornell. Observation of vortex pinning in Bose-Einstein condensates. *Phys. Rev. Lett.*, 97:240402, 2006.
62. A. Vanossi, N. Manini, M. Urbakh, S. Zapperi, and E. Tosatti. Colloquium: Modeling friction: From nanoscale to mesoscale. *Rev. Mod. Phys.*, 85:529–552, 2013.

63. L. Pauling. The structure and entropy of ice and of other crystals with some randomness of atomic arrangement. *J. Am. Chem. Soc.*, 57:2680–2684, 1935.
64. C. Nisoli, R. Moessner, and P. Schiffer. Colloquium: Artificial spin ice: Designing and imaging magnetic frustration. *Rev. Mod. Phys.*, 85:1473–1490, 2013.
65. S. H. Skjærvø, C. H. Marrows, R. L. Stamps, and L. J. Heyderman. Advances in artificial spin ice. *Nature Rev. Phys.*, 2:13–28, 2020.
66. Yuyang Lao, Francesco Caravelli, Mohammed Sheikh, Joseph Sklenar, Daniel Gardeazabal, Justin D. Watts, Alan M. Albrecht, Andreas Scholl, Karin Dahmen, Cristiano Nisoli, and Peter Schiffer. Classical topological order in the kinetics of artificial spin ice. *Nature Physics*, 14(7):723–727, Jul 2018.
67. R. F. Wang, C. Nisoli, R. S. Freitas, J. Li, W. McConville, B. J. Cooley, M. S. Lund, N. Samarth, C. Leighton, V. H. Crespi, and P. Schiffer. Artificial ‘spin ice’ in a geometrically frustrated lattice of nanoscale ferromagnetic islands. *Nature (London)*, 439(7074):303–306, 2006.
68. M. J. Morrison, T. R. Nelson, and C. Nisoli. Unhappy vertices in artificial spin ice: new degeneracies from vertex frustration. *New J. Phys.*, 15:045009, 2013.
69. J. P. Morgan, A. Stein, S. Langridge, and C. H. Marrows. Thermal ground-state ordering and elementary excitations in artificial magnetic square ice. *Nature Phys.*, 7(1):75–79, 2011.
70. V. Kapaklis, U. B. Arnalds, A. Farhan, R. V. Chopdekar, A. Balan, A. Scholl, L. J. Heyderman, and B. Hjörvarsson. Thermal fluctuations in artificial spin ice. *Nature Nanotechnol.*, 9(7):514–519, 2014.
71. I. Gilbert, Y. Lao, I. Carrasquillo, L. O’Brien, J. D. Watts, M. Manno, C. Leighton, A. Scholl, C. Nisoli, and P. Schiffer. Emergent reduced dimensionality by vertex frustration in artificial spin ice. *Nature Phys.*, 12(2):162, 2016.
72. R. P. Cowburn and M. E. Welland. Room temperature magnetic quantum cellular automata. *Science*, 287(5457):1466–1468, 2000.
73. C. A. Ross, S. Haratani, F. J. Castaño, Y. Hao, M. Hwang, M. Shima, J. Y. Cheng, B. Vögeli, M. Farhoud, M. Walsh, and Henry I. Smith. Magnetic behavior of lithographically patterned particle arrays (invited). *Journal of Applied Physics*, 91(10):6848–6853, 2002.
74. J.I Martin, J Nogués, Kai Liu, J.L Vicent, and Ivan K Schuller. Ordered magnetic nanostructures: fabrication and properties. *Journal of Magnetism and Magnetic Materials*, 256(1):449 – 501, 2003.

75. A. Ortiz-Ambriz, C. Nisoli, C. Reichhardt, C. J. O. Reichhardt, and P. Tierno. Colloquium: Ice rule and emergent frustration in particle ice and beyond. *Rev. Mod. Phys.*, 91:041003, 2019.
76. A. Libál, C. Reichhardt, and C. J. Olson Reichhardt. Realizing colloidal artificial ice on arrays of optical traps. *Phys. Rev. Lett.*, 97:228302, 2006.
77. A. Ortiz-Ambriz and P. Tierno. Engineering of frustration in colloidal artificial ices realized on microfeatured grooved lattices. *Nature Commun.*, 7:10575, 2016.
78. D. Y. Lee and P. Tierno. Energetics and the ground state quest in an artificial triangular colloidal ice. *Phys. Rev. Mater.*, 2(11):112601, 2018.
79. A. Libál, D. Y. Lee, A. Ortiz-Ambriz, C. Reichhardt, C. J. O. Reichhardt, P. Tierno, and C. Nisoli. Ice rule fragility via topological charge transfer in artificial colloidal ice. *Nature Commun.*, 9:4146, 2018.
80. F. Ma, C. Reichhardt, W. Gan, C. J. O. Reichhardt, and W. S. Lew. Emergent geometric frustration of artificial magnetic skyrmion crystals. *Phys. Rev. B*, 94:144405, 2016.
81. J. Trastoy, M. Malnou, C. Ulysse, R. Bernard, N. Bergeal, G. Faini, J. Lesueur, J. Briatico, and J. E. Villegas. Freezing and thawing of artificial ice by thermal switching of geometric frustration in magnetic flux lattices. *Nature Nanotech-nol.*, 9(9):710–715, 2014.
82. X.-H. Chen, X.-D. He, A.-L. Zhang, V. V. Moshchalkov, and J.-Y. Ge. Vortex ice pattern evolution in a kagome nanostructured superconductor. *Phys. Rev. B*, 102:054516, 2020.
83. Y.-Y. Lyu, X. Ma, J. Xu, Y.-L. Wang, Z.-L. Xiao, S. Dong, B. Jankó, H. Wang, R. Divan, J. E. Pearson, P. Wu, and W.-K. Kwok. Reconfigurable pinwheel artificial-spin-ice and superconductor hybrid device. *Nano Lett.*, 20:8933 – 8939, 2020.
84. C. Reichhardt, J. Groth, C. J. Olson, S. B. Field, and F. Nori. Spatiotemporal dynamics and plastic flow of vortices in superconductors with periodic arrays of pinning sites. *Phys. Rev. B*, 54:16108–16115, 1996.
85. S. T. Bramwell and M. J. P. Gingras. Spin ice state in frustrated magnetic pyrochlore materials. *Science*, 294(5546):1495–1501, 2001.
86. P. W. Anderson. Ordering and antiferromagnetism in ferrites. *Phys. Rev.*, 102:1008–1013, 1956.
87. Y.-L. Wang, Z.-L. Xiao, A. Snezhko, J. Xu, L. E. Ocola, R. Divan, J. E. Pearson, G. W. Crabtree, and W.-K. Kwok. Rewritable artificial magnetic charge ice. *Science*, 352(6288, SI):962–966, 2016.

88. M. A. SUBRAMANIAN, C. C. TORARDI, J. C. CALABRESE, J. GOPALAKRISHNAN, K. J. MORRISSEY, T. R. ASKEW, R. B. FLIPPEN, U. CHOWDHRY, and A. W. SLEIGHT. A new high-temperature superconductor: Bi₂sr_{3-x}ca_xcu₂o_{8+y}. *Science*, 239(4843):1015–1017, 1988.
89. V. Vinokur, B. Khaykovich, E. Zeldov, M. Konczykowski, R.A. Doyle, and P.H. Kes. Lindemann criterion and vortex-matter phase transitions in high-temperature superconductors. *Physica C: Superconductivity*, 295(3):209 – 217, 1998.
90. E. Zeldov, D. Majer, M. Konczykowski, V. B. Geshkenbein, V. M. Vinokur, and H. Shtrikman. Thermodynamic observation of first-order vortex-lattice melting transition in bi₂sr₂cacu₂o₈. *Nature*, 375(6530):373–376, Jun 1995.
91. V. M. Vinokur, M. V. Feigel'man, V. B. Geshkenbein, and A. I. Larkin. Resistivity of high- t_c superconductors in a vortex-liquid state. *Phys. Rev. Lett.*, 65:259–262, Jul 1990.
92. Jan Kierfeld and Valerii Vinokur. Lindemann criterion and vortex lattice phase transitions in type-ii superconductors. *Phys. Rev. B*, 69:024501, Jan 2004.
93. C.-S. Lee, B. Jankó, I. Derényi, and A.-L. Barabási. Reducing vortex density in superconductors using the ‘ratchet effect’. *Nature*, 400(6742):337–340, Jul 1999.
94. J. E. Villegas, E. M. Gonzalez, M. P. Gonzalez, J. V. Anguita, and J. L. Vicent. Experimental ratchet effect in superconducting films with periodic arrays of asymmetric potentials. *Phys. Rev. B*, 71:024519, Jan 2005.
95. G. Carapella and G. Costabile. Ratchet effect: Demonstration of a relativistic fluxon diode. *Phys. Rev. Lett.*, 87:077002, Jul 2001.
96. Clécio C. de Souza Silva, Joris Van de Vondel, Mathieu Morelle, and Victor V. Moshchalkov. Controlled multiple reversals of a ratchet effect. *Nature*, 440(7084):651–654, Mar 2006.
97. Qiming Lu, C. J. Olson Reichhardt, and C. Reichhardt. Reversible vortex ratchet effects and ordering in superconductors with simple asymmetric potential arrays. *Phys. Rev. B*, 75:054502, Feb 2007.
98. C. Reichhardt, D. Ray, and C. J. Olson Reichhardt. Reversible ratchet effects for vortices in conformal pinning arrays. *Phys. Rev. B*, 91:184502, May 2015.
99. G. Blatter, M. V. Feigel'man, V. B. Geshkenbein, A. I. Larkin, and V. M. Vinokur. Vortices in high-temperature superconductors. *Rev. Mod. Phys.*, 66:1125–1388, Oct 1994.
100. B. J. Baelus, L. R. E. Cabral, and F. M. Peeters. Vortex shells in mesoscopic superconducting disks. *Phys. Rev. B*, 69:064506, Feb 2004.

101. J. J. Palacios. Vortex matter in superconducting mesoscopic disks: Structure, magnetization, and phase transitions. *Phys. Rev. B*, 58:R5948–R5951, Sep 1998.
102. T. Cren, L. Serrier-Garcia, F. Debontridder, and D. Roditchev. Vortex fusion and giant vortex states in confined superconducting condensates. *Phys. Rev. Lett.*, 107:097202, Aug 2011.
103. A. K. Geim, I. V. Grigorieva, S. V. Dubonos, J. G. S. Lok, J. C. Maan, A. E. Filippov, and F. M. Peeters. Phase transitions in individual sub-micrometre superconductors. *Nature*, 390(6657):259–262, Nov 1997.
104. V. A. Schweigert and F. M. Peeters. Flux penetration and expulsion in thin superconducting disks. *Phys. Rev. Lett.*, 83:2409–2412, Sep 1999.
105. B. J. Baelus, F. M. Peeters, and V. A. Schweigert. Saddle-point states and energy barriers for vortex entrance and exit in superconducting disks and rings. *Phys. Rev. B*, 63:144517, Mar 2001.
106. P. Singha Deo, V. A. Schweigert, F. M. Peeters, and A. K. Geim. Magnetization of mesoscopic superconducting disks. *Phys. Rev. Lett.*, 79:4653–4656, Dec 1997.
107. Jonathan P. K. Doye. Network topology of a potential energy landscape: A static scale-free network. *Phys. Rev. Lett.*, 88:238701, May 2002.
108. Frank H. Stillinger and Thomas A. Weber. Packing structures and transitions in liquids and solids. *Science*, 225(4666):983–989, 1984.
109. Andreas Heuer. Exploring the potential energy landscape of glass-forming systems: from inherent structures via metabasins to macroscopic transport. *Journal of Physics: Condensed Matter*, 20(37):373101, aug 2008.
110. Pablo G. Debenedetti and Frank H. Stillinger. Supercooled liquids and the glass transition. *Nature*, 410(6825):259–267, Mar 2001.
111. Jonathan P. K. Doye and Claire P. Massen. Characterizing the network topology of the energy landscapes of atomic clusters. *The Journal of Chemical Physics*, 122(8):084105, 2005.
112. David Wales. Energy landscapes: Calculating pathways and rates. *Int. Rev. Phys. Chem.*, 25:237–282, 01 2006.
113. David J. Wales. Rearrangements of 55-atom lennard-jones and (c60)55 clusters. *The Journal of Chemical Physics*, 101(5):3750–3762, 1994.
114. David J. Wales, Jonathan P. K. Doye, Mark A. Miller, Paul N. Mortenson, and Tiffany R. Walsh. *Energy Landscapes: From Clusters to Biomolecules*, pages 1–111. John Wiley Sons, Ltd, 2000.

115. Gary D. Bader and Christopher WV Hogue. An automated method for finding molecular complexes in large protein interaction networks. *BMC Bioinformatics*, 4(1):2, Jan 2003.
116. Danail Bonchev and Dennis Rouvray. *Complexity in chemistry. Introduction and fundamentals*. 01 2003.
117. Danail Bonchev and Dennis Rouvray. Complexity in chemistry, biology, and ecology. *Mathematical and Computational Chemistry*, 01 2005.
118. D. Bonchev. Information-theoretic indices for characterization of chemical structures. 1983.
119. N. Trinajstić D. Bonchev. Information theory, distance matrix, and molecular branching. *J. Chem. Phys.*, 67:4517–4533, 1977.

*This document was prepared & typeset with pdfL^AT_EX, and formatted with
NDDiss2_ε classfile (v3.2017.2[2017/05/09])*